

**PRECISION CALCULATIONS IN UNIVERSAL  
EXTRA DIMENSIONS**

by

**Daniel Wiegand**

Bachelor of Science, Ruprecht-Karls University, Heidelberg (2011)

Master of Science, Ruprecht-Karls University, Heidelberg (2013)

Submitted to the Graduate Faculty of  
the Kenneth P. Dietrich School of Arts and Sciences in partial  
fulfillment

of the requirements for the degree of

**Doctor of Philosophy**

University of Pittsburgh

2018

UNIVERSITY OF PITTSBURGH  
DIETRICH SCHOOL OF ARTS AND SCIENCES

This dissertation was presented

by

Daniel Wiegand

It was defended on

May 10th 2018

and approved by

Ayres Freitas, University of Pittsburgh

Adam Leibovich, University of Pittsburgh

Joseph Boudreau, University of Pittsburgh

Arthur Kosowsky, University of Pittsburgh

Ira Rothstein, Carnegie Mellon University

Dissertation Director: Ayres Freitas, University of Pittsburgh

# PRECISION CALCULATIONS IN UNIVERSAL EXTRA DIMENSIONS

Daniel Wiegand, PhD

University of Pittsburgh, 2018

The Standard Model of particle physics, despite its amazing success, is in need of an extension to describe nature at high scales. One class of proposals for such an extension are field theories with extra dimensions. Many of these models have attractive features like stable dark matter candidates, promising at least partial answers to nature's questions.

Our focus lies with investigating the impact radiative corrections have on the phenomenology of the Universal Extra Dimensions (UED) model and the subsequent discovery potential at e.g. Hadron colliders. We study in detail the Next-to-Leading-Order corrections to the pair production of heavy vector color-octets, as they typically appear in such models. Additionally, we discuss how a variation of the cutoff scale influences this result. This is of particular importance since this a priori unknown scale represents a large source of uncertainty.

Subsequently we investigate radiatively induced operators for the entire Standard Model formulated in UED, particularly the impact they have on the degenerate mass spectrum and KK-number violating decays. This allows us to derive bounds from both indirect searches and directly detectable new physics signals.

## TABLE OF CONTENTS

<b>PREFACE</b> . . . . .	xiii
<b>1.0 INTRODUCTION</b> . . . . .	1
<b>2.0 THEORETICAL CONCEPTS</b> . . . . .	8
2.1 Universal Extra Dimensions . . . . .	8
2.1.1 $\Phi^4$ in 5D - A Toy Example . . . . .	9
2.1.2 The Standard Model in 5D . . . . .	14
2.2 The Two-Site Coloron Model . . . . .	17
<b>3.0 COLORON PAIR PRODUCTION AT NLO</b> . . . . .	22
3.1 Obtaining the Cross Section through Phase Space Slicing . . . . .	22
3.1.1 Renormalization . . . . .	23
3.1.2 Infrared Divergencies and Phase Space Slicing . . . . .	26
3.1.2.1 The Soft Limit . . . . .	27
3.1.2.2 The Collinear Limit . . . . .	28
3.1.3 Notes on the Technical Implementation . . . . .	30
3.2 Numerical Results . . . . .	31
3.3 Summary and Conclusions . . . . .	33
<b>4.0 THRESHOLD BEHAVIOR OF VERTEX FUNCTIONS</b> . . . . .	42
4.1 Infrared Divergent Contributions . . . . .	43
4.2 Contributions from Higher Modes . . . . .	45
4.2.1 Standard Model Vertices . . . . .	45
4.2.2 KK-Vertices . . . . .	48
4.2.3 Asymptotic Expansion . . . . .	50

4.2.4	Exact Renormalization Group Running . . . . .	52
4.2.4.1	QED-like Contributions . . . . .	56
4.2.4.2	QCD-like Contributions . . . . .	59
4.3	Phenomenological Analysis . . . . .	62
4.4	Summary and Conclusions . . . . .	64
<b>5.0</b>	<b>RADIATIVE CORRECTIONS TO MASSES AND VERTICES</b>	
	<b>IN MUED . . . . .</b>	<b>66</b>
5.1	Mass Corrections . . . . .	66
5.1.1	Approach . . . . .	67
5.1.2	Results . . . . .	70
5.2	KK-Number Violating Interactions . . . . .	73
5.2.1	Approach . . . . .	73
5.2.2	Results . . . . .	74
5.2.2.1	$\bar{\psi}_0\text{-}\psi_0\text{-}V_2^\mu$ coupling: . . . . .	74
5.2.2.2	$\bar{\psi}_2\text{-}\psi_0\text{-}V_0^\mu$ coupling: . . . . .	75
5.2.2.3	$V_2^{\mu,a}(p)\text{-}V_0^{\nu,b}(k_1)\text{-}V_0^{\rho,c}(k_2)$ coupling: . . . . .	76
5.2.2.4	$\bar{T}_2\text{-}t_0\text{-}\Phi_0 / \bar{t}_2\text{-}t_0/b_0\text{-}\Phi_0$ coupling: . . . . .	76
5.2.2.5	$\Phi_2$ decay couplings: . . . . .	77
5.3	Phenomenological Implications . . . . .	79
5.3.1	Mass Hierarchy . . . . .	79
5.3.2	Branching Ratios of Level-2 KK Excitations . . . . .	80
5.3.2.1	$\psi_2$ Decays . . . . .	81
5.3.2.2	$V_2$ Decays . . . . .	82
5.3.2.3	Cross Sections and Signatures . . . . .	83
5.4	Summary and Conclusions . . . . .	84
<b>6.0</b>	<b>CONCLUSIONS AND OUTLOOK . . . . .</b>	<b>98</b>
	<b>APPENDIX A. LAGRANGIANS AND FEYNMAN RULES . . . . .</b>	<b>101</b>
A.1	mUED Lagrangian . . . . .	101
A.1.1	The Gauge Sector . . . . .	102
A.1.2	The Fermion Sector . . . . .	104

A.1.3	The Higgs Sector	104
A.1.4	The Yukawa Sector	106
A.2	Feynman Rules for the Two-Site Coloron Model	107
A.2.1	Feynman Rules Involving Massless Quarks	107
A.2.2	Vertices Involving the Top Quark	108
A.2.3	Three-Point Boson Vertices	108
A.2.4	Feynman Rules Involving Ghosts	109
A.2.5	Four-Point Boson Vertices	109
<b>APPENDIX B. SPECIAL INTEGRALS AND FUNCTIONS</b>		<b>111</b>
B.1	One Loop Functions and Identities	111
B.1.1	Integrals with Ultraviolet Divergences	112
B.1.2	Integrals with Soft Divergencies	112
B.1.2.1	Triangle Functions	113
B.1.2.2	Box Functions	114
B.1.3	Derivatives of One-Loop Functions	115
B.1.4	Useful Identities and Special Cases	116
B.2	Soft Angular Integrals	117
<b>APPENDIX C. KK-NUMBER VIOLATING COUPLINGS IN MUED</b>		<b>119</b>
<b>BIBLIOGRAPHY</b>		<b>124</b>

## LIST OF TABLES

1	<i>Field content of the minimal universal extra dimension (MUED) model and their gauge and <math>\mathbb{Z}_2</math> quantum numbers.</i>	15
2	<i>Quantum numbers and chirality of the quark fields in the two-site symmetric Coloron model.</i>	19

## LIST OF FIGURES

1	<i>UED orbifolding. (A) periodic boundary conditions leading to <math>M_5 = M_4 \times S_1</math>. (B) Mapping out a <math>\mathbb{Z}_2</math> symmetry by identifying two opposite sides of the circle. Leading to (C) two fixed points on the boundaries of the essentially flat bulk.</i>	9
2	<i><math>\phi^4</math> tree-level vertices as they appear in the compactified theory. (A) pure SM vertex, (B) two SM modes and two KK modes, (C) one SM mode and three KK modes and (D) pure KK vertex. All Feynman diagrams in this thesis are produced using JAXODRAW 2.0 [20].</i>	12
3	<i>Loop induced process that produces a four-point operator that violates KK-number but conserves parity (A) loop process set up of KK-number conserving tree-level vertices (B) the effective vertex breaks KK-number conservation by <math>2n</math> units. Note that there also exist similar <math>S</math> and <math>U</math> channel contributions to the effective vertex, which we omit here.</i>	13
4	<i>Born-level diagrams contributing to massive color-octet vector-boson pair production. Here the spring–solid lines indicate massive color-octet vector-bosons, while the double lines indicate massive <math>\mathcal{P}</math>-odd quarks, and the dashed line indicates a <math>\mathcal{P}</math>-odd Goldstone scalar.</i>	35
5	<i>Sample one-loop diagrams contributing to Coloron pair production. See Fig. 4 for the definition of the different propagator line types.</i>	36
6	<i>Sample real radiation diagrams contributing to Coloron pair production. See Fig. 4 for the definition of the different propagator line types.</i>	36

7	<i>Real Emission of a soft/collinear gluon from a final state quark. The momentum square <math>(p-k_g)^2 = -2E_p E_g(1-\cos\theta)</math> in the denominator of the propagator goes to zero for either <math>E_g \rightarrow 0</math> or <math>\cos\theta \rightarrow 1</math>.</i>	37
8	<i>Flowchart illustrating the additions made to the FEYN CALC/FEYN ARTS framework. Yellow routines represent publicly available packages, while green are direct amends to that code. White parallelograms represent external input and the red integrator is a set of separate FORTRAN routines.</i>	37
9	<i>Dependence of the NLO cross-section for the <math>pp \rightarrow CC</math> on the soft cut-off <math>\delta_s</math> (left) and the collinear cut-off <math>\delta_c</math> (right). Both plots are for a <math>pp</math> center-of-mass energy of <math>\sqrt{s} = 14</math> TeV, Coloron mass <math>M = 1</math> TeV, and renormalization and factorization scales <math>\mu = \mu_F = M</math>. Furthermore, in the left (right) panel, the fixed value <math>\delta_c = 10^{-5}</math> (<math>\delta_s = 10^{-3.5}</math>) has been used.</i>	38
10	<i>Total LO and NLO Coloron pair production cross-sections as function of the Coloron mass <math>M</math>, for <math>\sqrt{s} = 14</math> TeV and <math>\mu = \mu_F = M</math>. The mass splitting between the Colorons and <math>\mathcal{P}</math>-odd quarks in the Born contribution has been set to the value predicted by mUED, see text and eq. (3.26), while the splitting has been neglected in the NLO corrections. The lower panel shows the ratio between NLO and LO cross-sections.</i>	39
11	<i>Dependence of the total LO and NLO Coloron pair production cross-sections on the combined renormalization and factorization scale <math>\mu = \mu_F</math>. The plot is based on the <math>pp</math> center-of-mass energy <math>\sqrt{s} = 14</math> TeV, mass <math>M = 1</math> TeV, and mass splitting <math>M - M_\Psi</math> in the Born contribution as predicted by mUED, see text and eq. (3.26).</i>	40
12	<i>Total LO and NLO Coloron pair production cross-sections as function of quark-Coloron mass splitting <math>\Delta M = M - M_\Psi</math>. The other input parameters have been set to <math>\sqrt{s} = 14</math> TeV, mass <math>M = 1</math> TeV, and <math>\mu = \mu_F = M</math>.</i>	41
13	<i>Differential cross-section for Coloron pair production in terms of rapidity at LO and NLO accuracy, for <math>\sqrt{s} = 14</math> TeV, mass <math>M = 1</math> TeV, and <math>\mu = \mu_F = M</math>.</i>	41

14	Sample diagrams the decay of the level-1 gluon decay $G_0 \rightarrow q_0 \bar{Q}_0$ within the Coloron model. (A) Born-level decay (B) NLO correction to the Born vertex (C) real emission contribution with an infrared divergence. . . . .	44
15	Full LO and NLO decay width for the level-1 KK-gluon decaying into a regular quark and the level-1 KK-quark within the Coloron model. Both curves exhibit the same $\Lambda$ dependence, since the $\kappa$ -factor is constant in our approximation. . . . .	46
16	Sample diagrams for the KK-contributions to the SM vertices. (A) quark-gluon vertex (B) three-point gluon vertex (C) four-point gluon vertex. . . . .	47
17	Sample diagrams for the KK-contributions to the vertex with two level-1 modes as external legs. . . . .	49
18	Running of the SM vertex function $q_0 - q_0 - g_0$ (solid line) and the KK vertex $q_0 - Q_1 - G_1$ (dashed line). We compare the full summation up to the cutoff with the asymptotic expansion as well as the results obtained from the FRGE running. The integration constants have been fixed such that the couplings coincide at $\Lambda R = 20$ . . . . .	63
19	Generic Feynman diagrams for the one-loop contributions to the self-energies of KK vector bosons. Here wavy, dashed, dotted and solid lines indicate the KK modes of vector bosons, scalars, ghosts and fermions, respectively. $V_5$ denotes the scalar degree of freedom from the fifth component of a 5D gauge field, whereas $H$ stands for the contribution from a genuine 5D scalar field. . . . .	88
20	Generic Feynman diagrams for the one-loop contributions to the self-energies of KK scalars. See caption of Fig. 19 for further explanations. . . . .	88
21	Generic Feynman diagrams for the one-loop contributions to the self-energy of KK fermions. See caption of Fig. 19 for further explanations. . . . .	89
22	Contributions to the $\bar{\psi}_0 - \psi_0 - V_2$ vertex, where the blobs indicate one-loop corrections. Zero-mode vector and fermion propagators are depicted through normal wavy and solid lines, respectively, whereas level-2 vector and fermion propagators are shown as wavy-solid and double-solid lines, respectively. . . . .	89
23	Vertex diagram contributing to KK-number violating vector-boson-fermion couplings involving a KK-Higgs in the loop. . . . .	89

24	Contributions to the $\bar{\psi}_2\text{-}\psi_0\text{-}V_0$ vertex. See caption of Fig. 23 for more explanations. . . . .	90
25	Contributions to the $V_2\text{-}V_0\text{-}V_0$ vertex. See caption of Fig. 23 for more explanations. . . . .	90
26	Mass spectrum of KK particles at level-1 for $R^{-1} = 1$ TeV and $\Lambda R = 20$ without (left) / with (right) finite contributions. . . . .	91
27	Left: The phase diagram in the $(R^{-1}, \Lambda R)$ plane from Ref. [96] is reproduced using the incorrect numerical factor (see text), which shows that the KK Higgs could be the NLKP in MUED for a large value of $R^{-1}$ . Right: Fixing $\Lambda R = 20$ , the old (incorrect) result is shown in (red, solid) as a function of $R^{-1}$ . The correct result is shown in (blue, dashed), while the curve in (green, dotted) includes finite terms. We find that KK leptons are always the NLKP. . . . .	91
28	Dependence of the Weinberg angle $\theta_n$ for KK levels ( $n = 1, \dots, 5$ ) on $R^{-1}$ for $\Lambda R = 20$ with (right) / without (left) finite contributions. . . . .	92
29	Branching fractions of $SU(2)_L$ -doublet level-2 KK lepton (left) and charged $SU(2)_L$ -singlet level-2 KK lepton (right). Solid curves include finite corrections and new decay channels, while dotted curves are old results. . . . .	92
30	Branching fraction of $SU(2)_L$ -doublet level-2 KK quark (left) and $SU(2)_L$ -singlet level-2 KK quark (right) for the up-type. . . . .	93
31	Branching fraction of $SU(2)_L$ -doublet KK top quark (left) and $SU(2)_L$ -singlet KK top quark (right). . . . .	93
32	Branching fractions of $\gamma_2, Z_2, W_2^\pm$ and $g_2$ for $\Lambda R = 20$ . . . . .	94
33	The decay width of level-2 gauge bosons as a function of $R^{-1}$ for $\Lambda R = 20$ . Solid curves include finite corrections, while dotted curves are old results. . . . .	95
34	Single production cross section of level-2 KK gauge bosons (left) and level-2 KK fermions (right) as a function of $R^{-1}$ . Dotted curves (left) are results from Ref. [97] and solid curves are new results including finite terms. Level-2 fermion cross sections and $\sigma(gg \rightarrow g_2)$ have been computed first time. The cut-off scale has been set to $\Lambda R = 20$ . . . . .	95

35	<i>Strong production of <math>n = 2</math> KK particles at the 14 TeV LHC. The left panel shows KK-quark pair production, while the right panel shows KK-quark/KK-gluon associated production and KK gluon pair production. Updated results (solid curves) are similar to old results (in dashed curves from Ref. [97]). The cut-off scale has been set to <math>\Lambda R = 20</math>.</i>	96
36	<i><math>5\sigma</math> discovery reach for <math>\gamma_2</math> (left) and <math>Z_2</math> (right). We show the total integrated luminosity <math>\mathcal{L}</math> (in <math>\text{fb}^{-1}</math>) required for a <math>5\sigma</math> excess of signal over SM backgrounds in the di-electron (red, dotted) and di-muon (blue, dashed) channels. In each plot, the upper set of curves labeled as ‘DY’ make use of the single production of <math>\gamma_2</math> or <math>Z_2</math> (from Fig. 34), while the lower set of curves labeled as ‘All processes’ includes indirect <math>\gamma_2</math> and <math>Z_2</math> productions from <math>n = 2</math> KK quarks (see Fig. 35). We assumed the same signal and background efficiencies used in Ref. [97] and combined with our updated cross sections and branching fractions.</i>	97

## PREFACE

First and foremost I want to thank Ayres Freitas for taking on the Sisyphean task of being my advisor. His unshakable patience and unique brand of humor made the journey down the physics rabbit hole a grand experience for me. I want to thank him not only for guiding me academically but also having my back through all major and minor crises encountered on the way. It is hard to adequately express my gratitude without becoming sentimental so I will leave it at that.

I would like to extend my thanks to Adam Leibovich, Joe Boudreau, Arthur Kosowsky and Ira Rothstein for agreeing to be on my committee and for going out of their ways to advise me through countless productive questions and helpful suggestions.

I thank KC Kong for the fruitful collaboration and helping me out with my postdoc application.

My thanks also belong to my colleagues and friends, without whom this thesis would have probably been done sooner, but significantly less enjoyable. I would like to thank (in no particular order) Kevin Sapp and Anna Elder, Louis Lello, Kevin Wilk, Fernando Zago, Xing Wang, Lin Dai, British Daniel and Karissa Miller and all other members of the bull pen (past and present) - especially Zhuoni Qian for her never-ending tech support and Barmak Shams Es Haghi for proofreading part of the manuscript. Thank you for the physics debates and subsequent shenanigans.

Additional thanks belongs to Leyla Hirschfeld and Cindy Cercone, without whom the bureaucracy would have gotten the better of me.

To my Mom and Dad and brother, for unflinchingly supporting and encouraging me from an ocean away.

And to Zac, who made it all worth while.

## 1.0 INTRODUCTION

The Standard Model (SM) of particle physics manages to describe the data we collected on the electroweak and strong interactions of matter with astonishing precision. Although highly successful it cannot be regarded as a complete description of nature for a number of reasons.

From a purely theoretical point of view it has to be noted that the Standard Model can only be an effective model for a UV-complete theory, which emerges above some a priori unknown cutoff scale. This picture is supported by evidence [1–3] that a theory containing a fundamental scalar, like the Higgs within the Standard Model, becomes trivial at very high scales. The UV-completion of the theory might additionally be able to unify the Standard Model forces and thus bring down the unsatisfactorily large number of unfixed parameters which so far could only be determined through measurement.

On the phenomenological side is the Standard Model unable to address the observed matter-antimatter asymmetry in the universe or the existence of massive neutrinos. Additionally, we do not currently understand how to incorporate gravity into the existing framework at a fundamental level. Perhaps the biggest phenomenological caveat relates to the Standard Model not containing a viable dark matter candidate. Over the years there has been an abundance of observational evidence for the existence of dark matter, like the discrepancy between measured and predicted orbital velocity of disk galaxies [4] or the observed gravitational lensing exhibited by galaxy clusters [5]. Based on say the  $\Lambda$ CDM cosmological model, dark matter represents about a quarter of the energy content of the universe, whereas the matter described by the Standard Model accounts for only about five percent:

$$\Omega_0 = \Omega_b + \Omega_c + \Omega_\Lambda = (1.00 \pm 0.009), \tag{1.1}$$

with the fractional density parameters measured [6] for baryonic matter  $\Omega_b = (0.049 \pm 0.001)$ , dark matter  $\Omega_c = (0.259 \pm 0.006)$ , and  $\Omega_\Lambda = (0.692 \pm 0.006)$ , describing the vacuum energy of space.

Even though the microscopic structure of dark matter has been a mystery for some time, a compelling explanation would be the existence of new elementary particles, that are only interacting through gravity and the weak nuclear force, or new dynamics comparable to the weak force. These so-called WIMPs (weakly interacting massive particles) would be required to be stable (or at least sufficiently long-lived) and have a mass  $\mathcal{O}(\text{TeV})$  to explain the dark matter relic abundance we observe in the universe today.

Countless models for physics beyond the Standard Model (BSM) have been constructed in an effort to resolve some or all of these problems. However, only experiment can shed light on what is and is not realized in nature. We have to rely on clues from direct discoveries and indirect constraints. It is very difficult to draw conclusions from indirect searches, since the decoupling theorem [7] states that the specifics of UV physics contributing to SM operators - once integrated out - cannot be reconstructed from the low-energy effective operators in details. Our goal therefore is to develop a set of tools and techniques that lead to robust and precise predictions to compare with experimental data. Going beyond the leading order in perturbation theory is an integral part in doing so: Radiative corrections can represent sizable contributions to observables, reduce unphysical scale dependencies and shape the phenomenology of a model considerably.

One attractive set of BSM theories is based on the idea that our four dimensional space-time is only a subspace of a more complicated higher-dimensional spacetime; postulating the existence of one or more Extra Dimensions in addition to the typical four. A number of models impose a parity on their particle content, which helps the predictions they make to evade the strong electroweak precision constraints. Additionally it forces new states to be pair produced, leading to rather weak bounds from the direct searches conducted so far. The same parity usually leads to the lightest new particle in the spectrum being stable and thus representing a possible dark matter candidate. An extensive review of dark matter within the Extra Dimensions context can be found in [8].

The idea to formulate field theory in a higher dimensional space dates back to the 1920s. The

first serious attempt was made by Theodor Kaluza [9], who equipped General Relativity with an additional space-like dimension in an effort to find a unified description of gravity and electromagnetism, the only fundamental forces known at the time. He additionally assumed that the components of the 5D metric tensor are constant across the fifth dimension and then parametrized that metric tensor as

$$G_{MN} = \left( \begin{array}{c|c} e^{\frac{1}{\sqrt{3}}\phi} g_{\mu\nu} + e^{-\frac{2}{\sqrt{3}}\phi} A_\mu A_\nu & e^{-\frac{2}{\sqrt{3}}\phi} A_\mu \\ \hline e^{-\frac{2}{\sqrt{3}}\phi} A_\mu^T & e^{-\frac{2}{\sqrt{3}}\phi} \end{array} \right) \quad (1.2)$$

with  $g_{\mu\nu}$ ,  $A_\mu$  and  $\phi$  all being functions of the four original spacetime coordinates. Our conventions are such that lowercase greek indices refer to the first four dimensions  $\mu \in \{0, 1, 2, 3\}$ , while uppercase latin ones denote all five dimensions  $M \in \{0, 1, 2, 3, 5\}$ . The fifth coordinate  $x_5$  we will occasionally call  $y$ .

Calculating the 5D Einstein-Hilbert action for this particular metric allowed him to show that the 5D curvature scalar  $R^{(5)}$  factorizes into a 4D one  $R^{(4)}$  built from  $g_{\mu\nu}$ , an abelian field strength tensor for the field  $A_\mu$  and a kinetic term for the scalar field  $\phi$  minimally coupled to the metric

$$S_5 \sim \int d^5x \sqrt{-G} R^{(5)} = V_5 \int d^4x \sqrt{-g} \left[ R^{(4)} - \frac{1}{4} e^{-\sqrt{3}\phi} F_{\mu\nu} F^{\mu\nu} - \frac{1}{2} \partial_\mu \phi \partial^\mu \phi \right], \quad (1.3)$$

where  $V_5$  is the volume of the fifth dimension, that can be absorbed into the definition of the 4D Newton's constant.

He thus showed that General Relativity in five dimensions describes gravity as well as free electromagnetism in four dimensions and an additional massless scalar, called the Dilaton. This is not entirely surprising since the general 5D coordinate invariance of  $R^{(5)}$  can be separated into 4D diffeomorphism invariance and a U(1) symmetry, forcing  $A_\mu$  to appear only as part of  $F_{\mu\nu} = \partial_\mu A_\nu - \partial_\nu A_\mu$ .

The aesthetically displeasing ad hoc assumption that none of the fields depend on the fifth coordinate was improved upon by Oskar Klein [10], who instead imposed a cylindricity condition on them, such that the two points  $y$  and  $y + 2\pi R$  were identified, giving the 5D

space-time the geometry of the cylinder  $\mathcal{M}_4 \times S_1$ , with  $\mathcal{M}_4$  being regular 4D Minkowski space. Making  $R$ , the so-called radius of compactification, sufficiently small then also resolves the phenomenological issue of the apparent absence of a fifth spatial dimension from everyday life - for conventional energy scales, the fifth dimension is not resolved and we observe an effectively 4D world. In modern terminology we refer to the 4D encasing subspace of the compactified volume as the Brane, and the higher dimensional enclosed space as the Bulk. Klein's postulate leads to a number of interesting features. The 5D energy-momentum relation

$$E^2 = p_{x_1}^2 + p_{x_2}^2 + p_{x_3}^2 + p_y^2 + m^2 \quad (1.4)$$

now also links the energy of our particles to their momenta along the fifth dimension  $p_y$ . At the same time we know, due to de Broglie, that the wavelengths of those particles need to be multiple integers of the circumference of the extra dimension

$$\lambda = \frac{2\pi R}{n}. \quad (1.5)$$

Or in other words, that the momentum along the fifth dimension needs to be quantized in units of  $\frac{1}{R}$ :

$$p_y = \frac{2\pi}{\lambda} \rightarrow p_y = \frac{2\pi n}{2\pi R} = \frac{n}{R}. \quad (1.6)$$

Plugging this quantization condition back into original 5D energy-momentum relation, we now see that every 5D field actually possesses an infinite amount of excitations of energy  $E_n$

$$E_n^2 = p_{x_1}^2 + p_{x_2}^2 + p_{x_3}^2 + m^2 + \frac{n^2}{R^2} \equiv \vec{p}^2 + M_n^2. \quad (1.7)$$

If we define  $M_n = \sqrt{m^2 + \frac{n^2}{R^2}}$  we can alternatively say in the 4D compactified theory every particle is accompanied by a tower of Kaluza-Klein (KK)-modes with identical quantum numbers but increasingly heavier masses  $M_n$ .

Even though it is possible to induce non-Abelian Yang-Mills theories through more involved compactification procedures in higher dimensions, the original Kaluza-Klein model is not suited to reproduce all SM physics. It is particularly not possible [11] to introduce chiral fermions, necessary for the weak interaction, into the original theory.

There is however a plethora of modern iterations of models with extra dimensions inspired by those historic attempts. Generally speaking they fall into two categories: those where the underlying 5D metric is intrinsically curved (*warped* geometry) and those where the metric is *flat*. Those models can be further classified as to how many of the fields in the model are localized on a Brane and how many get to penetrate the Bulk. Examples for a warped geometry include Randall-Sundrum models [12, 13], that confine all particles except the graviton to the Brane, and more recent attempts [14, 15] which also allow for SM fields to penetrate the Bulk. Large Extra dimensions [16, 17] constitute an example with a flat geometry but only gravity propagating inside Bulk, whereas Universal Extra Dimensions [8, 18] do not confine any fields to the Brane. A more detailed discussion can be found in [19], which we use as a general reference point. Many of these theories share a universal set of fundamental features, while some of the phenomenological details might differ from model to model. We chose the minimal setup of one Universal Extra Dimension (mUED) as a concrete framework for our studies.

In this thesis we try to shed light on the influence loop corrections have on the discovery potential of Universal Extra Dimensions scenarios along with how they help to shape their phenomenology, which in turn can serve as the base on which to build a search strategy. The thesis is structured in the following way:

In Chapter 2, we review the concrete theoretical models this work is based on. Our main focus is on the minimal Standard Model extension with one Universal Extra Dimension. We introduce the general concepts by the example of a  $\Phi^4$  toy model and give the full SM Lagrangian in Appendix A. Additionally, we describe the construction of the two-site Coloron model equipped with an exchange symmetry. It can be regarded as the low-energy effective theory of mUED, in which all KK-modes heavier than level-1 have been integrated out. This distinction becomes necessary since truncated mUED violates gauge invariance, making it ill-equipped for some of our later calculations. The Coloron model we present respects the full gauge symmetry, albeit non-linearly, making it a better suited framework. In Chapter 3, we describe the next-to-leading order (NLO) QCD corrections to the pair production of heavy color-octet vector bosons as they appear in the aforementioned Coloron model (or as the level-1 KK-gluons in the mUED version of QCD). We elaborate on several

subtleties concerning the gauge fixing and renormalization procedure, which are inherent to the production of heavy colored Vectors. The soft divergencies are treated through the two-cutoff phase-space slicing method, which we describe before utilizing it for the process at hand. We present the full NLO production cross section, discuss its scaling behavior, and the corresponding  $\kappa$ -factor.

In Chapter 4, we extend the analysis from the lowest KK-mode running in the loops, in order to quantify how much the previously truncated modes change the Coloron predictions. We apply and compare a number of approaches designed to extract meaningful results for the formally infinite sums of vertex diagrams. The most straightforward approach is an analytic summation over all modes in the compactified theory up to a hard cutoff scale  $\Lambda$ . Additionally, we present a general prescription on how to extract the asymptotic behavior of the vertex functions consistent with dimensional regularization. Finally we compare our results with those obtained from the exact functional renormalization group equation, applied to uncompactified QCD in 5D.

In Chapter 5, we investigate the impact that radiatively induced operators, localized on the boundary, have on the phenomenology of mUED. This is a twofold process. In step one we consider two-point functions that give rise to mass corrections of the KK-modes. These mass corrections significantly shape the decay channels of interest since the mass spectrum is almost degenerate at tree level. Secondly, we consider the KK-number violating coupling of a single level-2 mode into two SM modes within the complete mUED SM. The literature reports results for the logarithmic contributions to number of such mass corrections and couplings, while we present the full one-loop results, as well as some completely new, finite operators.

Through those couplings it would be possible to produce a single level-2 mode at say a collider and then detect the successive decay into a pair of SM modes without anything escaping. This represents an attractive search strategy (even though the modes under consideration are heavier than the level-1 modes discussed in Chapter 3), because even-parity modes are not bound by the pair production requirement that parity odd modes are limited by. We then discuss the phenomenological implications that come along with our findings.

In Chapter 6 we summarize our main results and provide an outlook that places them into

perspective.

## 2.0 THEORETICAL CONCEPTS

This chapter serves as a review of established theoretical concepts that are the foundation of the work this dissertation presents.

We begin by constructing  $\Phi^4$  theory in the mUED model and discuss important features that are relevant to our work. Additionally we describe how to implement the Standard Model in this framework, particularly the inclusion of chiral fermions and then present the final 4D Lagrangian in Appendix [A.1](#).

In the second part we discuss the so-called two-site Coloron model as a low-energy approximation of QCD in mUED. The Coloron is a non-linear sigma model, that describes the infrared behavior of a number of extra dimensional models, in energy regimes where all heavy modes but the first one are integrated out. The distinction between Coloron and UED models becomes necessary, however, since the truncated mUED version of QCD breaks 5D gauge invariance and is therefore not suited for the NLO calculation we present in Chapter [3](#).

## 2.1 UNIVERSAL EXTRA DIMENSIONS

The minimal UED scenario consists of one additional flat space-like dimension that is populated by all SM fields. The compactification procedure (shown in [Fig. 1](#)) initially follows the original one by Kaluza and Klein by confining the extra dimension to a finite volume and periodically identifying its ends. Therefore all fields that are functions of the fifth coordinate  $y$  are invariant under  $y \rightarrow y + 2\pi R$ .

However, to accommodate the chiral SM fermions, an additional breaking of 5D Lorentz invariance is necessary. This is achieved through so-called orbifold boundary conditions. Specif-

ically, the Lagrangian is required to be invariant under the  $\mathbb{Z}_2$  transformation  $y \rightarrow -y$ . The

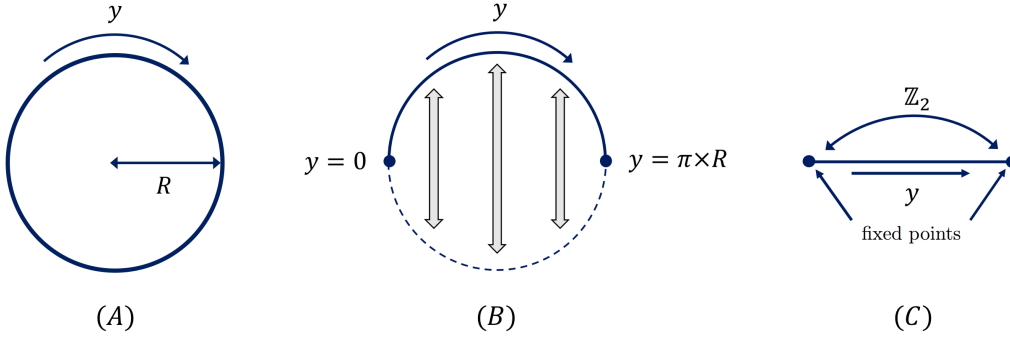


Figure 1: *UED orbifolding. (A) periodic boundary conditions leading to  $M_5 = M_4 \times S_1$ . (B) Mapping out a  $\mathbb{Z}_2$  symmetry by identifying two opposite sides of the circle. Leading to (C) two fixed points on the boundaries of the essentially flat bulk.*

extra dimension in this setup can be visualized as being curled up on a circle which is then pinched at two fixed points  $y = 0, \pi R$  and subsequently the upper and lower half circle are identified, leading to a mild topological defect in the resulting spacetime. The resulting space-time structure is, defects aside, still flat and described by the 5D metric tensor

$$\eta_{MN} = \begin{pmatrix} \eta_{\mu\nu} & 0 \\ 0 & -1 \end{pmatrix}, \quad (2.1)$$

with the regular 4D Minkowski metric  $\eta_{\mu\nu} = \text{diag}\{1, -1, -1, -1\}$ .

### 2.1.1 $\Phi^4$ in 5D - A Toy Example

After the qualitative description of the philosophy of minimal Universal Extra dimensions we now move on to summarizing the technical implementation within a field theoretical framework. As a first example we consider  $\Phi^4$  theory with the previously described single extra dimension compactified on an  $S_1/\mathbb{Z}_2$  orbifold and how to move from the 5D theory to the 4D effective theory.

The periodicity condition imposed on the fifth space-time coordinate implies that there exists a Fourier expansion of the field into discrete modes

$$\Phi(x, y) = \frac{1}{\sqrt{\pi R}} \left[ \phi_0(x) + \sqrt{2} \sum_{n=1}^{\infty} \left( \phi_n^+(x) \cos \frac{ny}{R} + \phi_n^-(x) \sin \frac{ny}{R} \right) \right]. \quad (2.2)$$

The appearance of a zero mode in the expansion is enabling us to account for the Standard Model modes, since the zero modes do not receive a mass contribution proportional to  $\frac{1}{R}$ . They are however an obstacle when describing fields that do not appear in the Standard Model and whose modes therefore all need to be heavy enough to evade detection. For this work, that is of particular importance for the fifth component of the vector fields,  $A_5$ , which is identified as the Goldstone boson stemming from the breaking of 5D Lorentz invariance through the compactification.

By introducing suitable boundary conditions at the fixed points we can project out the modes that are even/odd under the  $\mathbb{Z}_2$  symmetry and control which fields retain SM modes (which are even, since they are independent of  $y$ ). This can be accomplished by demanding that

$$\begin{aligned} \text{Neumann B.C.} \quad \partial_5 \Phi_+ &= 0 \quad \text{for even fields} \\ \text{Dirichlet B.C.} \quad \Phi_- &= 0 \quad \text{for odd fields,} \end{aligned} \quad (2.3)$$

on the boundary  $y = 0, \pi R$ .

The corresponding field expansion for the even/odd fields then becomes

$$\begin{aligned} \Phi_+(x, y) &= \frac{1}{\sqrt{\pi R}} \left[ \phi_0(x) + \sqrt{2} \sum_{n=1}^{\infty} \phi_n(x) \cos \frac{ny}{R} \right] \\ \Phi_-(x, y) &= \sqrt{\frac{2}{\pi R}} \sum_{n=1}^{\infty} \phi_n(x) \sin \frac{ny}{R} \end{aligned} \quad (2.4)$$

Now we can construct an effectively 4D Lagrangian by integrating the 5D  $\Phi^4$  theory over the fifth coordinate  $y$ , where for simplicity we assume  $\Phi$  to be  $\mathbb{Z}_2$  even

$$\mathcal{L} = \int_{-\pi R}^{\pi R} dy \left\{ \frac{1}{2} \partial_M \Phi(x, y) \partial^M \Phi(x, y) - \frac{m^2}{2} \Phi(x, y)^2 - \frac{\tilde{\lambda}}{4!} \Phi(x, y)^4 \right\}. \quad (2.5)$$

Next we substitute the expansion of the field in terms of modes into the Lagrangian and perform the integration over  $y$ . In the process it is useful to define a dimensionless coupling constant through

$$\lambda = \frac{\tilde{\lambda}}{\pi R}. \quad (2.6)$$

We arrive at an effectively 4D Lagrangian that firstly contains a kinetic piece, describing the dynamics of the the modes propagating in our flat space:

$$\mathcal{L}_{kin} = \underbrace{\frac{1}{2}\partial_\mu\phi_0\partial^\mu\phi_0 - \frac{m^2}{2}\phi_0^2}_{\text{SM mode}} + \sum_{n=1}^{\infty} \underbrace{\left\{ \frac{1}{2}\partial_\mu\phi_n\partial^\mu\phi_n - \frac{1}{2}\left(m^2 + \frac{n^2}{R^2}\right)\phi_n^2 \right\}}_{\text{level-n KK mode}} \quad (2.7)$$

The particle content of this theory is simply a scalar zero mode of mass  $m$  and an infinite tower of scalar fields with mass  $\sqrt{m^2 + \frac{n^2}{R^2}}$ , as the less rigorous argument made in the introduction suggested.

The second part of the Lagrangian, arising from the quartic interaction of the original 5D Lagrangian is then

$$\mathcal{L}_{int} = -\frac{\lambda}{4!} \left\{ \phi_0^4 + 6\phi_0^2 \sum_{n=1}^{\infty} \phi_n^2 + 2\sqrt{2}\phi_0 \sum_{k,l,m=1}^{\infty} \phi_k\phi_l\phi_m\Delta_{klm}^{(1)} + \frac{1}{2} \sum_{k,l,m,n=1}^{\infty} \phi_k\phi_l\phi_m\phi_n\Delta_{klmn}^{(2)} \right\} \quad (2.8)$$

where the  $\Delta$  symbols are permutations of the Kronecker delta function  $\delta_{ij}$ , that we define in Appendix A. The tree-level vertices of this 4D compactified theory are shown in Fig. 2. The defining phenomenological features of our model, relevant to our projects are in summary:

**Infinite KK towers** Every 5D field gives rise to an infinite tower of increasingly heavy modes in the 4D compactified theory. The zero modes then acquire a mass through electroweak symmetry breaking (EWSB), which in turn also shifts the mass of the higher KK-modes. All fields in the effective theory inherit the quantum numbers from the 5D field, despite the difference in mass.

**KK parity is an exact symmetry** After breaking 5D Lorentz invariance through the compactification a residual parity is still a good symmetry of the system. Geometrically this can be visualized as a reflection about the midpoint  $y = \pi R/2$  of the orbifold combined with application of the  $\mathbb{Z}_2$  transformation, rendering even-numbered field modes invariant

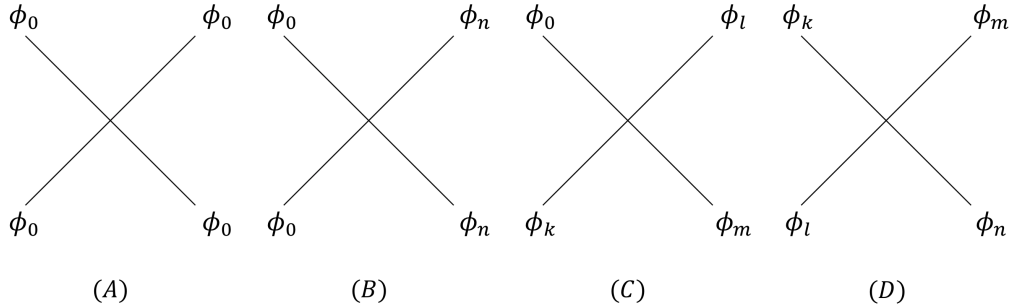


Figure 2:  $\phi^4$  tree-level vertices as they appear in the compactified theory. (A) pure SM vertex, (B) two SM modes and two KK modes, (C) one SM mode and three KK modes and (D) pure KK vertex. All Feynman diagrams in this thesis are produced using JAXODRAW 2.0 [20].

while odd-numbered modes change sign. In our specific model this statement is true at any loop order, so even radiatively induced processes cannot violate KK-parity. The lightest particles in the spectrum can therefore only be pair produced in experiments (cf. Chapter 3) as a direct consequence. Furthermore does the parity lead to KK contributions to low energy observables being at least loop-suppressed (cf. Chapter 4).

**KK number violation** The tree-level Lagrangian also conserves KK-number, which means that for all tree-level vertices appearing in the 4D effective theory (here especially (C) and (D) in Fig. 2) the mode numbers of the modes participating in the interactions obey

$$\begin{aligned}
 l \pm m \pm n &= 0 && \text{for 3-point vertices} \\
 k \pm l \pm m \pm n &= 0 && \text{for 4-point vertices.}
 \end{aligned}
 \tag{2.9}$$

Loop-induced processes however violate these conditions, as shown in Fig. 3. The left side is built from vertices that appear in the original tree-level Lagrangian and shrinks into the non-derivative, effective diagram shown on right, if we expand the loop integral in the region where the momentum transfer is small in comparison to the mass  $M_n$ .

Since extra dimension theories are non-renormalizable, there can be additional operators generated at a cut-off scale  $\Lambda$ . These are typically small, since the cut-off scale is estimated

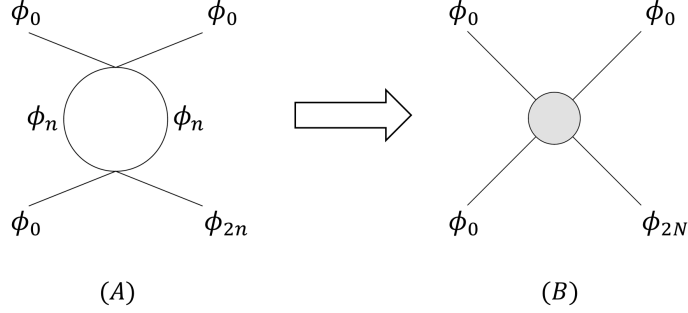


Figure 3: *Loop induced process that produces a four-point operator that violates KK-number but conserves parity (A) loop process set up of KK-number conserving tree-level vertices (B) the effective vertex breaks KK-number conservation by  $2n$  units. Note that there also exist similar S and U channel contributions to the effective vertex, which we omit here.*

to be  $\Lambda \sim \text{few} \times 10 R^{-1}$  [18, 22]. However, in general, the list of UV-induced operators could also include the boundary-localized KK-number violating interactions, and since they compete with loop-induced boundary terms, they can be phenomenologically relevant [85]. In the MUED scenario it is assumed that KK number is approximately conserved by the UV theory, so that the UV boundary terms are negligible.

The 5D operators corresponding to KK-number violating processes are localized on the boundaries, while the Bulk operators obey the rules 2.9. An operator leading to KK-number violating vertices would for example be

$$\mathcal{L}_{\text{Boundary}} \supset \frac{1}{2} \int_{-\pi R}^{\pi R} dy C_N [\delta(y) + \delta(y + \pi R)] \Phi(x, y)^N, \quad (2.10)$$

with some dimensionful coefficient  $C_N$ .

We can substitute the field for its Fourier expansion into modes as we did before, and performing the integration over  $y$  we find the 4D Lagrangian

$$\mathcal{L}_{\text{Boundary}} \supset \frac{C_N}{2(\pi R)^N} \left[ \left( \phi_0(x) + \sqrt{2} \sum_{n=1}^{\infty} \phi_n(x) \right)^N + \left( \phi_0(x) + \sqrt{2} \sum_{n=1}^{\infty} (-1)^n \phi_n(x) \right)^N \right] \quad (2.11)$$

Expanding the binomials into their power series we see how the KK-parity violating operators explicitly cancel

$$\mathcal{L}_{\text{Boundary}} \supset \frac{C_N}{(\pi R)^{N/2}} \left[ \phi_0(x)^N + \frac{N}{2} \phi_0(x)^{N-1} \sum_{n=1}^{\infty} \phi_n(x) (1 + (-1)^n) + \dots \right], \quad (2.12)$$

leaving us with a set of operators that violate the number conservation but continue to respect KK-parity

$$\mathcal{L}_{\text{Boundary}} \supset \frac{C_N}{(\pi R)^{N/2}} \left[ \phi_0(x)^N + N \phi_0(x)^{N-1} \sum_{n=1}^{\infty} \phi_{2n}(x) + \dots \right]. \quad (2.13)$$

Notice that the second term in the expansion reproduces the non-derivative operator, radiatively induced in Fig. 3.

How these radiatively induced operators shape the phenomenology for the mUED SM and the mass corrections they can induce is discussed in Chapter 5.

### 2.1.2 The Standard Model in 5D

The construction of an mUED model that reproduces the Standard Model at lowest order follows the same principle as our toy model, but exhibits some subtleties.

We promote all SM fields to 5D fields and from the usual SM interactions, one can construct the MUED Lagrangian and Feynman rules, see *e. g.* Refs, [8, 24–26]. It is however not possible to construct an equivalent of  $\gamma_5$  in 5D, so we have to induce SM fermions chiral under SU(2) in a different way [27]. We introduce two 5D fermion fields  $\Psi$  and  $\psi$  that are doublets and singlets under SU(2) respectively. Their Fourier expansion then reads

$$\begin{aligned} \Psi(x, y) &= \frac{1}{\sqrt{\pi R}} \left\{ \Psi_L(x) + \sqrt{2} \sum_{n=1}^{\infty} \left[ P_- \Psi_L^n(x) \cos \frac{ny}{R} + P_+ \Psi_R^n(x) \sin \frac{ny}{R} \right] \right\}, \\ \psi(x, y) &= \frac{1}{\sqrt{\pi R}} \left\{ \psi_R(x) + \sqrt{2} \sum_{n=1}^{\infty} \left[ P_+ \psi_R^n(x) \cos \frac{ny}{R} + P_- \psi_L^n(x) \sin \frac{ny}{R} \right] \right\}. \end{aligned} \quad (2.14)$$

Their zero modes are massless fermions that can be used to define chiral SM fermion through

$$\psi_{\text{SM}} = P_L \Psi_L + P_R \psi_R \quad (2.15)$$

with the usual 4D projection operators  $P_{L/R} = \frac{1}{2}(1 \pm \gamma_5)$ . Whereas the higher KK-modes combine to two sets of vector-like fermions, that are doublets/singlets under SU(2).

After having constructed chiral fermions the ingredients of our mUED version of the Standard Model are complete. We summarize the quantum numbers of all fields involved in Tab. 1. Note that every 4D vector field  $A_\mu$  is accompanied by a Goldstone boson  $A_5$ . For practical

Field	SU(3) <sub>C</sub>	SU(2) <sub>L</sub>	U(1) <sub>Y</sub>	$\mathbb{Z}_2$
$G^M \equiv (G^\mu, G^5)$	adj.	–	–	(+, –)
$W^M \equiv (W^\mu, W^5)$	–	adj.	–	(+, –)
$B^M \equiv (B^\mu, B^5)$	–	–	adj.	(+, –)
$(Q_L, Q_R)$	<b>3</b>	<b>2</b>	–1/6	(+, –)
$(u_L, u_R)$	<b>3</b>	–	+2/3	(–, +)
$(d_L, d_R)$	<b>3</b>	–	–1/3	(–, +)
$(L_L, L_R)$	–	<b>2</b>	–1/2	(+, –)
$(e_L, e_R)$	–	–	–1	(–, +)
$\Phi$	–	<b>2</b>	+1/2	+

Table 1: *Field content of the minimal universal extra dimension (MUED) model and their gauge and  $\mathbb{Z}_2$  quantum numbers.*

calculations, one also needs to introduce gauge-fixing and ghost terms for the 5D gauge fields  $V^M$  ( $V = G, W, B$ ). In this work, a covariant gauge fixing is employed, which has the form

$$\mathcal{L}_{\text{gf}} = \frac{1}{2} \int_{-\pi R}^{\pi R} dx^5 \left[ -\frac{1}{2\xi} (\partial^\mu V_\mu^a - \xi \partial_5 V_5^a)^2 \right], \quad (2.16)$$

$$\mathcal{L}_{\text{ghost}} = \frac{1}{2} \int_{-\pi R}^{\pi R} dx^5 \left[ \bar{c}^a (-\partial^\mu \partial_\mu + \xi \partial_5^2) c^a + g^{(5)} f^{abc} (-\partial^\mu \bar{c}^a G_\mu^c c^b + \xi \partial_5 \bar{c}^a G_5^c c^b) \right]. \quad (2.17)$$

where  $c^a$  and  $\bar{c}^a$  are 5D ghost and anti-ghost fields, respectively,  $a, b, c$  are adjoint gauge indices,  $f^{abc}$  is the non-Abelian structure constant, and  $g^{(5)}$  denotes the 5D gauge couplings for each of the three vector fields. For simplicity, the choice  $\xi \equiv 1$  for the gauge parameter is used throughout this work.

For the top quark, the SM Higgs Yukawa coupling cannot be ignored. It leads to mixing

between the singlets  $u_n$  and first component of the  $Q_n$  fields, which we call  $U_n$ , to remain consistent with notation of App. H of Ref. [26]. The mass matrix reads

$$\begin{pmatrix} \bar{U}_n & \bar{u}_n \end{pmatrix} \begin{pmatrix} M_n & m_t \\ m_t & -M_n \end{pmatrix} \begin{pmatrix} U_n \\ u_n \end{pmatrix}, \quad (2.18)$$

Diagonalizing this mass matrix leads to two degenerate mass eigenstates  $T_n$  and  $T'_n$  given by

$$\begin{pmatrix} U_n \\ u_n \end{pmatrix} = \begin{pmatrix} \cos \theta_n^T & \gamma_5 \sin \theta_n^T \\ \sin \theta_n^T & -\gamma_5 \cos \theta_n^T \end{pmatrix} \begin{pmatrix} T_n \\ T'_n \end{pmatrix} \quad (2.19)$$

with mass and mixing angle

$$M_T = \sqrt{M^2 + m_t^2}, \quad \tan 2\theta_T = \frac{m_t}{M}. \quad (2.20)$$

Even in the limit of massless SM quarks ( $\theta_n^T = 0$ ) the diagonalized mass eigenstates do not coincide with the original flavor eigenstates, due to the fact that the diagonal elements have a relative sign between them. The transformation reduces in that case to  $u^n \rightarrow -\gamma_5 u_n$ .

Similarly we have to diagonalize the mass matrix for the electroweak KK-bosons. We can define the KK-photon  $A_\mu^n$  and KK-Z  $Z_\mu^n$  through the Kaluza-Klein generalization of the Weinberg angle

$$\begin{pmatrix} A_n^\mu \\ Z_n^\mu \end{pmatrix} = \begin{pmatrix} \cos \theta_n & \sin \theta_n \\ -\sin \theta_n & \cos \theta_n \end{pmatrix} \begin{pmatrix} B_n^\mu \\ W_{3,n}^\mu \end{pmatrix}. \quad (2.21)$$

This redefinition is necessary to diagonalize the mass terms, which in the  $B_n^\mu$  and  $W_{3,n}^\mu$  basis take the form

$$\begin{pmatrix} B_n^\mu & W_{3,n}^\mu \end{pmatrix} \begin{pmatrix} \frac{n^2}{R^2} + \hat{\delta}m_{B_n}^2 + \frac{1}{4}g_1^2v^2 & \frac{1}{4}g_1g_2v^2 \\ \frac{1}{4}g_1g_2v^2 & \frac{n^2}{R^2} + \hat{\delta}m_{W_n}^2 + \frac{1}{4}g_2^2v^2 \end{pmatrix} \begin{pmatrix} B_{\mu,n} \\ W_{3,\mu,n} \end{pmatrix}, \quad (2.22)$$

where  $\hat{\delta}m^2$  are the mass corrections stemming from the one-loop self-energies of the electroweak gauge bosons in question.

Analogously we define the charged KK-W bosons as  $W_{\pm,n}^\mu = \frac{1}{\sqrt{2}} (W_{1,n}^\mu \pm iW_{2,n}^\mu)$ .

## 2.2 THE TWO-SITE COLORON MODEL

We now describe the construction of the two-site Coloron model as we will employ it in our calculation in Chapter 3. It serves to describe the low-energy physics of mUED and other extra dimensional models after all KK-modes heavier than  $n = 1$  have been integrated out. The two-site Coloron model is based on an extension of the strong gauge group to the product group  $SU(3)_1 \times SU(3)_2$ , which is broken down to  $SU(3)_C$  by a non-linear sigma model. In addition, invariance under the  $\mathbb{Z}_2$  transformation  $\mathcal{P}$  is imposed, which interchanges the two  $SU(3)$  groups:

$$\mathcal{P} : \quad SU(3)_1 \leftrightarrow SU(3)_2. \quad (2.23)$$

This exchange symmetry mimics the KK parity of UED. The Lagrangian of the model can be divided into three parts,

$$\mathcal{L} = \mathcal{L}_{\text{gauge}} + \mathcal{L}_{\text{ferm}} + \mathcal{L}_{\text{gf}}. \quad (2.24)$$

The gauge part is given by

$$\mathcal{L}_{\text{gauge}} = -\frac{1}{4}G_{1\mu\nu}G_1^{\mu\nu} - \frac{1}{4}G_{2\mu\nu}G_2^{\mu\nu} + \frac{f^2}{4}\text{tr}\{D_\mu\Sigma D^\mu\Sigma^\dagger\}. \quad (2.25)$$

Here  $G_{i\mu\nu}$  are the field strength tensors of  $SU(3)_i$  ( $i = 1, 2$ ), with gauge couplings  $g_1 = g_2 \equiv g$ .  $\Sigma$  denotes the non-linear sigma field

$$\Sigma = \exp(2i\pi^A T^A / f), \quad (2.26)$$

where  $A = 1, \dots, 8$  is implicitly summed over,  $T^A$  are the  $SU(3)$  generators,  $f$  is a constant of mass dimension, and  $\pi^A$  are the Goldstone fields of the broken  $SU(3)$ . Its covariant derivative is given by

$$D_\mu\Sigma = \partial_\mu\Sigma - igG_{1\mu}^A T^A \Sigma + ig\Sigma G_{2\mu}^A T^A. \quad (2.27)$$

Under  $SU(3)_1 \times SU(3)_2$ , the  $\Sigma$  field transforms as a bi-fundamental,

$$\Sigma \rightarrow U_1 \Sigma U_2^\dagger. \quad (2.28)$$

The  $\Sigma$  field is responsible for the breaking of  $SU(3)_1 \times SU(3)_2$  to the vectorial subgroup  $SU(3)_C$ . The gauge mass eigenstates in the broken phase are

$$G_\mu^A = \frac{1}{\sqrt{2}}(G_{1\mu}^A + G_{2\mu}^A), \quad C_\mu^A = \frac{1}{\sqrt{2}}(G_{1\mu}^A - G_{2\mu}^A). \quad (2.29)$$

Here  $G_\mu^A$  is the (massless) gluon field of  $SU(3)_C$  with coupling strength  $g_s = g/\sqrt{2}$ , whereas  $C_\mu^A$  is the massive Coloron field with mass  $M = g_s f$ , which ‘‘eats’’ the Goldstone fields  $\pi^A$ . Eq. (2.25) has the same form as for the Coloron model in Ref. [28] with the additional constraint that the two gauge groups have equal coupling strength. The latter requirement is a consequence of the  $\mathcal{P}$  parity, which was not considered in Ref. [28]. Under this parity

$$\mathcal{P} : \quad G_{1\mu}^A \leftrightarrow G_{2\mu}^A, \quad G_\mu^A \rightarrow G_\mu^A, \quad C_\mu^A \rightarrow -C_\mu^A, \quad \Sigma \rightarrow \Sigma^\dagger. \quad (2.30)$$

Since  $C_\mu^A$  is odd under  $\mathcal{P}$ , the massive Colorons can only be produced in pairs.

The fermion part of the Lagrangian reads

$$\begin{aligned} \mathcal{L}_{\text{ferm}} = & \bar{q}_1 i \not{D}_1 q_1 + \bar{q}_2 i \not{D}_2 q_2 + \bar{q}' i \not{D}_V q' - Y [\bar{q}_1 \xi q' - \bar{q}_2 \xi^\dagger q' + \text{h.c.}] \\ & + \bar{u}_1 i \not{D}_1 u_1 + \bar{u}_2 i \not{D}_2 u_2 + \bar{u}' i \not{D}_V u' - Y [\bar{u}_1 \xi u' - \bar{u}_2 \xi^\dagger u' + \text{h.c.}] \\ & + \bar{d}_1 i \not{D}_1 d_1 + \bar{d}_2 i \not{D}_2 d_2 + \bar{d}' i \not{D}_V d' - Y [\bar{d}_1 \xi d' - \bar{d}_2 \xi^\dagger d' + \text{h.c.}]. \end{aligned} \quad (2.31)$$

Here  $\psi_1$ ,  $\psi_2$  and  $\psi'$  are quark fields in the fundamental representation of  $SU(3)_1$ ,  $SU(3)_2$  and  $SU(3)_C$ , respectively ( $\psi = q, u, d$ ). The  $\psi = q$  fields are chiral doublets under the weak  $SU(2)_W$  group, whereas  $\psi = u, d$  are singlets. The relevant quantum numbers and chirality of the quark fields is summarized in Tab. 2. Their covariant derivatives read

$$\begin{aligned} D_{1\mu} \psi_1 &= \partial_\mu \psi_1 - ig G_{1\mu}^A T^A \psi_1 + \dots, \\ D_{1\mu} \psi_2 &= \partial_\mu \psi_2 - ig G_{2\mu}^A T^A \psi_2 + \dots, & [\psi = q, u, d] \\ D_{V\mu} \psi' &= \partial_\mu \psi' - \frac{ig}{\sqrt{2}} (G_{1\mu}^A + G_{2\mu}^A) T^A \psi' + \dots, \end{aligned} \quad (2.32)$$

where the dots indicate electroweak interactions, which are ignored in this work. Furthermore,  $\xi$  is the ‘‘square root’’ sigma field according to the CCWZ construction [29],

$$\xi = \exp(i\pi^A T^A / f). \quad (2.33)$$

Field	Chirality	SU(2) <sub>W</sub>	SU(3) <sub>1</sub>	SU(3) <sub>2</sub>	SU(3) <sub>C</sub>
$q_1$	L	<b>2</b>	<b>3</b>	<b>1</b>	–
$q_2$	L	<b>2</b>	<b>1</b>	<b>3</b>	–
$q'$	R	<b>2</b>	–	–	<b>3</b>
$u_1$	R	<b>1</b>	<b>3</b>	<b>1</b>	–
$u_2$	R	<b>1</b>	<b>1</b>	<b>3</b>	–
$u'$	L	<b>1</b>	–	–	<b>3</b>
$d_1$	R	<b>1</b>	<b>3</b>	<b>1</b>	–
$d_2$	R	<b>1</b>	<b>1</b>	<b>3</b>	–
$d'$	L	<b>1</b>	–	–	<b>3</b>

Table 2: *Quantum numbers and chirality of the quark fields in the two-site symmetric Coloron model.*

Under  $SU(3)_1 \times SU(3)_2$ , these fields transform as

$$\psi_1 \rightarrow U_1 \psi_1, \quad \psi_2 \rightarrow U_2 \psi_2, \quad \psi' \rightarrow U_V \psi', \quad \xi \rightarrow U_1 \xi U_V^\dagger = U_V \xi U_2^\dagger, \quad (2.34)$$

where  $U_V$  is the transformation matrix of the fundamental representation of the vectorial subgroup  $SU(3)_C$ . The effect of  $\mathcal{P}$  parity on the fermion fields is

$$\mathcal{P} : \quad \psi_1 \leftrightarrow \psi_2, \quad \psi' \rightarrow -\psi', \quad \xi \rightarrow \xi^\dagger. \quad (2.35)$$

The introduction of the  $\psi'$  fields is necessary to be able to write down invariant Yukawa terms (with coupling strength  $Y$ ) in eq. (2.31).

The physical quark mass eigenstates are

$$\begin{aligned} \psi &= \frac{1}{\sqrt{2}}(\psi_1 + \psi_2), & [\psi = q, u, d] \\ \Psi &= \frac{1}{\sqrt{2}}(\psi_1 - \psi_2)P_L + \psi'P_R, & [\Psi = Q, U, D] \end{aligned} \quad (2.36)$$

where  $P_{L,R} = \frac{1}{2}(1 \pm \gamma_5)$ . Here the  $\psi$  fields are massless chiral  $\mathcal{P}$ -even SM-like quark fields, whereas the  $\Psi$  fields are  $\mathcal{P}$ -odd fermion fields with a vector-like mass  $M_\Psi = \sqrt{2}Y$ . In general, the Yukawa coupling  $Y$  is a free parameter, but for the sake of analogy to UED we impose

$$Y = M/\sqrt{2}, \quad \text{i.e.} \quad M_\Psi = M. \quad (2.37)$$

The final component of the model is the gauge-fixing and ghost term. For a covariant gauge it can be defined in the following  $\mathcal{P}$ -symmetric form,

$$\mathcal{L}_{\text{gf}} = -\frac{1}{2}(\mathcal{F}_1^A)^2 - \frac{1}{2}(\mathcal{F}_2^A)^2 + \sum_{i,j=1}^2 \bar{u}_i^A \frac{\delta \mathcal{F}_i^A}{\delta \alpha_j^B} u_j^B, \quad (2.38)$$

where

$$\begin{aligned} \mathcal{F}_1^A &= \frac{1}{\sqrt{\xi}} G_{1\mu}^A + \sqrt{\xi} \frac{g}{2} f \pi^A, \\ \mathcal{F}_2^A &= \frac{1}{\sqrt{\xi}} G_{2\mu}^A - \sqrt{\xi} \frac{g}{2} f \pi^A, \end{aligned} \quad (2.39)$$

and  $\delta\alpha_i^A$  is the parameter of an infinitesimal  $\text{SU}(3)_i$  gauge transformation. For the calculation presented in the following sections, the Feynman gauge  $\xi = 1$  has been employed. In this gauge, the unphysical Goldstone fields  $\pi^A$  receive a mass  $M = g_s f = gf/\sqrt{2}$  from eq. (2.38). The ghost fields mix to form a  $\mathcal{P}$ -even massless gluon ghost  $u_g = \frac{1}{\sqrt{2}}(u_1 + u_2)$  and a  $\mathcal{P}$ -odd Coloron ghost  $u_C = \frac{1}{\sqrt{2}}(u_1 - u_2)$  with mass  $M$ . Thus one obtains

$$\begin{aligned} \mathcal{L}_{\text{gf}} &= -\frac{1}{2} \left[ (\partial^\mu G_\mu^A)^2 + (\partial^\mu C_\mu^A)^2 \right] - \frac{M^2}{2} (\pi^A)^2 - M \partial^\mu C_\mu^A \pi^A \\ &\quad - \bar{u}_g^A \partial^2 u_g^A - \bar{u}_C^A (\partial^2 + M^2) u_C^A + g_s f_{ABC} \bar{u}_g^A \partial^\mu (u_g^B G_\mu^C + u_C^B C_\mu^C) \\ &\quad + g_s f_{ABC} \bar{u}_C^A \partial^\mu (u_g^B C_\mu^C + u_C^B G_\mu^C) + g_s M f_{ABC} (\bar{u}_g^A u_C^B - \bar{u}_C^A u_g^B) \pi^C. \end{aligned} \quad (2.40)$$

In summary, the two-site symmetric Coloron model defined in this way contains several states with mass  $M$  in addition to the SM particle content. Besides the Coloron vector-boson, heavy vector-like quarks are required to enforce the  $\mathcal{P}$ -parity as an exact symmetry. This model can be viewed as a low-energy approximation of the 5-dimensional minimal UED model (mUED) with compactification radius  $R = M^{-1}$ , where only the zero modes and first KK excitations are kept as dynamical degrees of freedom. Note, however, that the Coloron model is not identical to a simple truncation of mUED at the  $n = 1$  level, since such a

truncated UED model would violate gauge invariance [30], whereas the model presented here respects the full gauge symmetry, albeit non-linearly. In fact, the Feynman rules for the two-site Coloron model and the first KK excitation in mUED are mostly identical, but there are a few differences, which are mentioned in Appendix A.2.

In a more general sense, the two-site symmetric Coloron model can be regarded as a low-energy description of any model with massive color-octet vector bosons that are odd under some (approximate) parity.

### 3.0 COLORON PAIR PRODUCTION AT NLO

We now consider the pair production of heavy vector color octets at Hadron colliders, as they appear in mUED as the level-1 KK-partner of the gluon, as described in [31]. QCD corrections have been computed for a number of pair production processes of colored BSM particles, including (but not limited to) squark and gluino production in the Minimal Supersymmetric Standard Model (MSSM) [32–34], leptoquark pair production [35], production of massive vector quarks [36], and pair production of scalar color octet bosons [37]. The corrections were generically found to be sizeable and important to reduce the large dependence of tree-level results on the renormalization scale. Thus, for a robust prediction of the production of colored BSM particles at hadron colliders, the inclusion of next-to-leading order (NLO) QCD corrections seems mandatory.

QCD corrections to production of single vector octets have been studied in Refs. [28, 38]. The Coloron model our analysis is based on (cf. chapter 2) is similar in spirit but equipped with an exchange symmetry to mimic KK-parity.

#### 3.1 OBTAINING THE CROSS SECTION THROUGH PHASE SPACE SLICING

Massive Colorons can be pair produced at hadron colliders, such as the LHC. The tree-level process  $pp \rightarrow CC$  can be divided into two partonic sub-channels,  $q\bar{q} \rightarrow CC$  and  $gg \rightarrow CC$ , with the relevant diagrams shown in Fig. 4. Note that at leading order this process is identical to of KK gluon pair production in mUED.

At NLO, one needs to consider one-loop corrections to the subprocesses  $q\bar{q} \rightarrow CC$  and  $gg \rightarrow$

$CC$ , as well as real emission of an extra gluon at tree-level,  $q\bar{q} \rightarrow CCg$  and  $gg \rightarrow CCg$ . A few sample diagrams are shown in Figs. 5 and 6. Both the loop contributions and real emission contributions are separately IR divergent, but the divergencies cancel in the combined result. Additionally, the quark-gluon induced subprocesses  $qg \rightarrow CCq$  and  $\bar{q}g \rightarrow CC\bar{q}$  appear for the first time at NLO. At NLO, the predictions for Coloron pair production become sensitive to assumptions about the UV completion. The renormalization procedure employed here takes a bottom-up approach, assuming that the running couplings are defined at the mass scale  $M$  of the Colorons<sup>†</sup>. In the next subsection, the renormalization scheme is discussed in more detail.

### 3.1.1 Renormalization

In this work, the renormalization is performed by using the on-shell scheme for the wave-function and mass renormalization of the physical states and  $\overline{\text{MS}}$  renormalization for the strong coupling constant. However, due to the fact that the two-site Coloron model is fundamentally a non-renormalizable theory, there are several subtleties that need to be addressed. These will be discussed in this section, together with a brief summary of the remaining aspects of the renormalization.

For the external states the wave-function renormalization constants

$$\delta Z_L^\psi = \delta Z_R^\psi \quad [\psi = q, u, d], \quad \delta Z^g, \quad \delta Z^C \quad (3.1)$$

are introduced for the left- and right-handed (massless) SM quarks, the gluons, and the massive Colorons, respectively. As usual, their values are determined through the residues of the renormalized propagators, leading to

$$\delta Z_{L,R}^\psi = -\Re\{\Sigma_{L,R}^\psi(0)\}, \quad \delta Z^g = -\Re\left\{\frac{\partial}{\partial(p^2)}\Sigma^g(0)\right\}, \quad \delta Z^C = -\Re\left\{\frac{\partial}{\partial(p^2)}\Sigma^C(M^2)\right\}, \quad (3.2)$$

where  $\Sigma_{L,R}^\psi(p^2)$ ,  $\Sigma^g(p^2)$  and  $\Sigma^C(p^2)$  are the left/right-handed quark self-energies, transverse gluon self-energy and transverse Coloron self-energy, respectively.

---

<sup>†</sup>If instead the couplings are defined at a high scale  $\Lambda \gg M$ , this may lead to additional moderately-sized contributions to the NLO result. This will be explored in the next chapter. However, experience from other BSM calculations indicates that the numerically dominant part of the NLO QCD is generated by SM gluon exchange contributions and thus does in this case not depend on the details of the UV completion.

The masses of the Colorons and massive quarks are renormalized according to the on-shell prescriptions

$$\delta M_C^2 = \Re\{\Sigma^C(M^2)\}, \quad \delta M_\Psi = \frac{M}{2} \Re\{\Sigma_L^\psi(M^2) + \Sigma_R^\psi(M^2) + 2\Sigma_S^\psi(M^2)\}. \quad (3.3)$$

The mass parameter in the gauge-fixing term gets renormalized in the same way as the Coloron mass.

Note that, while we assume that the Colorons and massive quarks have the same mass  $M$  at tree-level, as in mUED, they are technically independent parameters in the Coloron model and thus receive different mass counterterms. In mUED, in fact, the degeneracy of the KK masses is also broken at the one-loop level due to boundary terms [39], which we investigate in Chapter 5.

Following the analogy to mUED, therefore, we assume that the mass difference between the Coloron mass,  $M_C$ , and the vector-like quark mass,  $M_\Psi$ , is small:  $|M_C - M_\Psi|/M \sim \mathcal{O}(\alpha_s)$ . Within the contributions to  $\mathcal{O}(\alpha_s)$  we thus set  $M_C = M_\Psi = M$  but allow the masses to deviate by a small numerical amount in the tree-level contribution, consistent with this power counting.

The strong coupling constant is renormalized in the 5-flavor  $\overline{\text{MS}}$  scheme. In this scheme, only the gluons and five light quarks are included in the scale evolution of the  $\alpha_s$ , whereas the scale dependence of the top quark, Coloron and heavy vector quark loops is accounted for through explicit logarithms in the finite part of the counterterm. See e.g. Ref. [32] for an application of this scheme in the context of supersymmetry. For the  $g\psi\bar{\psi}$ ,  $ggg$ ,  $g\Psi\bar{\Psi}$  and  $gCC$  gauge coupling, this leads to

$$g_s^{\text{bare}} \rightarrow g_s(\mu) (1 + \delta Z_g) \quad (3.4)$$

$$\delta Z_g = \frac{\alpha_s(\mu)}{4\pi} \left[ -\frac{\beta_0}{2} \left( \frac{1}{\epsilon} - \gamma_E + \log(4\pi) \right) - \frac{1}{3} \log \frac{m_t^2}{\mu^2} + \left( \frac{21}{4} - \frac{2}{3}n_q \right) \log \frac{M^2}{\mu^2} - \frac{2}{3} \log \frac{M_T^2}{\mu^2} \right], \quad (3.5)$$

$$\beta_0 = \beta_0^L + \beta_0^H = \left( 11 - \frac{2}{3}n_q \right) + \left( \frac{21}{2} - \frac{4n_q + 6}{3} \right), \quad (3.6)$$

where  $n_q = 5$ , and  $\mu$  is the renormalization scale, which is taken equal to the regularization scale for simplicity. Furthermore,  $\epsilon = (4 - D)/2$ , where  $D$  is the number of dimensions in

dimensional regularization.

To be consistent at our order in perturbation theory requires the coupling of the Born contribution to the cross section to run at two loop. The two-loop beta-function for  $n_q$ -flavor QCD reads

$$\mu \frac{\partial \alpha_s}{\partial \mu} = - \left( \frac{11}{3} C_A - \frac{4}{3} T_f n_q \right) \frac{\alpha_s}{2\pi} - \left( \frac{17}{3} C_A^2 - \frac{10}{3} C_A T_f n_q - 2 C_F T_f n_q \right) \left( \frac{\alpha_s}{2\pi} \right)^2, \quad (3.7)$$

and was taken from [40].

On the other hand, for the  $C\psi\Psi$  and  $gC\pi$  couplings (where  $\pi$  is a Goldstone boson), one needs different coupling counterterms. This is not entirely surprising, since these couplings are not  $SU(3)_C$  gauge interactions, but are instead related to the larger non-linear  $SU(3)_1 \times SU(3)_2$  symmetry.

To determine the  $\mu$ -dependence of these couplings, one may assume that all gluon and Coloron coupling have the same value at  $\mu = M$ , and the  $C\psi\Psi$  and  $gC\pi$  couplings do not effectively run for  $\mu < M$ . Thus one finds

$$C\psi\Psi : \quad \delta Z'_g = \frac{\alpha_s(\mu)}{4\pi} \left[ - \left( 10 - \frac{2}{3} n_q \right) \left( \frac{1}{\epsilon} - \gamma_E + \log(4\pi) \right) + \frac{\beta_0^L}{2} \log \frac{M^2}{\mu^2} \right], \quad (3.8)$$

$$gC\pi : \quad \delta Z''_g = \frac{\alpha_s(\mu)}{4\pi} \left[ - \left( \frac{21}{4} - \frac{n_q}{2} \right) \left( \frac{1}{\epsilon} - \gamma_E + \log(4\pi) \right) + \frac{\beta_0^L}{2} \log \frac{M^2}{\mu^2} \right]. \quad (3.9)$$

In addition, one needs a counterterm for the vacuum expectation value of the sigma field,  $\Sigma$ . This counterterm, denoted by the symbol  $\delta t$ , appears in the renormalization of the Goldstone self-energy:

$$-----\star----- = i\delta_{AB} \frac{\delta t}{M}. \quad (3.10)$$

In a Higgs-like theory, this counterterm is usually determined from the requirement that the renormalized tadpole terms of the Higgs field should vanish. For the Coloron model, however, the symmetry breaking mechanism is left unspecified, and the radial degrees of freedom of the sigma field (which correspond to the Higgs scalars in a weakly coupled symmetry breaking sector) are assumed to be integrated out. Therefore the tadpole condition cannot be used here.

On the other hand, as explained for example in Ref. [41], the counterterm for the vacuum

expectation also appears in the Goldstone self-energy  $\Sigma^\pi(p^2)$ . Thus one can impose the renormalization condition

$$\delta t = -M \Sigma^\pi(0), \quad (3.11)$$

which in a Higgs-like theory is completely equivalent to the tadpole condition.

### 3.1.2 Infrared Divergencies and Phase Space Slicing

After removing the ultraviolet divergencies, that appear when the loop momentum goes to infinity, through renormalization we now have to consider what happens at the opposite end of the spectrum. Some loop functions develop infrared divergencies when a massless propagator goes on-shell (soft divergence) or the momentum of two neighboring massless particles align (collinear divergence). They manifest as poles in  $\epsilon$ , analogous to the UV divergencies, in dimensional regularization.

Those soft singularities luckily cancel order-by-order in perturbation theory between the virtual contributions to the process and the bremsstrahlung corrections to the corresponding Born-level process (Kinoshita-Lee-Nauenberg Theorem [42]). The real emission of a gluon from an external leg is shown exemplary in Fig. 7 and we see that the singularity arises through the propagator of the (massless) quark, either when the energy of the emitted gluon reaches zero or the angle  $\theta$  between the quark and the gluon closes. The initial state, collinear divergencies of our process do not cancel through the real emission diagrams but are absorbed into the redefinition of the parton density functions.

One way to carry out the cancelation described explicitly is the phase-space slicing with two cutoffs, first described in [43]. We follow a more modern prescription, as summarized in [44]. According to this scheme, the phase space integration of the  $2 \rightarrow N + 1$  real radiation contribution is split into three categories

$$\begin{aligned} \sigma_{A+B \rightarrow N+1} &= \frac{1}{2s} \int d\Gamma_{N+1} |\mathcal{M}_{N+1}|^2 \\ &= \frac{1}{2s} \left[ \int_S d\Gamma_{N+1} |\mathcal{M}_{N+1}|^2 + \int_C d\Gamma_{N+1} |\mathcal{M}_{N+1}|^2 + \int_H d\Gamma_{N+1} |\mathcal{M}_{N+1}|^2 \right]. \end{aligned} \quad (3.12)$$

Here  $d\Gamma_{N+1}$  is the  $N + 1$ -particle phase-space measure given by

$$d\Gamma_{N+1} = (2\pi)^D \delta^D \left( p_1 + p_2 - \sum_{i=1}^{N+1} k_i \right) \prod_{n=1}^{N+1} \frac{d^{D-1} k_n}{2(2\pi)^{D-1} E_n} \quad (3.13)$$

and  $\mathcal{M}_{N+1}$  the  $2 \rightarrow N + 1$  matrix element.

The integrals are over the regions of phase-space, where the gluon becomes soft ( $S$ ), hard-collinear ( $C$ ) and hard-collinear ( $H$ ). In those limits we can approximate the integrals and analytically extract the divergencies that will cancel against those from the virtual contributions, as we describe below. In a final step we integrate the divergence-free hard-collinear region numerically and match it to the finite pieces left after all poles have been canceled.

**3.1.2.1 The Soft Limit** The integration region denoted by  $S$  is the phase-space region where the the gluon that has been radiated off becomes soft. This region is characterized through

$$0 \leq E_g \leq \delta_S \frac{\sqrt{\hat{s}}}{2} \quad (3.14)$$

by the cutoff parameter  $\delta_S$  and a typical energy scale, here the partonic center-of-mass energy  $\hat{s}$ . We can start by factorizing the  $N + 1$  body phase-space into the  $N$  body one and one for the gluon

$$d\Gamma_{N+1} \Big|_{\text{soft}} = d\Gamma_N \frac{d^{D-1} k_g}{2(2\pi)^{D-1} E_g}. \quad (3.15)$$

performing the  $D$  dimensional angular integral we arrive at simple factorization formula

$$d\Gamma_{N+1} \Big|_{\text{soft}} = d\Gamma_N \frac{\Gamma[1 - \epsilon]}{\Gamma[1 - 2\epsilon]} \frac{\pi^\epsilon}{8\pi^3} d\Gamma_g, \quad (3.16)$$

so all that needs to be performed is the integral over the gluons energy, inside the boundaries [3.14](#), given through

$$d\Gamma_g = \int_0^{\delta_S \sqrt{\hat{s}}/2} dE_g d\theta_1 d\theta_2 E_g^{1-2\epsilon} \sin^{1-2\epsilon} \theta_1 \sin^{-2\epsilon} \theta_2. \quad (3.17)$$

We similarly decompose the  $2 \rightarrow N + 1$  matrix element into the Born-level matrix element  $2 \rightarrow N$  and an eikonal factor, by expanding for small energies  $E_g$

$$|\mathcal{M}_{N+1}|^2 \Big|_{\text{soft}} = -g^2 \mu_R^{2\epsilon} |\mathcal{M}_N|^2 \sum_{i,j} \frac{-p_i \cdot p_j}{(p_i \cdot k_g)(p_j \cdot k_g)}, \quad (3.18)$$

where in the case of dimensional regularization the renormalization scale  $\mu_R$  enters to ensure that both sides of the equation have the same mass dimension.

Finally we can combine the factorized phase-space and matrix element and arrive at an expression for the soft contribution to the cross section

$$\int_S d\Gamma_{N+1} |\mathcal{M}_{N+1}|^2 = \int d\Gamma_N |\mathcal{M}_N|^2 \times \frac{\alpha_s}{2\pi} \frac{\Gamma(1-\epsilon)}{\Gamma(1-2\epsilon)} \left( \frac{4\pi\mu_R^2}{s} \right)^\epsilon \sum_{i,j} \int d\Gamma_g \frac{-p_i \cdot p_j}{(p_i \cdot p_g)(p_j \cdot p_g)}. \quad (3.19)$$

The Eikonal factor can be integrated analytically and contains the relevant pole. They can be found in the literature [44, 45]. The integrals relevant for our calculation are listed in B.2.

**3.1.2.2 The Collinear Limit** The integration region denoted by  $C$  is the phase-space region where the the gluon that has been radiated off becomes collinear to another massless particle, but the energy remains in the hard region. This region is characterized through

$$\delta_s \frac{\sqrt{\hat{s}}}{2} < E_g, \quad 1 - \cos \theta_{gi} \leq \delta_c \frac{\sqrt{\hat{s}}}{E_g}, \quad (3.20)$$

where  $\theta_{gi}$  is the angle enclosed between the gluon and quark, as it appears in 7.

Similarly to the soft case we can expand the phase-space measure and the  $2 \rightarrow N + 1$  for small values of  $\theta_{gi}$  and find that they factorize into a finite Born-level term and a divergent piece.

If we define the parton density function (PDF) for incoming partons  $A$  and  $B$  through

$$d\sigma_{p+B \rightarrow N+1} = f_A(x) dx d\sigma_{A+B \rightarrow N+1} \quad (3.21)$$

where  $f(x)dx$  is the probability of getting parton  $A$  from the proton, carrying a momentum fraction between  $x$  and  $x + dx$ , we can write the factorized cross-section as

$$d\sigma_{p+B \rightarrow N+1} = f_A\left(\frac{x}{z}\right) \left[ \frac{\alpha_s}{2\pi} \frac{\Gamma[1-\epsilon]}{\Gamma[1-2\epsilon]} \left(\frac{4\pi\mu^2}{s}\right)^\epsilon \right] \sigma_{A+B \rightarrow N} \left(-\frac{1}{\epsilon}\right) \delta_c^{-\epsilon} P_{A'A}(z, \epsilon) \frac{dz}{z} \left[\frac{1-z}{z}\right]^{-\epsilon} dx, \quad (3.22)$$

where  $P_{A'A}$  denotes the Altarelli-Parisi kernel [46], describing the probability of parton  $A$  emitting a collinear gluon and continuing as parton  $A'$ . We ignore the initial state parton  $B$  for notational convenience for now.

The collinear divergencies in the splitting functions can be absorbed into the renormalization of the PDFs of the incoming partons. We do that in the  $\overline{\text{MS}}$  scheme, with the renormalization scale  $\mu_R$ .

The soft and collinear contributions are combined with the virtual corrections to arrive at

$$d\sigma = \sum_{i,j} \int dx_1 dx_2 \left\{ [f_i(x_1, \mu_F) f_j(x_2, \mu_F) + (1 \leftrightarrow 2)] [d\hat{\sigma}_{ij}^{(0)}(\hat{s}) + d\hat{\sigma}_{ij}^{(1)}(\hat{s}; \delta_s)] \right. \\ \left. + [\tilde{f}_i(x_1, \mu_F) f_j(x_2, \mu_F) + \tilde{f}_j(x_1, \mu_F) f_i(x_2, \mu_F) + (1 \leftrightarrow 2)] d\hat{\sigma}_{ij}^{(0)}(\hat{s}) \right\} \quad (3.23)$$

with

$$\tilde{f}_i(x, \mu_F) = \sum_k \int_x^{1-\delta_s} \frac{dz}{z} f_k\left(\frac{x}{z}, \mu_F\right) \frac{\alpha_s}{2\pi} \left[ P_{ik}(z) \ln\left(\frac{\hat{s}}{\mu_F^2} \frac{1-z}{z} \delta_c\right) - P'_{ik}(z) \right]. \quad (3.24)$$

Here  $f_i(x, \mu_F)$  is the proton PDF for the parton  $i$  with the factorization scale  $\mu_F$ ;  $d\hat{\sigma}_{ij}^{(0)}$  is the differential partonic Born cross-section for the incoming partons  $i$  and  $j$ ;  $d\hat{\sigma}_{ij}^{(1)}$  is the one-loop corrected partonic cross-section including the soft radiation terms;  $P_{ik}(z)$  and  $P'_{ik}(z)$  are the finite and  $\mathcal{O}(\epsilon)$  pieces of the unregulated splitting kernels (see e.g. Refs. [44]), and  $\hat{s} = x_1 x_2 s$ . Note that the form of eq. 3.23 changes slightly for the quark-gluon induced subprocesses, which do not receive Born contributions.

The remaining hard radiation region, labeled ‘‘H’’, is constrained by the conditions  $\delta_s \frac{\sqrt{\hat{s}}}{2} < E_g$  and  $1 - \cos\theta_{gi} > \delta_c \frac{\sqrt{\hat{s}}}{E_g}$ . It is finite and can be computed with numerical Monte-Carlo integration methods. Both the hard contribution and the result in eq. 3.23 separately depend on the choices for  $\delta_s$  and  $\delta_c$ . However, as long as the cutoff parameters are kept sufficiently small, this dependence drops out in the combined total result.

### 3.1.3 Notes on the Technical Implementation

The way the Coloron model has been implemented makes it necessary to decide on a scheme in which to treat  $\gamma_5$  in dimensional regularization, even though the model is not chiral in nature. Naïvely one expects  $\gamma_5$  to anticommute with all other Dirac matrices which is in practice insufficient to unambiguously define traces that contain odd numbers of  $\gamma_5$ . We therefore need to pick an additional prescription to ensure that e.g.:

$$\text{Tr} [\gamma_5 \gamma^\mu \gamma^\nu \gamma^\rho \gamma^\sigma] = 4i \varepsilon^{\mu\nu\rho\sigma} \quad (3.25)$$

One possibility is the so-called Breitenlohner-Maison scheme [47] which assumes the anticommutator  $\{\gamma_5, \gamma^\mu\}$  to be non-vanishing in  $D = 4 - 2\epsilon$  dimensions, corresponding to a term proportional to  $\epsilon$  in the Lagrangian that explicitly breaks chiral symmetry. Alternatively one can choose the Larin scheme [48] in which  $\gamma_5$  remains anticommuting and chiral symmetry is conserved but one is required to treat the non-conservation of the chiral current (Adler-Bardeen-Jackiw anomaly) separately. Both schemes lead to identical results in the context of this and the following chapters, for technical reasons we utilized the "\$LARIN" option implemented in FEYNALC.

The calculation has been performed using several publicly available computing tools, but additional components were specifically implemented by the authors. The Feynman rules of the Coloron model (see Appendix A.2) have been incorporated into FEYNARTS 3 [49], which was used for generating the relevant diagrams and amplitudes. The color, Dirac and Lorentz algebra was performed with FEYNALC [50].

To simplify the treatment of tensor loop integrals, the one-loop amplitude was contracted with the Born amplitude and the sum over the spins of external particles carried out before any tensor reduction. As a result, most tensor structures in the numerator of the loop integrand can be canceled against propagator denominators. For the remaining tensor integrals, Passarino-Veltman reduction has been used [51]. One thus arrives at a final result in terms of standard one-loop basis functions. The IR-finite basis integrals have been evaluated numerically using LOOPTOOLS 2 [52], whereas the IR-divergent basis integrals were taken from Ref. [53], and are listed in Appendix B.1.

For the  $q\bar{q}$  channel, two fully independent calculations have been carried out. One is based on dimensional regularization for the UV singularities and gluon and quark mass regulators for the soft and collinear divergencies, respectively. The other calculation has employed dimensional regularization for all types of singularities. Perfect agreement between the two results at the level of differential cross-sections was obtained. For the  $gg$  channel, the use of a mass regulator is not suitable. Nevertheless, we have performed many independent checks of partial contributions to the final result.

The numerical integration over the final-state phase space and initial-state PDFs is implemented in the form of a Monte-Carlo generator in Fortran. This implementation is based on Ref. [54] and produces weighted parton-level events.

### 3.2 NUMERICAL RESULTS

In the following, we present phenomenological results for Coloron pair production at the LHC with  $\sqrt{s} = 14$  TeV. Throughout this section, the CTEQ6.1M PDF set [55] have been used, as incorporated in the LHAPDF framework [56].

As a first consistency check, the independence of the total NLO cross-section on the soft and collinear slicing cut-offs,  $\delta_s$  and  $\delta_c$  is shown in Fig. 9. The figure depicts two separate plots for the dependence on  $\delta_s$  and  $\delta_c$ , respectively. It can be seen that the combined virtual, soft and collinear contributions ( $\sigma_{S+V}$ ) and the hard real emission contribution ( $\sigma_{2\rightarrow 3}$ ) are separately logarithmically dependent on  $\delta_s$  and  $\delta_c$ , but this dependence cancels in the sum  $\sigma_{\text{NLO}} = \sigma_{S+V} + \sigma_{2\rightarrow 3}$ . The remaining power contributions, proportional to  $\delta_s^n$  and  $\delta_c^n$ , are negligibly small for all practical purposes if the cut-off parameters are smaller than about  $10^{-3}$  and  $10^{-4}$ , respectively. Note that the plots in Fig. 9 are subject to statistical errors from the Monte-Carlo integration over initial parton momentum fractions and final-state phase space. However, the cancellation of soft and collinear logarithms happens already point-by-point for the fully differential cross-section, after integration over only the one-particle phase-space of the massless final-state parton in  $\sigma_{2\rightarrow 3}$ . Therefore, the accuracy of the cancellation of the  $\delta_s$  and  $\delta_c$  dependence is very high, as shown in the lower boxes of the Fig. 9.

The optimal choice of the cut-off parameters needs to strike a balance between two constraints: (i) The non-logarithmic power contributions, proportional to  $\delta_{s,c}^n$ , are minimized by choosing each cut-off parameter as small as possible, whereas (ii) the statistical error for the  $2 \rightarrow 3$  phase-space integration increases if  $\delta_{s,c}$  are too small. For the remainder of this section, we use  $\delta_s = 5 \times 10^{-4}$  and  $\delta_c = 5 \times 10^{-5}$ .

In Fig. 10, the LO and NLO total cross-sections are shown as a function of the Coloron mass  $M$ . For this plot, the mass of the  $\mathcal{P}$ -odd quarks has been fixed according to the mUED prediction, i.e.  $M_\Psi = M - \Delta M$ , where  $\Delta M$  is the mass splitting due to boundary terms in mUED [39]. To show the qualitative behavior we restrict ourselves to employ the leading logarithm of the mass splitting, the full one-loop result can be found in 5.1.2

$$\Delta M = M \frac{11\alpha_s}{16\pi} \ln \frac{\Lambda^2}{\mu^2} \quad (3.26)$$

Since  $\Delta M$  is a one-loop contribution itself, we neglect it inside the  $\mathcal{O}(\alpha_s)$  corrections to the cross-section and set  $M_\Psi = M$  there. For the UV cut-off of mUED we choose  $\Lambda = 20 M$ .

In the lower part of the figure, the  $K$ -factor  $\sigma_{\text{NLO}}/\sigma_{\text{LO}}$  of the NLO and Born cross-sections is shown. As evident from this plot, the  $K$ -factor depends only mildly on  $M$  and amounts to about 0.88. It is interesting to note that the NLO contributions are negative in all three subprocesses,  $q\bar{q} \rightarrow CC + X$ ,  $gg \rightarrow CC + X$ , and  $qg/\bar{q}g \rightarrow CC + X$ , the latter of which is only generated by  $2 \rightarrow 3$  real emission diagrams and is turned negative due to the PDF renormalization. While the overall correction is relatively modest, and of a typical magnitude for high-energy QCD processes, it is nevertheless relevant for accurately evaluating current limits and the discovery potential of the LHC for mUED and related models [23].

In addition, the computation of the NLO QCD corrections serves to reduce the theoretical uncertainty from the renormalization and factorization scale dependence. This is demonstrated in Fig. 11, where the two scales have been varied in parallel,  $\mu = \mu_F$ . Considering the range  $0.75 < \mu/M < 1.5$ , the LO cross-section changes by about  $\begin{smallmatrix} +15\% \\ -17\% \end{smallmatrix}$ , which is reduced to  $\begin{smallmatrix} +5\% \\ -8\% \end{smallmatrix}$  for the NLO cross-section. Note that the dominant source of uncertainty stems from the renormalization scale, whereas the factorization scale by itself has a subdominant effect. In Fig. 12, we also show how the cross-section changes when the mass splitting  $\Delta M = M - M_\Psi$  is modified from the mUED prediction. Note that the  $gg$  channel does not depend on

this parameter at tree-level, and we neglect the mass splitting within the one-loop corrections. Therefore, only the  $q\bar{q}$  channel is shown in Fig. 12.

We restrict ourselves to the mass ordering  $M_\Psi < M$ , to avoid the situation where the heavy quarks may become resonant in the subprocess  $qg \rightarrow CCq$ , i.e.  $qg \rightarrow C\Psi$  production with the subsequent decay  $\Psi \rightarrow Cq$ . This would correspond to a different process than the one studied in this chapter and is left for future work.

As evident from Fig. 12, the  $q\bar{q} \rightarrow CC$  subprocess depends very sensitively on  $\Delta M$ . However, since the  $gg$  channel is dominant, the total cross-section varies only by a few percent for reasonable values of the mass splitting.

Finally, Fig. 13 displays the impact of the NLO corrections on the differential cross-section in terms of the rapidity  $y \equiv \frac{1}{2} \ln \frac{E+p_L}{E-p_L}$ . Here  $E$  and  $p_L$  are the energy and longitudinal momentum of one of the final-state Colorons. Since, after summing over colors, we have two identical Colorons in the final state, the rapidity distribution is symmetric. As one can see from the figure, the effect of the NLO corrections results in a slight enhancement of the tails of the rapidity distribution relative to the central region. This can be partially understood from a simple kinematic effect, since the recoil against extra radiated partons causes a broadening of the rapidity distribution.

### 3.3 SUMMARY AND CONCLUSIONS

The production of colored new physics particles at the LHC may be subject to sizeable QCD corrections. In this article, results for the NLO corrections to the pair production of color-octet vector bosons have been presented. Such new vector bosons appear, for example, in Coloron models or models with extra space dimensions. There are characteristic versions of these models where the single production of color-octet vector bosons is forbidden by a parity symmetry, such as an exchange symmetry for Coloron models and Kaluza-Klein parity for extra dimensional models. For concreteness, this chapter focuses on a two-site Coloron model, which is based on two copies of a non-linear sigma model for the gauge sector. In addition, the presence of the exchange symmetry requires the introduction of heavy partners

to the SM quarks. This model can serve as a gauge-invariant low-energy effective description of the minimal universal extra dimension (mUED) model.

The renormalization of the two-site Coloron model involves several peculiarities that do not occur for models with colored particles of spin less than one. For instance, the couplings of the SM gluon and the massive Coloron are identical at tree-level, but they receive different counterterms at higher orders. In addition, the broken gauge symmetry of the massive vector boson requires the introduction of a counterterm for the symmetry-breaking vacuum expectation value. This may be surprising at first glance, given that the symmetry-breaking mechanism is not specified in the non-linear sigma model, but in fact this counterterm can be uniquely determined from the Goldstone self-energy.

The calculation of the NLO corrections presented in this chapter is based on a largely automated computer implementation, using publicly available packages supplemented by in-house routines. For the combination of virtual loop corrections and real radiation contributions, the phase-space slicing method has been employed. Several checks of the results have been performed.

It is found that for the standard choice of the renormalization scale,  $\mu = M$ , where  $M$  is the Coloron mass, the NLO correction has a relatively modest impact on the Coloron pair production cross-section. The total NLO cross-section is 11–14% smaller than the LO result for values of  $M$  between 1 and 2 TeV. At the same time, the dependence of the cross-section on the renormalization scale is significantly reduced, by a factor of 2–3. By studying the rapidity distribution it is furthermore observed that the NLO contribution cannot be characterized by a simple global K-factor, but instead the K-factor is slightly smaller in the central rapidity region and slightly larger for large absolute values of rapidity.

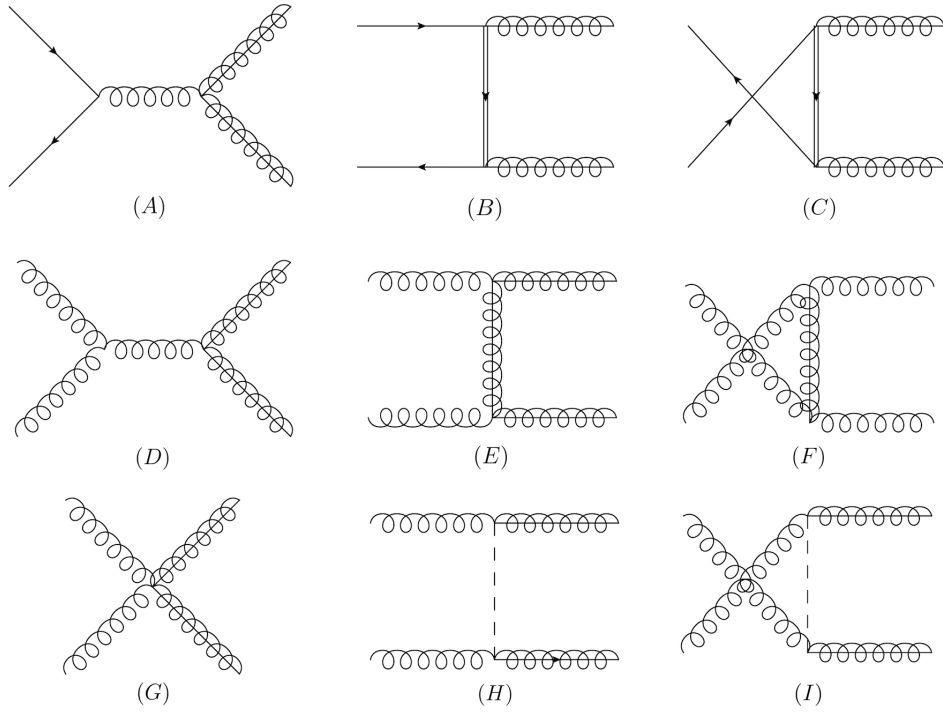


Figure 4: Born-level diagrams contributing to massive color-octet vector-boson pair production. Here the spring–solid lines indicate massive color-octet vector-bosons, while the double lines indicate massive  $\mathcal{P}$ -odd quarks, and the dashed line indicates a  $\mathcal{P}$ -odd Goldstone scalar.

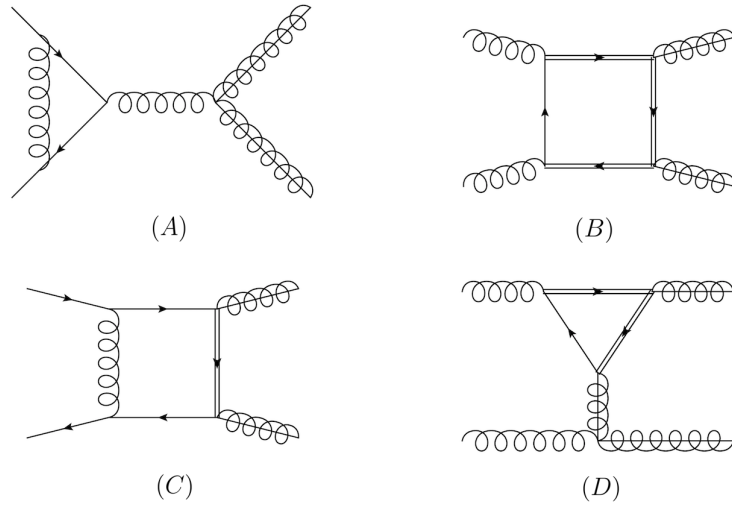


Figure 5: Sample one-loop diagrams contributing to Coloron pair production. See Fig. 4 for the definition of the different propagator line types.

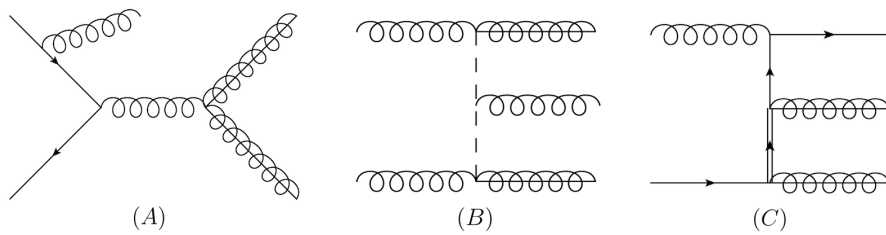


Figure 6: Sample real radiation diagrams contributing to Coloron pair production. See Fig. 4 for the definition of the different propagator line types.

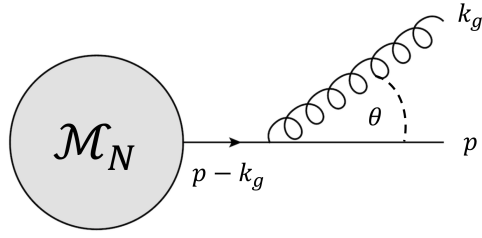


Figure 7: *Real Emission of a soft/collinear gluon from a final state quark. The momentum square  $(p - k_g)^2 = -2E_p E_g(1 - \cos \theta)$  in the denominator of the propagator goes to zero for either  $E_g \rightarrow 0$  or  $\cos \theta \rightarrow 1$ .*

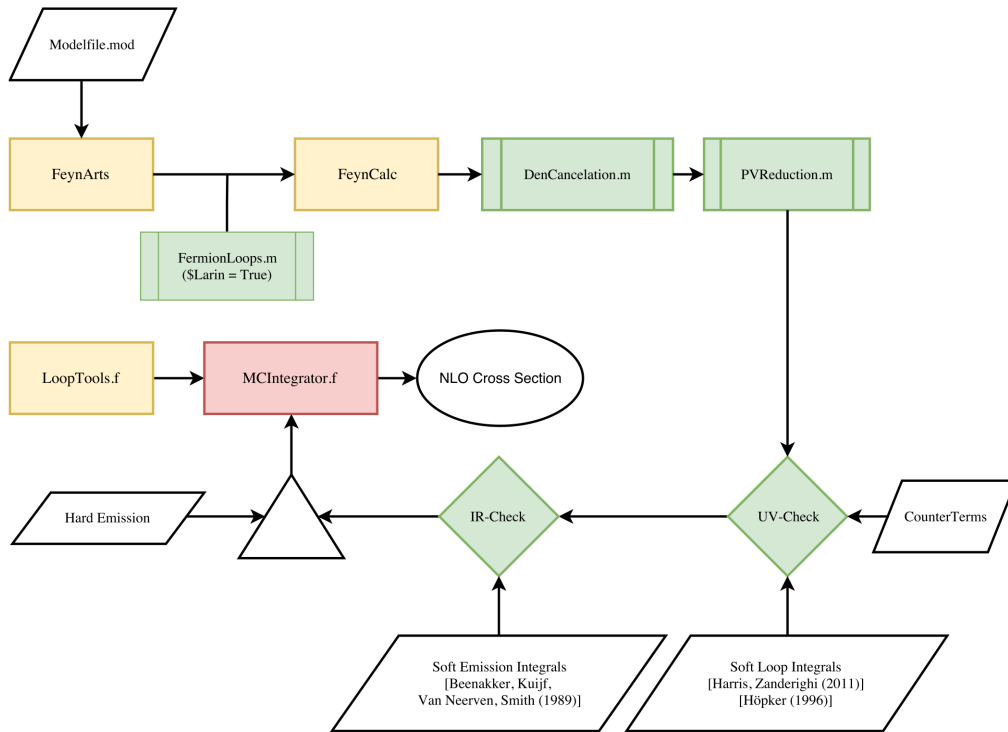


Figure 8: *Flowchart illustrating the additions made to the FEYNCalc/FEYNArts framework. Yellow routines represent publicly available packages, while green are direct amends to that code. White parallelograms represent external input and the red integrator is a set of separate FORTRAN routines.*

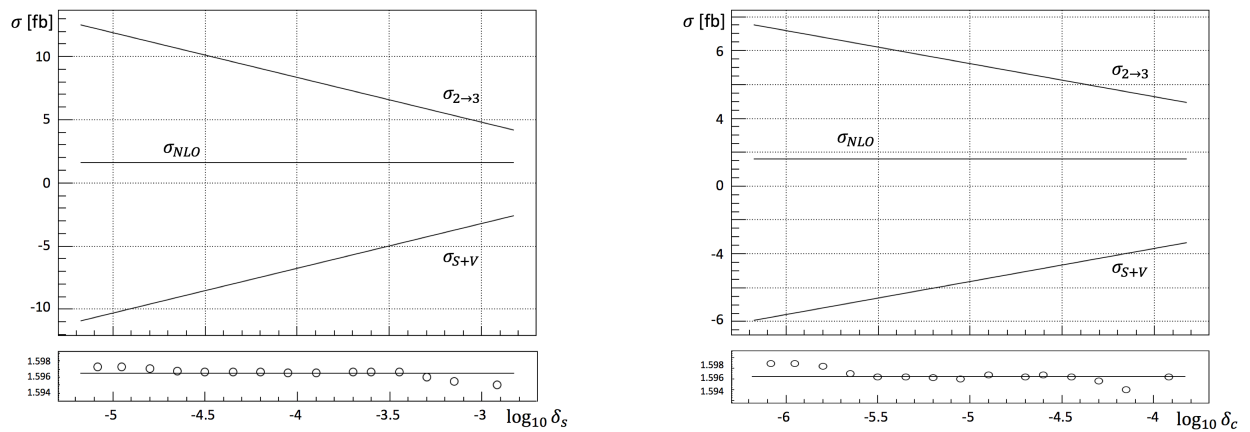


Figure 9: *Dependence of the NLO cross-section for the  $pp \rightarrow CC$  on the soft cut-off  $\delta_s$  (left) and the collinear cut-off  $\delta_c$  (right). Both plots are for a  $pp$  center-of-mass energy of  $\sqrt{s} = 14$  TeV, Coloron mass  $M = 1$  TeV, and renormalization and factorization scales  $\mu = \mu_F = M$ . Furthermore, in the left (right) panel, the fixed value  $\delta_c = 10^{-5}$  ( $\delta_s = 10^{-3.5}$ ) has been used.*

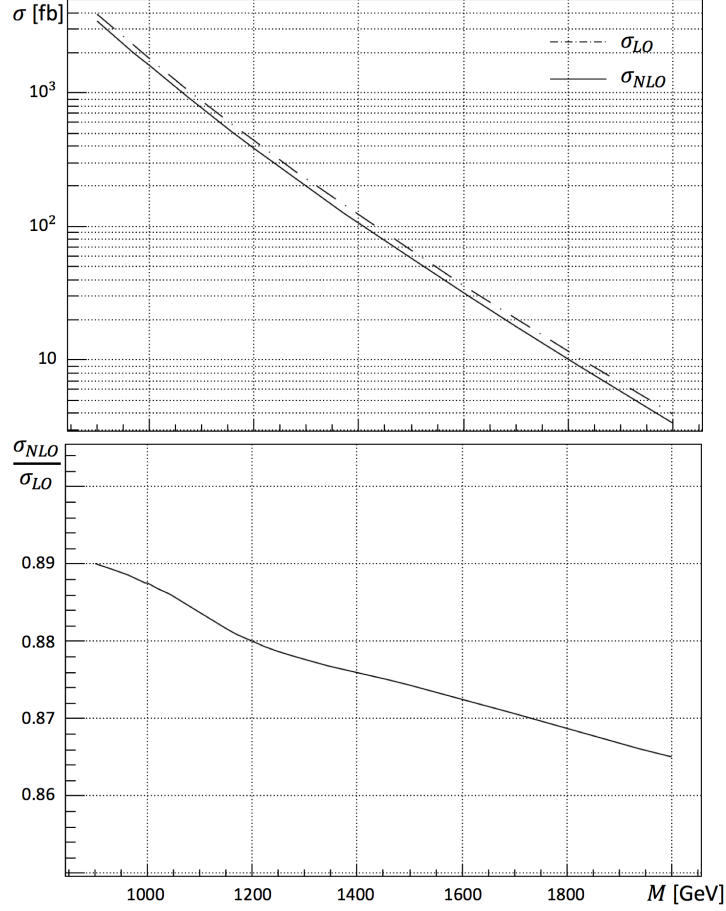


Figure 10: *Total LO and NLO Coloron pair production cross-sections as function of the Coloron mass  $M$ , for  $\sqrt{s} = 14$  TeV and  $\mu = \mu_F = M$ . The mass splitting between the Colorons and  $\mathcal{P}$ -odd quarks in the Born contribution has been set to the value predicted by  $mUED$ , see text and eq. (3.26), while the splitting has been neglected in the NLO corrections. The lower panel shows the ratio between NLO and LO cross-sections.*

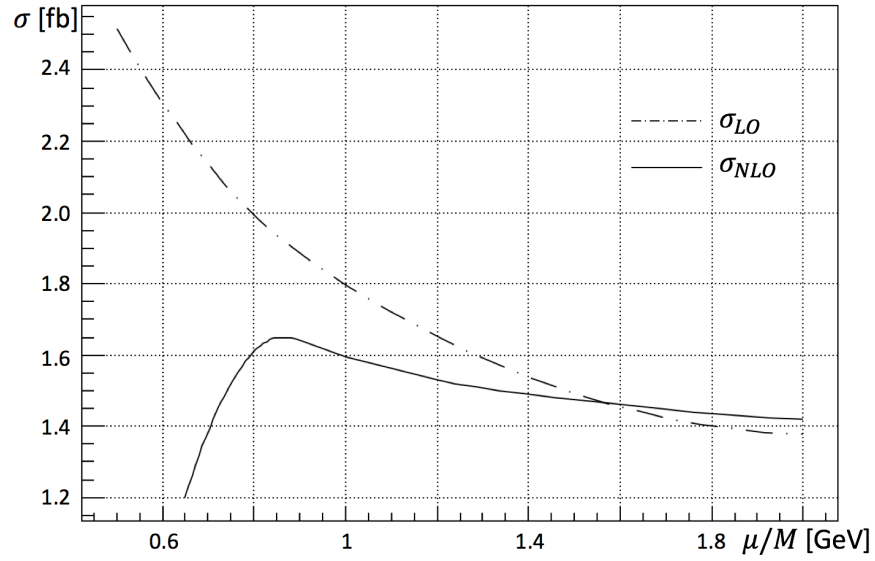


Figure 11: *Dependence of the total LO and NLO Coloron pair production cross-sections on the combined renormalization and factorization scale  $\mu = \mu_F$ . The plot is based on the  $pp$  center-of-mass energy  $\sqrt{s} = 14$  TeV, mass  $M = 1$  TeV, and mass splitting  $M - M_\Psi$  in the Born contribution as predicted by mUED, see text and eq. (3.26).*

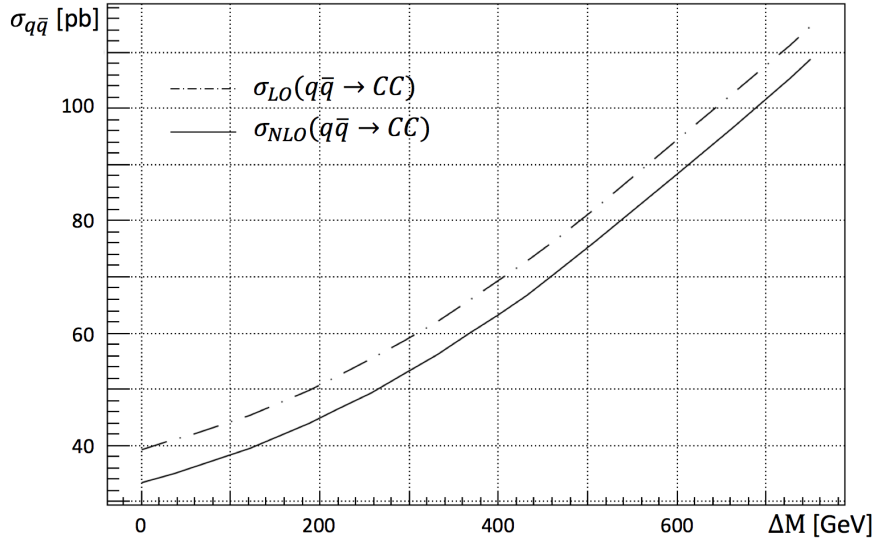


Figure 12: Total LO and NLO Coloron pair production cross-sections as function of quark-Coloron mass splitting  $\Delta M = M - M_\Psi$ . The other input parameters have been set to  $\sqrt{s} = 14$  TeV, mass  $M = 1$  TeV, and  $\mu = \mu_F = M$ .

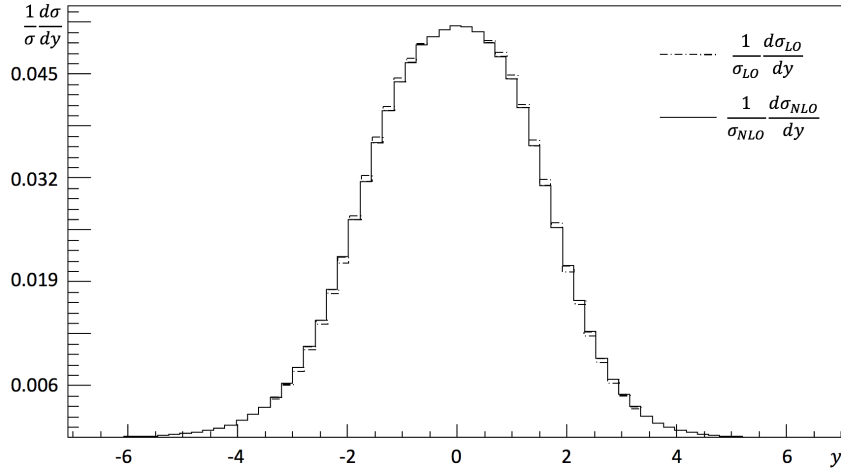


Figure 13: Differential cross-section for Coloron pair production in terms of rapidity at LO and NLO accuracy, for  $\sqrt{s} = 14$  TeV, mass  $M = 1$  TeV, and  $\mu = \mu_F = M$ .

## 4.0 THRESHOLD BEHAVIOR OF VERTEX FUNCTIONS

While the question of scale sensitivity of couplings in extra-dimensional theories has a long history [58–63], a detailed analysis of the *difference* between the effective zero-mode gauge bosons and their KK excitations is so far missing. Such an analysis is the topic of this chapter, together with an extensive discussion of the influence of the UV cutoff scale on both vertices.

The calculation in the previous section was performed in a model which truncates the KK-tower for all modes heavier than  $n = 1$ . If this represents a valid approximation is the subject of investigation in this chapter, based on Ref. [64]. Furthermore it is important to discuss and quantify how big the uncertainty is that is being introduced into the calculation by truncating after a certain mode number. To this end we evaluate the Wilson coefficients stemming from increasingly heavier KK-modes in the loop for the three SM QCD-operators as well as the a vertex with two KK level-1 modes and a SM mode.

The  $q_0 - Q_1 - G_1$  vertex receives infrared divergent contributions from diagrams containing SM modes. We calculate the full one-loop decay width  $\Gamma[G_1 \rightarrow q_0 Q_1]$  through two cutoff phase space slicing to fix the IR physics. Considering the decay width instead of the naked Wilson coefficient is not only helping us to put our results in perspective by considering a physical observable, but also technically necessary, since the IR divergence appears in three as well as four-point operators, prohibiting to us to define a universal Wilson coefficient.

The modes  $n \geq 2$  can be included straightforwardly. For every new level participating in the loop we renormalize the vertex and report the change of the beta function, as well as the resulting Wilson coefficient. We then extract the asymptotic behavior from the summed up vertex functions and compare them. In a final step we analyze the behavior of the vertex functions by perturbatively solving the exact Functional Renormalization Group Equation

(FRGE).

#### 4.1 INFRARED DIVERGENT CONTRIBUTIONS

Completely analogous to the procedure employed in chapter 3 we calculate the decay width for the process  $G_1 \rightarrow q_0 Q_1$  (we obtain the same result for the decay into doublet quarks as for singlets, since we are considering QCD corrections only).

Diagram (A) in Fig. 14 represents the only tree-level Feynman describing the Coloron decay. Calculating the squared matrix element necessary for the decay width we find

$$|\mathcal{M}_{\text{Born}}|^2 = \frac{g^2}{16M_{G_1}^2} N_C C_F (M_{G_1}^2 - M_{Q_1}^2) (2M_{G_1}^2 + M_{Q_1}^2), \quad (4.1)$$

which vanishes if the Coloron and KK-Quark masses are identical on kinematic grounds. We therefore assume again a radiatively induced mass splitting as we did in section 3.2. Since the mass splitting is small in comparison to the mass scale of the process we will perform the calculation of the NLO corrected matrix element only to lowest order in  $M_{G_1}^2 - M_{Q_1}^2$ . The decay width for the two-body processes can be derived from the corresponding matrix elements via

$$\Gamma_2(G_1 \rightarrow q_0 \bar{Q}_1) = \frac{M_{G_1}^2 - M_{Q_1}^2}{16\pi M_{G_1}^3} |\mathcal{M}_2|^2. \quad (4.2)$$

The renormalization (example loop diagram (B) in Fig. 14) is performed in the same way we described in section 3.1.1, with the exception that we also need a field renormalization  $\delta Z_{L,R}^Q$  for the external KK-quark leg, which can be defined in the on-shell scheme through

$$\delta Z_{L,R}^Q = -\Re \left\{ \Sigma_{L,R}^Q(M_{Q_1}^2) \right\} - M_{Q_1}^2 \frac{\partial}{\partial p^2} \Re \left\{ \Sigma_R^Q(p^2) + \Sigma_L^Q(p^2) + 2\Sigma_S^Q(p^2) \right\} \Big|_{p^2=M_{Q_1}^2}. \quad (4.3)$$

Furthermore we require the vertex renormalization constant defined in the  $\overline{\text{MS}}$  scheme  $\delta Z'_g$  from eq. (3.9). Also note that for our analysis we assume all quarks to be massless, including the top, such that  $n_q = 6$ .

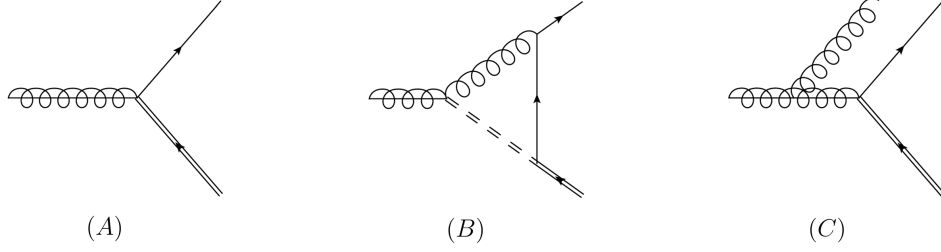


Figure 14: *Sample diagrams the decay of the level-1 gluon decay  $G_0 \rightarrow q_0 \bar{Q}_0$  within the Coloron model. (A) Born-level decay (B) NLO correction to the Born vertex (C) real emission contribution with an infrared divergence.*

To remove the infrared divergencies we employ phase-space slicing with two cutoffs in the way described in section 3.1.2. The soft divergencies from the real emission diagrams, (C) in Fig. 14 exactly cancel the soft poles of the one-loop functions. Collinear divergencies only arise from the diagram containing the final state gluon being emitted from the SM quark leg. That case is described by the same Altarelli-Parisi splitting kernel we found for the initial state radiation in eq. (3.22).

The three-body phase space integration in the hard, non-collinear regime can be performed analytically. The phase space measure for that case reads

$$d\Gamma_3 = \frac{M_{G_1}^2 - M_{Q_1}^2 - 2E_3 M_{G_1}}{2(M_{G_1} - E_3(1 - \cos\theta))} \frac{dE_3 d(\cos\theta)}{64\pi^3 M_{G_1}} |\mathcal{M}_3|^2 \quad (4.4)$$

and is dependent on the energy of the final state gluon  $E_3$  and the angle  $\theta$  between the gluon and the SM quark. The integration range of these two variables is restricted by the soft and collinear conditions expressed through

$$\begin{aligned} -1 \leq \cos\theta \leq 1 - \frac{M_{G_1}^3}{E_3(M_{G_1}^2 - 2M_{G_1}E_3 - M_{Q_1}^2)} \delta_c, \\ \frac{M_{G_1}}{2} \delta_s \leq E_3 \leq \frac{M_{G_1}^2 - M_{Q_1}^2}{2M_{G_1}}. \end{aligned} \quad (4.5)$$

After carrying out the integration over the three-body matrix element the cancelation of cutoff parameters between the three and two-body processes is then checked explicitly. Due

to the approximation in which we work the  $\kappa$ -factor is a constant, independent of any of the masses, and turns out to be  $\kappa = 1.238$ . In Fig. 15 we plot the dependence of the LO and NLO decay width on the cutoff scale  $\Lambda$ , that was introduced through the radiative mass splitting between the KK-quark and gluon.

## 4.2 CONTRIBUTIONS FROM HIGHER MODES

In order to calculate the contributions from modes with  $n \geq 2$  to the previously described process, we need to renormalize the vertex at any order  $n$ , that consists of modes containing but not exceeding  $n$ . After introducing a counterterm that is dependent on renormalization constants for the external legs with level- $n$  modes in the loop we absorb the rest of the UV divergence into a coupling renormalization of form

$$\delta Z_g = -\frac{g_s^2}{32\pi^2}\beta_x, \quad (4.6)$$

from which we then can extract the contribution  $\beta_n$  of the level to the overall beta function

$$\frac{\partial\alpha^{-1}}{\partial\log\mu} = -\frac{1}{\alpha^2}\frac{\partial\alpha}{\partial\log\mu} = \frac{\beta_x}{2\pi}. \quad (4.7)$$

### 4.2.1 Standard Model Vertices

The three QCD tree-level vertices, the quark-gluon vertex as well as the pure Yang-Mills vertices, within the Standard Model receive contributions from higher KK-modes running in the loop (an example diagram for each is shown in Fig. 16). All modes within in the loop have the same mode-number starting at  $n = 0$ , as a consequence of KK-parity.

The standard result for the QCD beta function is reproduced by the zero modes at one loop and found to be

$$\beta_{\text{SM}} = \left( \frac{11}{3}C_A - \frac{4}{3}n_q T_f \right). \quad (4.8)$$

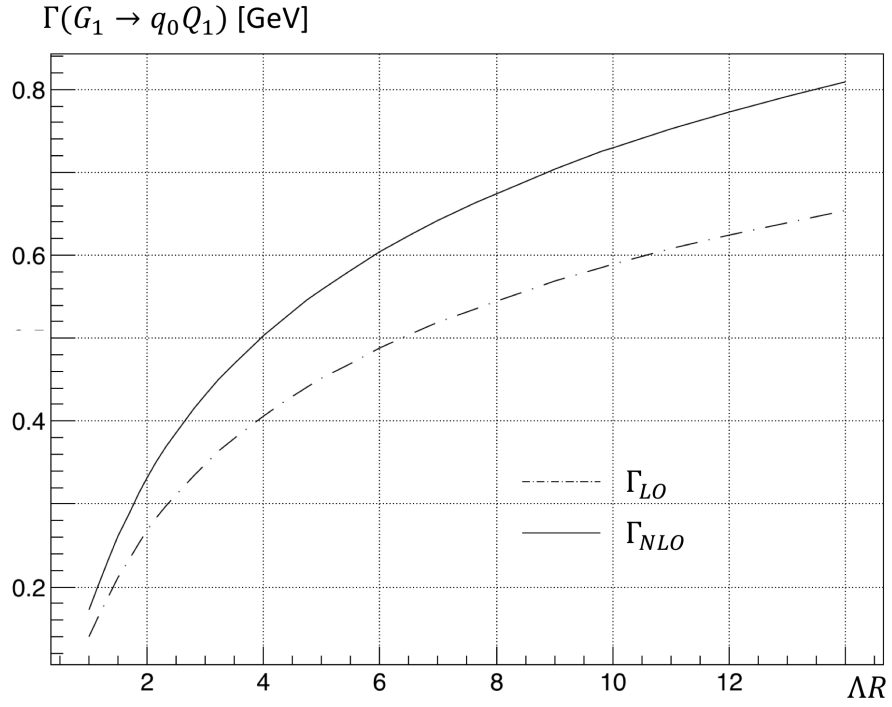


Figure 15: Full LO and NLO decay width for the level-1 KK-gluon decaying into a regular quark and the level-1 KK-quark within the Coloron model. Both curves exhibit the same  $\Lambda$  dependence, since the  $\kappa$ -factor is constant in our approximation.

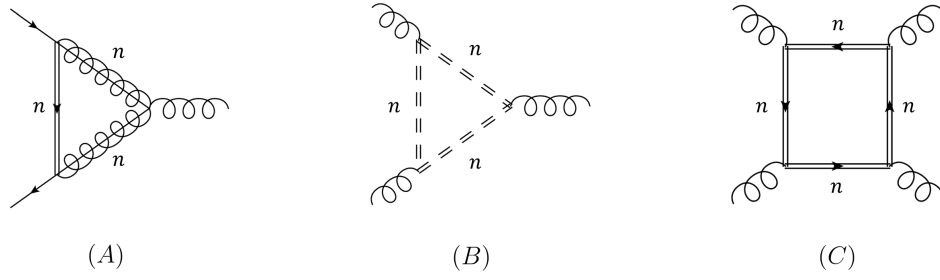


Figure 16: *Sample diagrams for the KK-contributions to the SM vertices. (A) quark-gluon vertex (B) three-point gluon vertex (C) four-point gluon vertex.*

Now when allowing for KK-modes with  $n \geq 1$  in the loop, we acquire an additional contribution to the beta function every time we cross the energy threshold  $\frac{n}{R}$

$$\beta_N = \left( \frac{7}{2}C_A - \frac{8}{3}n_q T_f \right). \quad (4.9)$$

These contributions to the beta function lead to a running of the strong coupling constant that deviates from the Standard Model behavior, described for a renormalization scale between  $\Lambda \leq \mu \leq \Lambda + R^{-1}$  by

$$\begin{aligned} \alpha_S^{-1}(\mu) &= \alpha_S^{-1}(M_Z) + \frac{\beta_{\text{SM}}}{2\pi} \log\left(\frac{\mu}{M_Z}\right) + \frac{\beta_N}{2\pi} \sum_{n=1}^{\Lambda R} \log\left(\frac{\mu}{nR^{-1}}\right) \\ &= \alpha_S^{-1}(M_Z) + \frac{\beta_{\text{SM}}}{2\pi} \log\left(\frac{\mu}{M_Z}\right) + \frac{\beta_N}{2\pi} \left[ \Lambda R \log\left(\frac{\mu}{R^{-1}}\right) - \log(\Lambda R!) \right], \end{aligned} \quad (4.10)$$

where the sum over KK-modes extends up to a UV-cutoff scale  $\Lambda$ .

It has to be noted that the sum is strictly speaking only defined for an integer cutoff number. We therefore write  $\Lambda R$ , as it appears in and from the summation, to be understood as the argument of the Gauss floor function  $[\Lambda R]$ , rounding down to the largest integer not exceeding  $\Lambda R$ .

Since we take all external legs to be massless there is no dipole operator being generated in the Lagrangian. We find that the vector coupling  $q_0 - q_0 - G_0$  as well as the three and

four-point gluon couplings receive the same Wilson coefficient  $C_{\text{SM}}$ . Summing over all modes within the loop up to the cutoff-scale that coefficient then reads

$$C_{\text{SM}}(\mu) = \frac{g_s^3}{192\pi^2} \sum_{n=1}^{\Lambda R} \left[ 2C_A - (21C_A - 16n_q T_f) \log \left( \frac{n^2}{(\mu R)^2} \right) \right]. \quad (4.11)$$

Notice that the first term in the bracket is independent of the Renormalization Group running and represents a threshold correction.

### 4.2.2 KK-Vertices

In the case of two external legs being KK-particles the one-loop corrections to the vertex induce a dipole operator and the total interaction under consideration becomes

$$-iC_{q_0 Q_1 G_1} \gamma^\mu P_L - D_{q_0 Q_1 G_1} \frac{\sigma^{\mu\nu}}{2R^{-1}} q_\nu P_L. \quad (4.12)$$

If only Standard Model modes and the first KK-mode are allowed in the loop, the coupling renormalization of eq. (3.9) contributes to the beta function with

$$\beta_{\text{Coloron}} = \left( \frac{(3 + 85C_A^2)(C_A - 2C_F)}{12} - \frac{8}{3}n_q T_f \right). \quad (4.13)$$

The contributions to the vertex function from higher modes are shown in Fig. 17 and can be straightforwardly calculated for every new mode allowed in the loop. The renormalization procedure is again done level by level and require the on-shell field renormalizations for external legs.

The beta function resulting from the coupling renormalization at every level  $n \geq 2$  is identical to the one we found for the SM vertices for  $n \geq 1$ , reported in eq. (4.9).

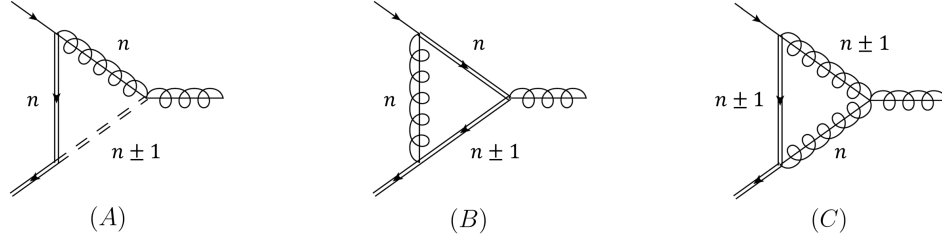


Figure 17: Sample diagrams for the KK-contributions to the vertex with two level-1 modes as external legs.

For the Wilson coefficients appearing in front of the vector coupling of eq. (4.12) we separate the NLO contribution into terms proportional to  $C_A, C_F$  and  $n_q$  and find

$$C_{\text{KK},1}(\mu) = -\frac{g_s^3}{64\pi^2} C_F \sum_{n=1}^{\Lambda R} \left[ 10 + (1 + 5n) \log \left( \frac{n^2}{(n+1)^2} \right) \right], \quad (4.14)$$

$$\begin{aligned} C_{\text{KK},2}(\mu) &= \\ &= \frac{g_s^3}{64\pi^2} C_A \sum_{n=1}^{\Lambda R} \left[ 15 + 4n + 4n^2 + n(8 + 3n + 2n^2) \log \left( \frac{n^2}{(n+1)^2} \right) - 7 \log \left( \frac{(n+1)^2}{(\mu R)^2} \right) \right], \end{aligned}$$

$$\begin{aligned} C_{\text{KK},3}(\mu) &= \\ &= -\frac{g_s^3}{12\pi^2} n_q T_f \sum_{n=1}^{\Lambda R} \left[ \frac{13}{6} + 2n + 2n^2 + \frac{n}{2} (3 + 3n + 2n^2) \log \left( \frac{n^2}{(n+1)^2} \right) - \log \left( \frac{(n+1)^2}{(\mu R)^2} \right) \right]. \end{aligned}$$

Additionally we can calculate the dipole coefficient, which is finite and does not require renormalization

$$D_{q_0 G_1 Q_1} = \frac{g_s^2}{64\pi^2} (C_A^2 - 4) (C_A - 2C_F) \sum_{n=1}^{\Lambda R} \left[ 2 + \frac{1+2n}{2} \log \left( \frac{n^2}{(n+1)^2} \right) \right]. \quad (4.15)$$

### 4.2.3 Asymptotic Expansion

The analytic summation using elliptical Jacobi theta functions, that has been employed in Ref. [58, 59], is not an accurate method for our case, since we are defining our coupling renormalization within the  $\overline{\text{MS}}$  scheme. We are however able to recover the same results in the large  $\Lambda R$  limit, as the theta function method does within the on-shell scheme, using a somewhat different approach.

We begin by performing the summation up to mode  $N = \lfloor \Lambda R \rfloor$  analytically. The only non-trivial sums appearing are of the form

$$\sum_{n=1}^N \log \left( \frac{n}{n+1} \right) = \log \left( \frac{\Gamma[N+1]}{\Gamma[N+2]} \right), \quad (4.16)$$

which can be rewritten using the Euler  $\Gamma$  function as a generalization of the factorial, and

$$\sum_{n=1}^N n \log \left( \frac{n}{n+1} \right) = \log(\Gamma[N+2]) + \zeta'[-1, N+1] - \zeta'[-1, N+2], \quad (4.17)$$

which can be carried out using the Riemann  $\zeta$  function. The prime denotes a derivative with respect to the first argument of the generalized  $\zeta$  function  $\zeta[s, a] = \sum_{n=0}^{\infty} (n+a)^{-s}$ . One solves the sums involving higher moments analogously, like e.g.:

$$\begin{aligned} \sum_{n=1}^N n^2 \log \left( \frac{n}{n+1} \right) &= \\ &= -\frac{1}{6} + 2 \log(A) - \log(\Gamma[N+2]) + \zeta'[-2, N+1] - \zeta'[-2, N+2] + 2\zeta'[-1, N+2], \end{aligned} \quad (4.18)$$

where  $A = 1.282427 \dots$  denotes the Glaisher-Kinkelin constant.

For the asymptotic expansion of the first sum, in a region where  $\Lambda R$  becomes large we simply utilize Stirling's Formula

$$\log(\Gamma[N]) = N(\log(N) - 1) - \frac{1}{2} \log \left( \frac{N}{2\pi} \right) + \frac{1}{12N} + \mathcal{O}(N^{-2}). \quad (4.19)$$

For the sums involving higher powers of  $n$ , the asymptotic expansion of the derivative of the generalized Riemann  $\zeta$  function can be performed according to

$$\begin{aligned}\zeta'[-1, N] &= -\frac{N^2}{4}(1 - 2\log(N)) - \frac{N}{2}\log(N) + \frac{1}{12}(1 + \log(N)) + \frac{1}{720N^2} + \mathcal{O}(N^{-3}), \\ \zeta'[-2, N] &= -\frac{N^3}{9}(1 - 3\log(N)) - \frac{N^2}{2}\log(N) + \frac{N}{12}(1 + 2\log(N)) - \frac{1}{360N} + \mathcal{O}(N^{-3}).\end{aligned}\tag{4.20}$$

It is worth noting at this point that the Riemann  $\zeta$  function is related to the elliptical Jacobi theta function through

$$\int_0^\infty \frac{dt}{t} (\vartheta_n(it) - 1)t^{\frac{s}{2}} = \frac{2}{\pi^{\frac{s}{2}}}\Gamma\left[\frac{s}{2}\right]\zeta[s, 1],\tag{4.21}$$

making our order by order recovery of the results derived with the aide of the theta function not entirely surprising.

The Wilson coefficients reported in eq. (4.11) and eq. (4.15) can therefore be asymptotically expanded for large values of the cutoff scale and we find

$$C_{\text{SM}}(\Lambda) = \frac{g_s^3}{192\pi^2} [4(11C_A - 8n_q T_f)\Lambda R - (21C_A - 16n_q T_f)\log(\Lambda R)] + \mathcal{O}\left(\frac{1}{\Lambda R}\right),\tag{4.22}$$

which agrees to leading order with

$$C_{\text{KK}}(\Lambda) = \frac{g_s^3}{192\pi^2} [4(11C_A - 8n_q T_f)\Lambda R - (42C_A - 32n_q T_f + 9C_F)\log(\Lambda R)] + \mathcal{O}\left(\frac{1}{\Lambda R}\right).\tag{4.23}$$

This serves to show, that they both exhibit the same leading order behavior in a regime where the fifth dimension is being resolved.

For the dipole moment we find

$$D_{q_0 Q_1 G_1} = \frac{g^2}{64\pi^2} (C_A^2 - 4)(C_A - 2C_F) (\log(2\pi) - 2) + \mathcal{O}\left(\frac{1}{\Lambda R}\right).\tag{4.24}$$

The dipole operator therefore stays finite even in the limit  $\Lambda \rightarrow \infty$ .

#### 4.2.4 Exact Renormalization Group Running

It is instructive to perform the same analysis by using the exact functional renormalization group equation FRGE, which we will apply to the 5D uncompactified theory. To put our findings in context we begin by briefly summarizing the derivation of the main tools used. In the review we largely follow Ref. [65], which is based on the original renormalization group work [66, 67].

The Schwinger functional  $W_k[J_i]$  and the generating functional  $Z_0[J_i]$  for an arbitrary theory containing a number of fields  $\Phi_i(x)$  in the presence of an external source  $J$  can be related in the path-integral formalism via

$$\exp \{iW_k [J_i]\} = \int \mathcal{D}\Phi_i \exp \left\{ iS [\Phi_i(x)] + i\Delta S_k [\Phi_i(x)] + i \int d^D x J_n \Phi_n(x) \right\} = Z_0[J_i], \quad (4.25)$$

where we ignore an overall normalization, which is irrelevant for our argument. Additionally we introduced an explicit regulator term  $\Delta S_k$ , designed to suppress the low energy modes below the some intermediate cutoff scale  $k$ . The regulator is usually defined as

$$\Delta S_k [\Phi_i(x)] = \int \frac{d^D p}{2(2\pi)^D} \tilde{\Phi}_j(p) \mathcal{R}_k(p^2) \tilde{\Phi}_j(-p), \quad (4.26)$$

where  $\mathcal{R}_k$  is the regulator shape function. For  $\mathcal{R}_k$  to define a sensible IR cutoff it has to monotonically interpolate between the the UV cutoff  $\Lambda$  (becoming infinite as we push  $\Lambda \rightarrow \infty$ ) and the IR regime (vanishing as  $k \rightarrow 0$ ).

We chose to work with Litim's optimized regulator [68], given by

$$\mathcal{R}_k(p^2) = (k^2 - p^2) \Theta(k^2 - p^2) \quad (4.27)$$

in terms of the Heaviside theta function. This regulator is optimized in the sense described in [69] and allows us to perform the relevant integrals analytically.

We absorb the explicit regulator term into the tree-level action in the following derivation and restore it in the final result.

Splitting the fields  $\Phi_i(x)$  into classical parts  $\phi_i$ , which solve their respective equations of

motion, and quantum parts  $\delta\phi_i(x)$ , it is reasonable to assume that the classical piece will change much more slowly than the quantum piece, such that

$$\begin{aligned} \Phi_i(x) &= \phi_i + \delta\phi_i(x) \\ \Rightarrow Z_0[J_i] &= \int \mathcal{D}\delta\phi_i \exp \left\{ iS[\phi_i + \delta\phi_i] + i\Delta S_k[\phi_i + \delta\phi_i] + i \int d^D x (\phi_n + \delta\phi_n) J_n \right\}, \end{aligned} \quad (4.28)$$

where the path integral over the classical field will only contribute a constant which can be absorbed into the overall normalization.

We now expand the action around the classical solution, where its first derivative with respect to the fields vanishes, marking its saddle point,

$$S[\Phi_i] = S[\phi_i] + \frac{1}{2} \int dx_1 dx_2 \left\{ \delta\phi_m \left( \frac{\delta^2 S}{\delta\Phi_m \delta\Phi_n} \Big|_{\Phi_i=\phi_i} \right) \delta\phi_n \right\} + \dots, \quad (4.29)$$

where we kept terms up to second order, which is consistent up to 1-loop order. The second derivative in brackets signifies the Hessian matrix of the action  $S$ .

Inserting the expansion in our original definition of the Schwinger functional we find

$$\begin{aligned} iW_k[J_i] &= \log \left( \exp \left\{ iS[\phi_i] + \int d^D x J_n \phi_n \right\} \int \mathcal{D}\delta\phi_i \exp \left\{ \frac{i}{2} \int d^D x_1 d^D x_2 \delta\phi_m \frac{\delta^2 S}{\delta\Phi_m \delta\Phi_n} \delta\phi_n \right\} \right) \\ &= iS[\phi_i] + \int d^D x J_n \phi_n + \frac{1}{2} \log \left( \frac{(2\pi)^D}{\det \left| \frac{\delta^2 S}{\delta\Phi_m \delta\Phi_n} \right|} \right) \\ &= i \left[ \Gamma_k[\Phi_i] + \int d^D x J_n \Phi_n \right], \end{aligned} \quad (4.30)$$

where in the middle line we performed the path integral over the fields  $\delta\phi_i$  making use of the generalized Gauss integral

$$\int \mathcal{D}\varphi \exp \left\{ -\frac{i}{2} \int d^D x_1 d^D x_2 \varphi(x_1) A \varphi(x_2) \right\} = \sqrt{\frac{(2\pi)^D}{\det |A|}} \quad (4.31)$$

and in the last equality we defined the effective action as the Legendre transform of the Schwinger functional.

Absorbing all constant pieces into the bare action  $S$  we can read off the saddle point approximation for the effective action

$$\Gamma_k = S - \frac{1}{2} \log \left( \det \left| \frac{\delta^2 S}{\delta \Phi_m \delta \Phi_n} + \mathcal{R}_k \delta_{mn} \right| \right). \quad (4.32)$$

Since we will be dealing with theories that contain two types of fields at a time it is useful to note that the Hessian is a  $2 \times 2$  block matrix. In order to solve the determinant inside the logarithm it is necessary to make use of a general determinant identity

$$\det \begin{vmatrix} A & B \\ C & D \end{vmatrix} = \det |D| \det |A - CD^{-1}B| \quad (4.33)$$

and then apply the trace identity

$$\log \left( \det |A| \right) = \text{Tr} \langle x | \log(A) | x \rangle \quad (4.34)$$

to the pieces remaining inside the logarithm. Note that this identity is well defined through the insertion of an arbitrary complete set of eigenstates  $|x\rangle$ .

Taking the derivative of the effective action with respect to the renormalization time parameter  $t = \log \left( \frac{k}{k_0} \right)$  we arrive at an one-loop exact integro-differential equation describing the flow of the coarse-grained effective action between the two fixed points  $k = 0$ , where no modes are integrated out, such that  $\Gamma_0$  represents the full quantum action  $\Gamma$ , and  $k = \Lambda$ , where all modes are integrated out and we are left with the classical action  $\Gamma_\Lambda = S$ . The so-found flow equation that interpolates the two regimes, can schematically be written as

$$\partial_t \Gamma_k = \frac{1}{2} \text{Tr} \left[ \partial_t \mathcal{R}_k \left( \frac{\partial^2 S}{\partial \Phi \partial \Phi} \right) + \mathcal{R}_k^{-1} \right]. \quad (4.35)$$

This procedure represents the one-loop approximation of the general concept found in Ref. [67]. We chose to solve the flow equation through the non-local heat kernel expansion [70–74], which is based on the fact that the term under the trace on the right-hand-side of (4.35) is generally of the form of a heat kernel

$$h_k(\Delta, \omega) = \frac{\partial_t \mathcal{R}_k(\Delta)}{\Delta + \omega + \mathcal{R}_k(\Delta)}. \quad (4.36)$$

In all our considerations the heat kernel will depend on a second derivative Laplace type operator  $\Delta$ , that is related to the covariant derivative of the theory under consideration through

$$\Delta = -D_M D^M + U, \quad (4.37)$$

where  $U$  denotes the non-derivative part of the operator.

The trace over the heat kernel can be asymptotically expanded in terms of so-called non-local structure functions [70–74]. We furthermore define the gauge connection  $\Omega_{MN} = \frac{i}{g} [D_M, D_N]$ . For a flat background metric the asymptotic form of the flow equation then becomes

$$\partial_t \Gamma_k = \frac{1}{2(4\pi)^{\frac{D}{2}}} \int d^D x \left[ \text{Tr}[\mathbb{1}] Q_{\frac{D}{2}} [h_k] + \text{Tr} [U g_U U] + \text{Tr} [\Omega_{MN} g_\Omega \Omega^{MN}] \right]. \quad (4.38)$$

The structure functions appearing in the expansion can be conveniently defined with the help of a basis of "Q-functionals" [87]

$$\begin{aligned} g_U(z, k) &= \frac{1}{2} \int_0^1 d\xi Q_{\frac{D}{2}-1} \left[ h_k^{z\xi(1-\xi)} \right], \\ g_\Omega(z, k) &= \frac{1}{2z} Q_{\frac{D}{2}-1} [h_k] - \frac{1}{2z} \int_0^1 d\xi Q_{\frac{D}{2}-1} \left[ h_k^{z\xi(1-\xi)} \right], \end{aligned} \quad (4.39)$$

where the  $Q$  functionals are in turn related to the original heat kernel of our theory in question through

$$Q_n [h_k^a] = \int_0^\infty ds s^{-n} \tilde{h}_k(s+a, w) = \int_0^\infty ds s^{-n} e^{-sa} \tilde{h}_k(s, w), \quad (4.40)$$

where  $\tilde{h}_k$  denotes the Laplace transform of  $h_k$ . The second equality explains the short-hand notation used to describe a heat kernel with a shifted argument.

It is possible to bring the  $Q$ -functionals into a more convenient form by applying a Mellin transformation. This leads to

$$\begin{aligned} Q_n [h_k] &= \frac{1}{\Gamma[n]} \int_0^\infty ds s^{n-1} h_k(s, w) \quad \text{for } n > 0, \\ Q_{-n} [h_k] &= (-1)^n \frac{\partial^n}{\partial s^n} h_k(s, w) \Big|_{s=0} \quad \text{for } n \in \mathbb{Z} \leq 0. \end{aligned} \quad (4.41)$$

From those identities we can calculate all special cases appearing in our analysis. Choosing Litim's regulator as mentioned earlier, we find the remaining relevant functionals not explicitly stated in the literature, namely

$$\begin{aligned} Q_{\frac{1}{2}}[h_k^a] &= \frac{4}{\sqrt{\pi}} \sqrt{k^2 - a}, \\ Q_{\frac{3}{2}}[h_k^a] &= \frac{8}{3\sqrt{\pi}} \left( \sqrt{k^2 - a} \right)^3. \end{aligned} \quad (4.42)$$

Furthermore it is useful to already mention the integrals over those two functionals with shifted arguments, as they appear in the definition of the structure functions

$$\begin{aligned} \int_0^1 d\xi Q_{\frac{1}{2}} \left[ h_k^{z\xi(1-\xi)} \right] &= \frac{2k^2}{\sqrt{\pi}(k^2 + \omega^2)} \left( k - \frac{(z - 4k^2)}{2\sqrt{z}} \text{ArcTanh} \frac{\sqrt{z}}{4k} \right), \\ \int_0^1 d\xi Q_{\frac{3}{2}} \left[ h_k^{z\xi(1-\xi)} \right] &= \frac{k^2}{\sqrt{\pi}(k^2 + \omega^2)} \left( 5k^3 - \frac{3kz}{4} - \frac{3}{8\sqrt{z}} (z - 4k^2)^2 \text{ArcTanh} \frac{\sqrt{z}}{4k} \right). \end{aligned} \quad (4.43)$$

**4.2.4.1 QED-like Contributions** To compare the results extracted from the FREG with the explicit one-loop calculation performed earlier we analyze the contributions stemming from QED-like interactions separately from the ones stemming from QCD-like interactions. The general strategy on how to solve the flow equation at one loop for QED and QCD can be found in Ref. [75].

It is sufficient to consider the QED contributions as they appear for the Yang-Mills term of the theory. Through 5D gauge invariance all interaction terms in question acquire the same Wilson coefficient.

The one-loop effective action for 5D quantum electrodynamics, containing a massless fermion, can be found in the literature, e.g. [76]. We start from the classical action

$$S_{\text{QED}} = \int d^D x \left\{ \frac{1}{2} A_M \left( \partial^2 \eta^{MN} - \left( 1 - \frac{1}{\xi} \right) \partial^M \partial^N \right) A_N + i \bar{\psi} \not{D} \psi \right\}. \quad (4.44)$$

to which we apply the one-loop saddle point approximation (4.32). The resulting effective action is then

$$\begin{aligned} \Gamma_{\text{1-loop}} = S_{\text{QED}} + \frac{1}{2} \text{Tr} \left\langle x \left| \log \left( \left( -\partial^2 \eta^{MN} + \left( 1 - \frac{1}{\xi} \right) \partial^M \partial^N \right) - g^2 \bar{\psi} \gamma^M \frac{1}{i \not{D}} \gamma^N \psi \right) \right| x \right\rangle \\ - \text{Tr} \langle x | \log (i \not{D}) | x \rangle. \end{aligned} \quad (4.45)$$

Working from this general result we can bring the second term into the form of a heat kernel by noting that

$$\mathrm{Tr} \langle x | \log (i\mathcal{D}) | x \rangle = \frac{1}{2} \mathrm{Tr} \langle x | \log \left( -\mathcal{D}^2 \right) | x \rangle = \frac{1}{2} \mathrm{Tr} \langle x | \log \left( -D^2 - \frac{g}{2} \sigma^{MN} F_{MN} \right) | x \rangle^\dagger. \quad (4.46)$$

For simplicity we ignore the last term in the logarithm in eq. (4.45), since we are not interested in operators with fermions as external legs at this point. Taking then the derivative of the effective action yields

$$\partial_t \Gamma_k = \frac{1}{2} \mathrm{Tr} \left[ \frac{\partial_t R_k (-\partial^2)^{MN}}{-\partial^2 \eta^{MN} + R_k (-\partial^2)^{MN}} \right] - \frac{1}{2} \mathrm{Tr} \left[ \frac{\partial_t R_k (\Delta)}{-D^2 + U + R_k (\Delta)} \right], \quad (4.47)$$

which is the desired heat kernel form of the flow equation.

Next we identify the field monomials from which our non-local expansion is built

$$U = -\frac{1}{2} \sigma^{MN} F_{MN} \quad \text{and} \quad \Omega_{MN} = iF_{MN}. \quad (4.48)$$

The expansion of the flow equation then reads

$$\partial_t \Gamma_k = -\frac{T_f}{2} \frac{1}{(4\pi)^{\frac{D}{2}}} \int d^D x \left[ \mathrm{Tr} [\mathbf{1}] Q_{\frac{D}{2}} [h_k] + F_{MN} (2g_U - Dg_\Omega) F^{MN} \right].^\ddagger \quad (4.49)$$

To extract the the coefficients we wish to compare with our previous results we make the well-motivated Ansatz for the effective action

$$\Gamma_k [A] \Big|_{F^2} = \int d^D x \frac{Z_k}{4} F_{MN}^a [\delta^{ab} + \Pi_k^{ab} (-D^2)] F^{b,MN}, \quad (4.50)$$

---

<sup>†</sup>The second equality holds, since  $\not{x} \not{b} = a_M b^N - i a_M \sigma^{MN} b_N$ .

<sup>‡</sup>For the Dirac trace we used the facts that  $\{\Gamma_M, \Gamma_N\} = 2\eta_{MN}$ ,  $\mathrm{Tr} [\Gamma^M \Gamma^N] = 4\eta^{MN}$  and  $\mathrm{Tr} [\Gamma^K \Gamma^L \Gamma^M \Gamma^N] = 4(\eta^{KL} \eta^{MN} - \eta^{KM} \eta^{LN} + \eta^{KN} \eta^{LM})$  as well as  $\Gamma_M \Gamma^M = 5$  and for the color trace  $\mathrm{Tr} [T^a, T^b] = T_f \delta^{ab}$

of which we will take the derivative with respect to the renormalization scale and match to the non-local expansion in eq. (4.49). This leads us to a differential equation for the scale dependent polarization function and the field renormalization constant

$$\partial_t (Z_k(1 + \Pi_k(z))) = -\frac{T_f}{(4\pi)^{D/2}} \int_0^1 d\xi Q_{\frac{D}{2}-2}[h_k] + \frac{D}{2z} \left( Q_{\frac{D}{2}-1}[h_k] - Q_{\frac{D}{2}-1} \left[ h_k^{z\xi(1-\xi)} \right] \right), \quad (4.51)$$

where we use the short-hand notation  $z = -D^2$  and introduced the Dynkin index by taking the color trace  $Tr[T^a T^b] = T_f \delta^{ab}$  in our expansion.

We solve this equation firstly in the limit of zero momentum transfer  $z \rightarrow 0$ , since we know that the polarization function vanishes  $\Pi_k(0) = 0$ . In that limit the right hand side of eq. (4.51) changes like

$$\begin{aligned} \frac{1}{2z} \int_0^\infty d\xi \left[ Q_{\frac{D}{2}-1}[h_k] - Q_{\frac{D}{2}-1} \left[ h_k^{z\xi(1-\xi)} \right] \right] &\xrightarrow{z \rightarrow 0} \int_0^\infty d\xi \left[ \frac{1}{2} \xi(1-\xi) Q_{\frac{D}{2}-2}[h_k] \right] \\ &= \frac{1}{12} Q_{\frac{D}{2}-2}[h_k]. \end{aligned} \quad (4.52)$$

We arrive at a simple differential equation for the field renormalization

$$\partial_t Z_k = \frac{T_f}{3\pi} Q_{\frac{D}{2}-2}[h_k], \quad (4.53)$$

which can be integrated to yield both the QED-contribution to the anomalous dimension of the gluon field, as well as the beta function. We write them in terms of the 4D couplings  $g^{(5)} = g\sqrt{\pi R}$

$$\eta_k^{\text{QED}} = -\frac{\partial_t Z_k}{Z_k} = T_f \frac{g^2}{3\pi^2} kR \quad \text{and} \quad \partial_k \alpha_s^{-1} = -\frac{2T_f}{3\pi} R, \quad (4.54)$$

where we used the identification  $Z_k = \frac{1}{g^{(5)2}}$ .

With these results we can solve the original differential equation for the polarization function, which now reads

$$\begin{aligned} \partial_t \Pi_k(z) &= \eta_k^{\text{QED}} (1 + \Pi_k(z)) \\ &+ \frac{1}{Z_k} \frac{T_f}{64\pi^3 z^{3/2}} \left[ 2k(4k^2 - 3z) \sqrt{z} - (4k^2 - z)(12k^2 + 29z^2) \text{ArcTanh} \left( \frac{\sqrt{z}}{k} \right) \right], \end{aligned} \quad (4.55)$$

where we have to drop the term proportional to  $\Pi_k$  on the right hand side, since it gives rise to terms  $\mathcal{O}(g^4)$ .

We can now integrate the flow down from the UV cutoff  $\Lambda$  to an infrared scale  $k$ . The theory is well-behaved in the UV and the polarization function vanishes there, such that  $\Pi_\Lambda(z) = 0$  for any  $z$ . This leaves us with

$$\begin{aligned} \Pi_k(z) = \frac{T_f g^2}{768\pi^3 z^{3/2}} & \left[ -2k(12k^2 + 13z)\sqrt{z} + 3(4k^2 - z)(4k^2 + 5z)\text{ArcTanh}\left(\frac{\sqrt{z}}{k}\right) \right. \\ & \left. + 18z^2 \left( \text{Li}_2\left(\frac{\sqrt{z}}{2k}\right) - \text{Li}_2\left(-\frac{\sqrt{z}}{2k}\right) \right) \right], \end{aligned} \quad (4.56)$$

for  $n_q$  flavors of quarks.

We cannot perform the limit  $k \rightarrow 0$ , where the polarization function is badly divergent. This signifies a breakdown of the validity of our perturbation theory in the regime where QCD becomes strongly coupled.

**4.2.4.2 QCD-like Contributions** Similarly to the previous section we now construct the effective action for QCD-like contributions. This is best done using background field gauge [77]. We follow the spirit and notation of Ref. [78] and split the field in a classical background field and a fluctuation as done in eq. (4.28)

$$A_M = \bar{A}_M + \delta A_M. \quad (4.57)$$

The tree-level action then takes the form

$$S_{\text{QCD}} = \int d^D x - \frac{1}{4} F_{MN}^a F^{a,MN} - \frac{1}{2\xi} \left( \bar{D}_M^{ab} \delta A^{a,M} \right)^2 - \left( D_M^{ab} \bar{c}^b \right) \left( \bar{D}^{M,ac} c^c \right), \quad (4.58)$$

where  $\bar{D}_M$  denotes the derivative with respect to the background field, while  $D_M$  contains the full field.  $c_a$  is the corresponding Faddeev-Popov ghost.

The effective action  $\Gamma[A, c, \bar{c}; \bar{A}]$  is not only dependent on the full field  $A_M$  but also explicitly depends on the classical field, which enters through the gauge fixing. It is necessarily not invariant under original gauge transformation, since the gauge fixing is necessary to perform the path integral.

On the other hand it is invariant under an extended set of gauge transformations provided the

classical field transforms simultaneously. The full set of infinitesimally gauge transformations with local gauge parameter  $\theta(x)$

$$\begin{aligned}\delta A_M^a &= -D_M^{ab}\theta^b(x), \\ \delta \bar{A}_M^a &= -\bar{D}_M^{ab}\theta^b(x), \\ \delta c^b &= -ig\theta^a(x)(T_A^a)^{bc}c^c,\end{aligned}\tag{4.59}$$

where  $T_A^a$  is the set of generator matrices in the adjoint representation.

The effective action takes its simplest form for  $A_M = \bar{A}_M$  in which case the first two transformations in (4.59) become identical and the whole set is of the standard gauge transformation form under which the newly constructed action  $\Gamma[A, c, \bar{c}; A]$  is invariant.

Using the background field method one can construct the renormalization flow equation, which we quote from [87]

$$\partial_t \Gamma[\bar{A}] = \frac{1}{2} \text{Tr} \left[ \frac{\partial_t \mathcal{R}_k(\bar{D}_T) - \eta_k^A \mathcal{R}_k(\bar{D}_T)}{\bar{D}_T + \mathcal{R}_k(\bar{D}_T)} \right] - \text{Tr} \left[ \frac{\partial_t \mathcal{R}_k(-\bar{D}^2) - \eta_k^A \mathcal{R}_k(-\bar{D}^2)}{-\bar{D}^2 + \mathcal{R}_k(-\bar{D}^2)} \right], \tag{4.60}$$

with the covariant Laplacian  $(D_T)_{MN}^{ab} = (-D^2)^{ab} \eta_{MN} + U_{MN}^{ab}$ . We can immediately determine our building blocks for the non-local expansion, namely

$$U_{MN}^{ab} = 2f^{abc} F_{MN}^c \quad \text{and} \quad \Omega_{MN}^{ab} = -f^{abc} F_{MN}^c. \tag{4.61}$$

Comparing the resulting flow equation with the derivative of our ansatz we arrive again at a differential equation for field renormalization and polarization function

$$\partial_t (Z_k(1 + \Pi_k(z))) = \frac{C_A}{(4\pi)^{D/2}} \int d\xi 4Q_{\frac{D}{2}-2} \left[ h_k^{z\xi(1-\xi)} \right] + \frac{D-2}{z} \left[ Q_{\frac{D}{2}-1} \left[ h_k^{z\xi(1-\xi)} \right] - Q_{\frac{D}{2}-1} [h_k] \right]. \tag{4.62}$$

In the limit  $z = 0$  the polarization function again vanishes,  $\Pi(0) = 0$ , and the differential equation simplifies to

$$\partial_t Z_k = \frac{C_A}{(4\pi)^{D/2}} \frac{26-D}{6} Q_{\frac{D}{2}-2} [h_k], \tag{4.63}$$

where we can extract the the QCD-contributions to the anomalous dimension and to the beta function after evaluating the  $Q$ -functionals. In  $D = 5$  we find in terms of the 4D coupling constants

$$\eta_k^{\text{QCD}} = -\frac{\partial_t Z_k}{Z_k} = -7C_A \frac{g^2}{16\pi^2} kR \quad \text{and} \quad \partial_k \alpha_s^{-1} = \frac{7C_A}{4\pi} R. \quad (4.64)$$

Substituting those results back into the full equation and solving for the polarization function we find

$$\begin{aligned} \partial_t \Pi_k(z) = & \eta_k^{\text{QCD}} (1 + \Pi_k(z)) \\ & - \frac{1}{Z_k} \frac{C_A}{256\pi^3 z^{3/2}} \left[ 2k(12k^2 - 29z)\sqrt{z} - (4k^2 - z)(12k^2 + 29z)\text{ArcTanh}\left(\frac{\sqrt{z}}{k}\right) \right], \end{aligned} \quad (4.65)$$

which can be integrated down from  $\Lambda$  to an IR cutoff scale  $k$ , at which we become non-perturbative. Again we find  $\Pi_\Lambda(z) \rightarrow 0$  as  $\Lambda$  reaches infinity, leaving us with a polarization function dependent on  $k$

$$\begin{aligned} \Pi_k(z) = & \frac{C_A g^2}{1024\pi^3 z^{3/2}} \left[ 2k(12k^2 + 53z)\sqrt{z} - (4k^2 - z)(12k^2 + 55z)\text{ArcTanh}\left(\frac{\sqrt{z}}{k}\right) \right. \\ & \left. - 58z^2 \left( \text{Li}_2\left(\frac{\sqrt{z}}{2k}\right) - \text{Li}_2\left(-\frac{\sqrt{z}}{2k}\right) \right) \right]. \end{aligned} \quad (4.66)$$

The limit  $k \rightarrow 0$  on the other hand is not save, marking a break down of our theory, and remains regulated.

### 4.3 PHENOMENOLOGICAL ANALYSIS

From eqs. (4.54) and (4.64) one finds that the cutoff dependence of the effective gauge coupling is given by

$$\frac{1}{g_s(\Lambda)} - \frac{1}{g_s(0)} = \frac{g_s^3}{8\pi^2} \left( \frac{7}{4} C_A - \frac{4}{3} n_q T_f \right) \Lambda R. \quad (4.67)$$

Since this was obtained in the framework of an uncompactified 5D theory, there is no distinction between couplings of zero modes and higher KK modes.

The result in eq. (4.67) is numerically close, but not identical to the linear  $\Lambda R$  terms in eqs. (4.22) and (4.23). The difference stems from threshold corrections that contribute to (4.22) and (4.23) at each KK level. Thus, even when we study the dependence of the effective vertex coupling on  $\Lambda$  for  $\Lambda R \gg 1$ , i.e. at scales much beyond the compactification radius, there is a non-vanishing impact of the compactification. In other words, when considering mUED at large scales one does not trivially recover the uncompactified 5D theory.

This is illustrated in Fig. 18. In this plot it is assumed that there is some fundamental 5D coupling at the scale  $\Lambda_0 = 20R^{-1}$ . The curves illustrate the effect of integrating out all energy scales beyond  $\Lambda R^{-1}$  in different approximations. The solid blue line corresponds to the result (4.67) from the flow equation. The solid green curve depicts the result from the explicit calculation of the  $gq\bar{q}$  vertex diagrams, as in eq. (4.11) with  $\mu = \Lambda$ , whereas the solid orange curve is the approximation (4.22). The dotted green and orange curves are the equivalent cases for the  $G_1 Q_1 \bar{q}$  vertex, eqs. (4.15) and (4.23). The vertical axis is normalized such that the effective  $gq\bar{q}$  coupling at  $n = 1$  is equal to its SM value.

First of all, the plot demonstrates that the large- $\Lambda R$  expansions (orange) provide an excellent approximation to the level-by-level calculations (green). Furthermore, it shows that all approaches lead to similar results for the dependence of the effective gauge couplings on the truncation scale. However, there are differences at the few-percent level, which stem from the following two facts: The flow equation is insensitive to threshold corrections from the compactification; and the  $G_1 Q_1 \bar{q}$  and  $gq\bar{q}$  vertices have different logarithmic dependencies on  $\Lambda$ . Note that the plot also includes the running from the coloron contribution, see eq. (3.9). From a low-energy perspective, on the other hand, the dependence of the gauge vertices on

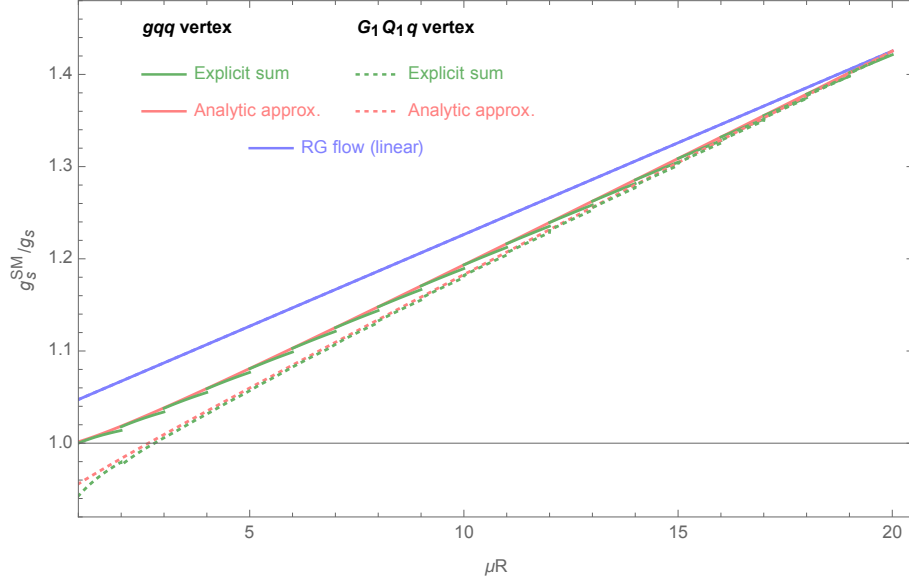


Figure 18: Running of the SM vertex function  $q_0 - q_0 - g_0$  (solid line) and the KK vertex  $q_0 - Q_1 - G_1$  (dashed line). We compare the full summation up to the cutoff with the asymptotic expansion as well as the results obtained from the FRGE running. The integration constants have been fixed such that the couplings coincide at  $\Lambda R = 20$ .

the cutoff  $\Lambda$  is not directly observable. However, if KK gluons and KK quarks should be discovered in the future, one can compare the strength of the SM  $gq\bar{q}$  coupling with the  $G_1 Q_1 \bar{q}$  vertex. While the leading linear  $\Lambda R$  dependence drops out in this difference, there is still some sensitivity to the cutoff scale from the logarithmic terms in eqs. (4.22) and (4.23):

$$C_{g_0 Q_1 G_1}(\Lambda) - C_{q_0 q_0 g_0}(\Lambda) = -\frac{g_s^3}{192\pi^2} (21C_A + 9C_F - 16n_q T_f) \log(\Lambda R) + \mathcal{O}\left(\frac{1}{\Lambda R}\right). \quad (4.68)$$

Including the contribution to the running from the lowest modes, see eq. (3.9), and assuming that the  $gq\bar{q}$  and  $G_1 Q_1 \bar{q}$  couplings are identical at the scale  $\mu = \Lambda$ , one finds that the observable couplings depends on  $\Lambda$  as follows:

$$\frac{g_{g_0 Q_1 G_1}(R^{-1})}{g_{q_0 q_0 g_0}(R^{-1})} \approx \frac{23g_s^2}{192\pi^2} \log(\Lambda R). \quad (4.69)$$

For  $\Lambda R = 10 \dots 50$ , this amounts to an effect between 3.5% and 6%.

This means that the prediction of the decay rate for  $G_1 \rightarrow Q_1 \bar{q}$ , including  $\mathcal{O}(\alpha_s)$  corrections,

depends on the unknown UV completion of mUED. At the same time, the impact of this UV sensitivity is rather mild, at the level of a few percent, which may be negligible for most practical purposes.

While a more complete analysis of different processes in mUED and larger classes of extra-dimensional models is beyond the scope of this work, we expect that a similar conclusion can be reached in these cases. This conjecture is based on our observation that the leading UV sensitivity cancels when normalizing the KK gauge boson vertex to the SM gauge boson vertex, as dictated by the renormalization flow equation. The cancellation still works when including the threshold corrections at each KK level, and thus it should hold in any extra-dimensional extension of the SM. The next-to-leading term, while enhanced by  $\log(\Lambda R)$ , is nevertheless numerically rather modest.

#### 4.4 SUMMARY AND CONCLUSIONS

As discussed in chapter 2 do models with extra dimensions generally feature infinite KK-towers of new states that need to be considered when calculating loop corrections within those models. KK-number conserving operators receive corrections from the full spectrum of these modes. The corrections are in general dependent on a cutoff scale  $\Lambda$  at which the model breaks down and some unspecified UV completion is required to describe the physics. In this article we investigated the numerical impact of this unknown cutoff parameter on physical observables. As a concrete framework we considered QCD in a spacetime with one additional universal extra dimension, which is compactified on a circle with a  $\mathbb{Z}_2$  orbifold. In the first half of this article, the problem was discussed from the viewpoint of the compactified 4D effective theory. We computed the full one-loop QCD corrections to the SM gauge-boson vertex  $gq\bar{q}$  as well as the vertex  $G_1 Q_1 \bar{q}$  (or, equivalently,  $G_1 \bar{Q}_1 q$ ), which contains two level-1 KK modes. These include vertex diagrams, on-shell counterterms for the external legs, and  $\overline{\text{MS}}$  coupling counterterms generated by loops up to KK level  $n$ . The  $\overline{\text{MS}}$  scale dependence of the  $gq\bar{q}$  vertex can be described through the regular QCD beta function, where the well-known SM result is supplemented by an extra term each time one of the KK

thresholds is crossed. Additionally, the Wilson coefficient of the  $gq/\bar{q}$  vertex receives a finite threshold correction from each KK level, which is not described by the beta function.

For the  $G_1Q_1\bar{q}$  ( $G_1\bar{Q}_1q$ ) vertex we proceeded similarly. For concreteness, we considered the physical process  $G_1 \rightarrow \bar{q}Q_1$ . The NLO corrections to this decay exhibit soft divergencies in the virtual vertex contributions, which can be canceled against the real radiation contributions with the two cutoff phase-space slicing method. This part of the calculation is identical to a 4D coloron model. Overall, the beta function for this vertex differs from the SM  $gq/\bar{q}$  vertex, but the contribution from higher KK modes ( $n > 1$ ) is identical for the  $gq\bar{q}$  and  $G_1Q_1\bar{q}$  beta functions. Furthermore, the Wilson coefficient for the  $G_1Q_1\bar{q}$  vertex receives KK threshold corrections, which differ from the ones found for the SM vertex.

The results for both vertices can be conveniently written in terms of an expansion for large values of the cutoff scale  $\Lambda$ . It turns out that their leading terms, which are linear in  $\Lambda R$ , are identical. The first difference between the two vertices appears at the subleading order  $\log(\Lambda R)$ . Higher orders beyond the log term are numerically very small and can be neglected.

In the second half, we studied the cutoff dependence within uncompactified 5D QCD, using the functional renormalization group flow equation. To solve the equation and extract the beta function we applied the saddle-point approximation and utilized the non-local heat kernel expansion method. Through this approach we were able to find the flow equation analogue of the one-loop beta function. Its coefficient coincides with the leading order behavior of the running of the coupling found for the explicit diagrammatic calculation in the compactified theory. However, the uncompactified 5D framework is not able to reproduce the contributions from the threshold corrections in the 4D framework.

When comparing the diagrammatic 4D calculations of the  $gq\bar{q}$  and  $G_1Q_1\bar{q}$  vertices, as well as the 5D flow equation result, one finds that the NLO prediction for the decay  $G_1 \rightarrow \bar{q}Q_1$  is indeed sensitive to the choice of the UV cutoff and thus to the unknown high-scale physics. However, the numerical impact of this uncertainty is numerically rather modest, since the leading contributions cancel in the comparison.

## 5.0 RADIATIVE CORRECTIONS TO MASSES AND VERTICES IN MUED

Having discussed the pair-production of level-1 modes we can now ask how that picture changes for higher modes in the spectrum. Since those modes are heavier than the first excitation one would naïvely assume their phenomenology plays a sub-leading role. As we however discussed in Chapter 2 can radiative corrections induce KK-number violating couplings, which for a number of level-2 modes means that they can couple to a pair of SM modes through a one-loop process, conserving parity. Therefore the level-2 modes do not need to be pair produced and lead to drastically different detector signatures than the level-1 modes did.

In [79] we calculate the full one-loop improved mass spectrum of the KK-modes and the induced couplings. Generally speaking the resulting contributions are logarithmically divergent and stem from 5D operators localized on the boundary, that violate KK-number. The logarithmic pieces  $\log \Lambda R$  for the mass corrections and a number of processes have been reported in the literature. For typical values of  $\Lambda R \sim 10 \dots 50$ , those logarithms are however of similar magnitude as the non-logarithmic, finite contributions, and therefore might impact the phenomenology considerably. The remaining finite terms are calculated and their phenomenological impact is discussed. We additionally find previously unconsidered couplings, that do not depend on  $\log \Lambda R$  but are nevertheless non-zero.

### 5.1 MASS CORRECTIONS

The KK modes of fields propagating in a compactified extra dimension receive loop-induced corrections to the basic geometric mass relation  $m_n = n/R$ . These corrections stem from

contributions where the loop propagators wrap around the extra dimension. They can be separated into two categories: bulk and boundary mass corrections [39, 80].

While the bulk corrections are present in extra-dimensional models with and without orbifolding, and they lead to mass terms that are independent of  $x^5$  and conserve KK number, the boundary terms are a consequence of the orbifolding condition, and they lead to mass terms that are localized in the extra dimension. For example, for a scalar field, the boundary mass correction has the form

$$\mathcal{L} \supset \frac{\pi R}{2} [\delta(x^5) + \delta(x^5 + \pi R)] \Phi^\dagger \partial_5^2 \Phi. \quad (5.1)$$

These boundary terms break KK number.

Both the bulk and boundary corrections are induced first at one-loop order. Whereas the bulk corrections are UV finite, the boundary contributions are UV divergent and must be renormalized. We employ  $\overline{\text{MS}}$  renormalization for this purpose, with the  $\overline{\text{MS}}$  scale set to the cut-off scale  $\Lambda$ .

### 5.1.1 Approach

To compute the mass corrections we choose to work in the effective 4D theory. Every self-energy diagram contributing to the corrections of a given mode contains the infinite tower of increasingly heavy KK-modes running in the loop and needs to be treated in a manner similar to the one described in Ref. [80]. We will begin by describing the general procedure employed on the example of diagram (A) in Fig. 19. For a vector boson the self-energy can be decomposed into covariants according to

$$\Pi_{\mu\nu}^{ab}(p^2) = - \left[ \eta_{\mu\nu} \left( p^2 \Pi_{\text{T}}^{(1)}(p^2) + M_n^2 \Pi_{\text{T}}^{(2)}(p^2) \right) - p_\mu p_\nu \Pi_2(p^2) \right] \delta^{ab}, \quad (5.2)$$

where additionally to the usual transverse part  $\Pi_{\text{T}}^{(1)}$  a second contribution  $\Pi_{\text{T}}^{(2)}$  emerges as a proportionality constant to the fifth momentum component.

The mass correction is then defined as

$$\delta M_{V_n}^2 = -M_n^2 \Re \left\{ \Pi_{\text{T}}^{(1)}(M_n^2) + \Pi_{\text{T}}^{(2)}(M_n^2) \right\}. \quad (5.3)$$

Both the self-energy and the resulting mass correction are dependent on an infinite sum over all heavy modes running in the loop, which in turn is divergent. To find a sensible regularization scheme we first make use of the Poisson summation identity

$$\sum_{n=-\infty}^{\infty} f(n) = \sum_{k=-\infty}^{\infty} \mathcal{F}\{f\}(k) \quad (5.4)$$

where the Fourier transform  $\mathcal{F}$  is defined as

$$\mathcal{F}\{f\}(k) = \int_{-\infty}^{\infty} dx e^{-2\pi i k x} f(x). \quad (5.5)$$

By applying the identity to the divergent mass correction, the sum over KK-numbers is transformed into a sum of winding numbers in position space about the fifth dimension. The most straightforward way to define a physical observable is to subtract the (formally infinite) contribution of the zero winding number from the sum, since it is equivalent to the diagram in the 5D uncompactified theory.

For our example we restrict ourselves to the mass correction of the first vector mode; all higher modes can be found by rescaling the mode number. The example diagram then amounts to a mass correction described by

$$\begin{aligned} \delta M_{V_1}^2 = & \frac{g^2}{32\pi^2} C_A \frac{34 - 41d + 11d^2}{(d-3)(d-1)} A_0(M^2) \\ & + \frac{g^2}{32\pi^2(d-1)} C_A \sum_{n=1}^{\infty} \left\{ [n(3-2d) + d-1] A_0(n^2 M^2) \right. \\ & - [(n+1)(3-2d) - d+1] A_0((n+1)^2 M^2) \\ & \left. + M^2(d-1)(5+2n+2n^2) B_0(M^2, n^2 M^2, (n+1)^2 M^2) \right\}, \quad (5.6) \end{aligned}$$

where  $d = 4 - 2\epsilon$  is the number of space-time dimensions in dimensional regularization, and the term outside the sum stems from the diagram with a zero mode (massless SM vector boson) in the loop.

The explicit form of the  $A_0$  and  $B_0$  functions appearing in the equation are well-known and can be written as

$$A_0(M^2) = M^2 \left( \frac{1}{\epsilon} + 1 - \ln \frac{M^2}{\mu^2} \right), \quad (5.7)$$

$$B_0(M^2, (n+1)^2 M^2, n^2 M^2) = \frac{1}{\epsilon} + 2 - \ln \frac{M^2}{\mu^2} + 2[n \log(n) - (n+1) \log(n+1)]. \quad (5.8)$$

Splitting up the first term in order to extend the sum to include  $n = 0$  and taking the the limit  $d \rightarrow 4$  yields

$$\delta M_{V_1}^2 = \frac{23g^2}{96\pi^2} C_A M^2 \left( \frac{112}{69} + \ln \frac{\Lambda^2}{M^2} \right) + \frac{g^2}{8\pi^2} C_A \sum_{n=0}^{\infty} n^2 \ln n \quad (5.9)$$

where any polynomial terms under the sum have been dropped since their Fourier transform only amounts to derivatives of delta functions. Note that we assumed the existence of a  $\overline{\text{MS}}$  UV-counterterm at the cut-off scale  $\mu = \Lambda$  to cancel the divergence in the remainder.

The remaining sum is now treated as outlined above, starting from the Fourier transform

$$\int_{-\infty}^{\infty} dx |x|^2 \ln |x| e^{2\pi i k x} = \frac{1}{4\pi^2 |k|^3} + \frac{\gamma_E}{4\pi^2} \delta^{(2)}(k), \quad (5.10)$$

where  $\delta^{(n)}$  denotes the n-th distribution derivative of the Dirac  $\delta$ -function.

Dropping the zero winding number ( $k=0$ ) piece, we can identify the finite rest in terms of the Riemann  $\zeta$ -function

$$\sum_{n=0}^{\infty} |n|^2 \ln |n| = \frac{1}{8\pi^2} \sum_{k=-\infty}^{\infty} \left( \frac{1}{|k|^3} + \gamma_E \delta^{(2)}(k) \right) \sim \frac{\zeta(3)}{4\pi^2}. \quad (5.11)$$

The finite contribution to the mass correction stemming from diagram (A) then is given by

$$\delta M_{V_n}^2 = \frac{g^2 M_n^2}{32\pi^2} C_A \left( \frac{23}{3} L_n + \frac{112}{9} + \frac{\zeta(3)}{\pi^2} \right), \quad (5.12)$$

where  $L_n = \ln(\Lambda^2/m_n^2)$ . The last term in parenthesis, proportional to  $\zeta(3)$ , can be identified as a contribution to the bulk mass correction [80], so that the remaining two terms belong to the boundary mass correction. In a similar fashion, the contribution from other diagrams in Fig. 19 to the boundary corrections can be singled out.

Analogously we decompose the fermion self-energies displayed in Fig. 21 according to

$$\Sigma_f^{ij}(p^2) = [\not{p} P_+ \Sigma_R(p^2) + \not{p} P_- (p^2) \Sigma_L(p^2) + M_n \Sigma_S(p^2)] \delta^{ij}, \quad (5.13)$$

with fundamental  $\text{SU}(N)$  indices  $i, j$ , and  $P_{\pm} \equiv (1 \pm \gamma_5)/2$ . The fermion mass correction is then given by

$$\delta M_{f_n} = \frac{M_n}{2} \Re \{ \Sigma_R(M_n^2) + \Sigma_L(M_n^2) + 2\Sigma_S(M_n^2) \}, \quad (5.14)$$

and similarly for the scalars in Fig. 20. In all cases, the relevant diagrams have been generated with the help of FEYNARTS 3 [49].

It is interesting to note that the boundary mass corrections can also be obtained by computing KK-number violating self-energy corrections. In this case, the bulk contribution is absent, and only one KK level contributes in the loop.

For instance, for the case of a vector boson, the KK-number violating  $V_n$ - $V_{n'}$  self-energy (with  $n' = n \pm 2$ ) can be written as [80]

$$\Pi_{\mu\nu}^{ab} = - \left[ \eta_{\mu\nu} p^2 \Pi_{\text{T}}^{(1)}(p^2) + \eta_{\mu\nu} \frac{1}{2} (n^2 + n'^2) \Pi_{\text{T}}^{(2)}(p^2) - p_\mu p_\nu \Pi_2(p^2) \right], \quad (5.15)$$

as a consequence of the 5D Lorentz symmetry. Thus from this self-energy one can extract  $\Pi_{\text{T}}^{(1)}$  and  $\Pi_{\text{T}}^{(2)}$  and then compute the KK-number conserving mass correction from (5.3).

We have explicitly checked that both approaches lead to the same results for the boundary mass corrections.

### 5.1.2 Results

In the following, results for the KK-mode mass corrections induced by boundary terms are presented for a general theory with an unspecified non-Abelian gauge interaction. The one-loop diagrams contributing to the masses of KK gauge bosons, KK scalars and KK fermions are shown in Figs. 19, 20, and 21, respectively.

The mass corrections obtained with the methods described in the previous section read as follows. As before, we use the abbreviation  $L_n \equiv \ln(\Lambda^2/m_n^2)$ .

$$\bar{\delta} m_{V_n}^2 = m_n^2 \frac{g^2}{32\pi^2} \left[ C_A \left( \frac{23}{3} L_n + \frac{154}{9} \right) - \sum_{i \in \text{scalars}} (-1)^{P_i} T_f \left( \frac{1}{3} L_n - \frac{4}{9} \right) \right], \quad (5.16)$$

$$\bar{\delta} m_{S_{+n}}^2 = \bar{m}^2 + m_n^2 \frac{1}{32\pi^2} \left[ C_F g^2 (6L_n + 16) - \sum_{i \in \text{scalars}} (-1)^{P_i} \lambda_i (L_n + 1) \right], \quad (5.17)$$

$$\bar{\delta} m_{f_n} = m_n \frac{1}{64\pi^2} \left[ C_F g^2 (9L_n + 16) - \sum_{i \in \text{scalars}} (-1)^{P_i} h_i^2 (L_n + 2) \right]. \quad (5.18)$$

Here  $m_{V_n}$  denotes the mass of the  $n$ -th KK excitations of a generic gauge boson, where  $C_A$  is the quadratic Casimir invariants of the adjoint representation. Similarly,  $m_{f_n}$  and  $m_{S_{+n}}$  are the masses of a KK-fermion and  $\mathbb{Z}_2$ -even KK-scalar, respectively, in the representation  $r$

with quadratic Casimir  $C_F$ . In a  $SU(N)$  theory one has  $C_A = N$  and  $C_F = (N^2 - 1)/(2N)$  for the fundamental representation. The sums run over the different scalar fields in the theory, with  $\mathbb{Z}_2$ -parity  $P_i$ , Dynkin index  $T_f$ , Yukawa coupling  $h_i$ , and scalar 4-point coupling  $\lambda_i^\dagger$ . Note that the two components of a complex scalar field need to be counted separately in the sum. As already pointed out in Ref. [80], fermion loops do not contribute to the self-energy boundary terms of gauge bosons and scalars, due to a cancellation between  $\mathbb{Z}_2$ -even and -odd fermion components.

A  $\mathbb{Z}_2$ -even scalar can also receive power-divergent contributions, which can be written as a boundary mass term [80]

$$\mathcal{L} \supset -\frac{\pi R}{2} [\delta(x^5) + \delta(x^5 + \pi R)] \bar{m}^2 \Phi^\dagger \Phi. \quad (5.19)$$

This term produces a mass correction of  $\bar{m}^2$  for the zero mode, while the higher KK masses are shifted by  $2\bar{m}^2$ . Thus, relative to the zero mode, the masses of the KK excitations receive a correction of  $\bar{m}^2$ , see eq. (5.17). While naive dimensional analysis would suggest that  $\bar{m}^2 \sim \mathcal{O}(\Lambda^2)$ , this is not consistent with the presence of a light scalar in the spectrum, as is the case in the SM. Instead, to generate the SM as a low-energy effective theory, one has to assume that  $\bar{m}^2$  is tuned to  $\bar{m}^2 \ll R^{-2}$ .

The logarithmic parts  $\propto L_n$  in eqs. (5.16)–(5.18) can be compared to Ref. [80], but we find some discrepancies: The one-loop scalar mass corrections should be proportional to  $C_F$ , instead of  $T_f$  in Ref. [80], and the fermion mass contribution from Yukawa couplings is a factor 3 smaller than reported there<sup>‡</sup>.

As evident from the equations above, the non-logarithmic terms are smaller than the terms proportional to  $L_n \sim 4 \cdots 8$  (for  $n \sim \mathcal{O}(1)$ ) by at most a factor of a few. Thus their contribution is phenomenologically important.

The KK mass corrections in MUED can be determined by simply substituting the appropriate SM coupling constants and group theory factors in the formulae above. For the gauge bosons

---

<sup>†</sup>The convention for the normalization of these couplings is the same as in appendix A.2.

<sup>‡</sup>Specifically, the  $b_1$  terms in line (b) of Tab. III in Ref. [80] should have opposite signs.

this leads to

$$\bar{\delta}m_{G_n}^2 = m_n^2 \frac{g_3^2}{32\pi^2} \left( 23L_n + \frac{154}{3} \right), \quad (5.20)$$

$$\bar{\delta}m_{W_n}^2 = m_n^2 \frac{g_2^2}{32\pi^2} \left( 15L_n + \frac{104}{3} \right), \quad (5.21)$$

$$\bar{\delta}m_{B_n}^2 = m_n^2 \frac{g_1^2}{16\pi^2} \left( -\frac{1}{6}L_n + \frac{2}{9} \right), \quad (5.22)$$

while for the fermions one obtains

$$\bar{\delta}m_{Q_n} = m_n \frac{1}{16\pi^2} \left[ g_3^2 \left( 3L_n + \frac{16}{3} \right) + g_2^2 \left( \frac{27}{16}L_n + 3 \right) + g_1^2 \left( \frac{1}{16}L_n + \frac{1}{9} \right) \right], \quad (5.23)$$

$$\bar{\delta}m_{Q_{3n}} = m_n \frac{1}{16\pi^2} \left[ g_3^2 \left( 3L_n + \frac{16}{3} \right) + g_2^2 \left( \frac{27}{16}L_n + 3 \right) + g_1^2 \left( \frac{1}{16}L_n + \frac{1}{9} \right) - h_t^2 \left( \frac{1}{4}L_n + \frac{1}{2} \right) \right], \quad (5.24)$$

$$\bar{\delta}m_{u_n} = m_n \frac{1}{16\pi^2} \left[ g_3^2 \left( 3L_n + \frac{16}{3} \right) + g_1^2 \left( L_n + \frac{16}{9} \right) \right], \quad (5.25)$$

$$\bar{\delta}m_{t_n} = m_n \frac{1}{16\pi^2} \left[ g_3^2 \left( 3L_n + \frac{16}{3} \right) + g_1^2 \left( L_n + \frac{16}{9} \right) - h_t^2 \left( \frac{1}{2}L_n + 1 \right) \right], \quad (5.26)$$

$$\bar{\delta}m_{d_n} = m_n \frac{1}{16\pi^2} \left[ g_3^2 \left( 3L_n + \frac{16}{3} \right) + g_1^2 \left( \frac{1}{4}L_n + \frac{4}{9} \right) \right], \quad (5.27)$$

$$\bar{\delta}m_{L_n} = m_n \frac{1}{16\pi^2} \left[ g_2^2 \left( \frac{27}{16}L_n + 3 \right) + g_1^2 \left( \frac{9}{16}L_n + 1 \right) \right], \quad (5.28)$$

$$\bar{\delta}m_{e_n} = m_n \frac{1}{16\pi^2} g_1^2 \left( \frac{9}{4}L_n + 4 \right), \quad (5.29)$$

where  $Q_{3n}$  and  $t_n$  denote the third generations of the KK excitations of the left-handed and right-handed up-type quark fields, respectively. Finally, the mass correction to the KK Higgs boson reads

$$\bar{\delta}m_{H_n}^2 = \bar{m}_H^2 + m_n^2 \frac{1}{16\pi^2} \left[ g_2^2 \left( \frac{9}{4}L_n + 6 \right) + g_1^2 \left( \frac{3}{4}L_n + 2 \right) - \lambda_H(L_n + 1) \right]. \quad (5.30)$$

In the above expressions,  $g_{1,2,3}$  are the couplings of the SM  $U(1)_Y$ ,  $SU(2)_L$  and  $SU(3)_C$  gauge groups, respectively, while  $h_t$  is the top Yukawa coupling and  $\lambda_H$  the Higgs self-coupling.

The numerical impact of these corrections will be discussed in section 5.3.

## 5.2 KK-NUMBER VIOLATING INTERACTIONS

As is well-known, the Lorentz symmetry breaking from orbifolding leads to loop-induced boundary-localized interactions which can break KK number [80]. From a phenomenological point of view, 2–0–0 interactions between a level-2 KK mode and two zero modes are particularly interesting, since they can mediate single production and decay of a level-2 KK particle at colliders.

The logarithmically enhanced contributions,  $\propto \ln(\Lambda R)$ , to these vertices have been considered in Refs. [80, 95]. Here, the non-logarithmic contributions are also computed, which are important for two reasons. On one hand, they can be numerically of similar order as the  $\ln(\Lambda R)$  term and thus lead to sizable corrections of the known KK-number violating couplings. On the other hand, there are additional vertices that are UV-finite but non-zero. Since these do not contain any  $\ln(\Lambda R)$  terms, they have not been considered before, but they can lead to phenomenologically relevant new production and decay channels.

### 5.2.1 Approach

The calculation of the KK-number violating couplings can be relatively easily performed by directly computing the  $X_2$ – $Y_0$ – $Z_0$  vertices in the 4D compactified theory. Here  $X$ ,  $Y$  and  $Z$  stand for any MUED fields. Since all leading-order vertices in MUED do conserve KK-number, one needs to consider only level-1 KK modes inside the loop.

As before, the authors have used FEYNARTS 3 [49] for the amplitude generation, and FEYN-CALC [50] was employed for part of the Dirac and Lorentz algebra manipulations. Similar to the mass corrections discussed above, UV divergences have been renormalized in the  $\overline{\text{MS}}$  scheme with the scale choice  $\mu = \Lambda$ .

Throughout this chapter, unless mentioned otherwise, contributions from electroweak symmetry breaking (EWSB) have been neglected, since these are suppressed by powers of  $vR$ . In particular, mixing between the KK- $Z$  boson and KK photon or between the KK-top doublet and singlet has not been included for the particles running inside the loops.

## 5.2.2 Results

Let us begin by writing the results for a generic theory with arbitrary non-Abelian gauge group and an arbitrary number of fermionic and scalar matter fields. Detailed expressions for the specific field content and interactions of MUED are listed in Appendix C.

**5.2.2.1  $\bar{\psi}_0\text{-}\psi_0\text{-}V_2^\mu$  coupling:** This vertex can be written in the form

$$-iC_{\psi_0\psi_0V_2}\gamma^\mu T^a P_\pm. \quad (5.31)$$

Here  $P_\pm$  are right-/left-handed projectors and  $T^a$  are the generators of the gauge group. For a U(1) group (such as U(1)<sub>Y</sub>),  $T^a$  is simply replaced by the charge (hypercharge  $Y$ ). The coefficient  $C_{\psi_0\psi_0V_2}$  receives contributions from the vertex and self-energy corrections shown in Fig. 23 and reads

$$\begin{aligned} C_{\psi_0\psi_0V_2} = & \frac{\sqrt{2}g}{64\pi^2} \left[ g^2 C_A^V \left( \frac{23}{3}L_1 + \frac{157}{9} - 2\pi^2 \right) + \sum_k g_k^2 C_F^k \left( -9L_1 - 13 + \frac{7\pi^2}{4} \right) \right. \\ & + g^2 \sum_{i \in \text{scalars}} (-1)^{P_i} T_f^V \left( -\frac{1}{3}L_1 - \frac{2}{9} \right) \\ & \left. + \sum_{i \in \text{scalars}} (-1)^{P_i} h_i^2 \left( L_1 - 1 + \frac{\pi^2}{4} + 2 \frac{C_{\phi_{i0}\phi_{i0}V_0}}{C_{\psi_0\psi_0V_0}} \right) \right], \quad (5.32) \end{aligned}$$

where  $C_A^V$  is the adjoint Casimir of the gauge group of  $V$ , which has the gauge coupling  $g$ , and  $T_f^V$  is the Dynkin index for the representation of the scalar  $i$  under the same group. The sum  $\sum_k$  runs over all gauge groups under which  $\psi$  is charged, with gauge couplings  $g_k$ , and  $C_F^k$  being the Casimir of the representation of  $\psi$  with respect to the gauge group  $k$ . For U(1) groups,  $T_f$  and  $C_F^k$  get replaced by the corresponding charges.  $h_i$  is the Yukawa coupling between scalar  $i$  and  $\psi$ .

Finally, eq. (5.32) depends also on  $C_{\phi_{i0}\phi_{i0}V_0}/C_{\psi_0\psi_0V_0}$ , the ratio of the couplings of the scalar  $i$  and the fermion  $\psi$  to the gauge field  $V$ . Some care must be taken when defining the signs of these couplings. The signs of the ratio should be +1 (−1) if  $\psi_0$  and  $\phi_{i0}$  have the same representation or the same charge sign for the gauge group of  $V$ , and they run in opposite directions (the same direction) in Fig. 23.

The logarithmic part of the first two lines in eq. (5.32) agrees with Ref. [80]. The logarithmic part of the last line in eq. (5.32) has been computed in Ref. [95] for a U(1) group, but we obtain a different result.

**5.2.2.2  $\bar{\psi}_2\text{-}\psi_0\text{-}V_0^\mu$  coupling:** There are two form factors that can facilitate the single production and decay of a level-2 KK-quark. The first is a Dirac-type chiral interaction,

$$-iC_{\psi_2\psi_0V_0}\gamma^\mu T^a P_\pm, \quad (5.33)$$

whereas the second is a dipole-like interaction,

$$-\tilde{D}_{\psi_2\psi_0V_0}\frac{\sigma^{\mu\nu}q_\nu}{2m_{KK}}T^a P_\pm, \quad (5.34)$$

where  $q$  is the momentum  $V_0^\mu$ . Note that by only considering these two expressions, we restrict ourselves to *transverse* polarization modes of the  $V_0^\mu$  boson. If  $V_0^\mu$  was a massive  $W$  or  $Z$  boson, their longitudinal modes must be excluded when using eq. (5.33), since they would receive contributions from an additional form factor proportional to  $(k_2 - k_0)^\mu$ , where  $k_2$  and  $k_0$  are the (incident) momenta of the  $\psi_2$  and  $\psi_0$  fermion, respectively. The restriction to transverse gauge boson polarizations is justified since the contribution of the longitudinal mode of  $W$  or  $Z$  bosons is suppressed by  $vR$ .

For the computation of the coefficient  $C_{\psi_2\psi_0V_0}$  one needs to consider the diagrams in Fig. 24, which yield

$$C_{\psi_2\psi_0V_0} = \frac{\sqrt{2}g}{64\pi^2} \left[ g^2 C_A^V \left( \frac{\pi^2}{4} L_1 - 2 \right) + 4 \sum_k g_k^2 C_F^k \right]. \quad (5.35)$$

The dipole-like interaction in eq. (5.34) is generated only by the vertex diagrams in Fig. 24 (A).

The result reads

$$\begin{aligned} D_{\psi_2\psi_0V_0} = & \frac{\sqrt{2}g}{64\pi^2} \left[ g^2 C_A^V (\pi^2 - 7) + \sum_k g_k^2 C_F^k \left( 3 - \frac{3\pi^2}{4} \right) \right. \\ & \left. + \sum_{i \in \text{scalars}} (-1)^{P_i} h_i^2 \left( \frac{\pi^2}{4} - 1 + \frac{\pi^2 - 8}{2} \frac{C_{\phi_{i0}\phi_{i0}V_0}}{C_{\psi_0\psi_0V_0}} \right) \right]. \quad (5.36) \end{aligned}$$

As evident from these expressions, both  $C_{\psi_2\psi_0V_0}$  and  $\tilde{D}_{\psi_2\psi_0V_0}$  are independent of  $\ln(\Lambda R)$ , and have not been previously reported in the literature.

**5.2.2.3  $V_2^{\mu,a}(p)-V_0^{\nu,b}(k_1)-V_0^{\rho,c}(k_2)$  coupling:** Restricting ourselves, as before, to transverse polarizations for  $V_0^{\nu,b}(k_1)$  and  $V_0^{\rho,c}(k_2)$ , this coupling can be written in the form

$$f_{abc} \left\{ \left[ \eta_{\mu\nu}(p-k_1)_\rho + \eta_{\nu\rho}(k_1-k_2)_\mu + \eta_{\rho\mu}(k_2-p)_\nu \right] C_{V_2V_0V_0} \right. \\ \left. + \left[ -\eta_{\mu\nu}k_{1,\rho} + \eta_{\rho\mu}k_{2,\nu} \right] D_{V_2V_0V_0} + \eta_{\nu\rho}(k_1-k_2)_\mu E_{V_2V_0V_0} \right\}. \quad (5.37)$$

Here  $f_{abc}$  are the structure constants of the gauge group. Furthermore,  $p$ ,  $k_1$  and  $k_2$  are the vector boson momenta, which are all taken to be incoming.

The coefficient  $C_{V_2V_0V_0}$  receives contributions from all diagrams in Fig. 25, whereas  $D_{V_2V_0V_0}$  and  $E_{V_2V_0V_0}$  are only generated by the first diagram in the figure. At one-loop level, they are given by

$$C_{V_2V_0V_0} = \frac{\sqrt{2}g^3}{64\pi^2} \left[ C_A^V \left( -\frac{157}{9} + \frac{7\pi^2}{6} \right) - \sum_{i \in \text{scalars}} (-1)^{P_i} T_f^V \left( \frac{4}{9} - \frac{\pi^2}{18} \right) \right], \quad (5.38)$$

$$D_{V_2V_0V_0} = \frac{\sqrt{2}g^3}{64\pi^2} \left[ C_A^V \left( \frac{91}{6} - \pi^2 \right) + \sum_{i \in \text{scalars}} (-1)^{P_i} T_f^V \frac{8 - \pi^2}{12} \right], \quad (5.39)$$

$$E_{V_2V_0V_0} = \frac{\sqrt{2}g^3}{64\pi^2} C_A^V \left( \frac{38}{3} - \frac{3\pi^2}{4} \right). \quad (5.40)$$

These results, which are also independent of  $\ln(\Lambda R)$ , are new.

**5.2.2.4  $\bar{T}_2-t_0-\Phi_0$  /  $\bar{t}_2-t_0/b_0-\Phi_0$  coupling:** Level-2 KK top quarks can have loop-induced decays into zero-mode top or bottom and Higgs states, which are proportional to the top Yukawa coupling. Here any component of the Higgs doublet can appear in the final state, including the Higgs bosons as well as longitudinal  $W$  and  $Z$  bosons. The result,

including strong and electroweak contributions, reads

$$\begin{aligned}\bar{t}_2 - t_0 - h_0 &: + i \frac{m_t}{v} P_- C_{t_2 t_0 \Phi_0}, \\ \bar{t}_2 - t_0 - Z_L &: - \frac{m_t}{v} P_- C_{t_2 t_0 \Phi_0},\end{aligned}\tag{5.41}$$

$$\begin{aligned}\bar{t}_2 - b_0 - W_L^+ &: - i \sqrt{2} \frac{m_t}{v} P_- C_{t_2 t_0 \Phi_0}, \\ C_{t_2 t_0 \Phi_0} &= \frac{\sqrt{2}}{64\pi^2} \left[ g_3^2 \left( \frac{8}{3} L_1 + \frac{40}{3} - \pi^2 \right) + g_2^2 \left( -3L - \frac{3}{2} + \frac{3\pi^2}{8} \right) \right. \\ &\quad \left. + g_1^2 \left( \frac{23}{9} L_1 + \frac{83}{18} - \frac{5\pi^2}{24} \right) - 2h_t^2 L_1 + \lambda \frac{3}{2} (L_1 + 1) \right],\end{aligned}\tag{5.42}$$

$$\begin{aligned}\bar{T}_2 - t_0 - h_0 &: - i \frac{m_t}{v} P_+ C_{T_2 t_0 \Phi_0}, \\ \bar{T}_2 - t_0 - Z_L &: - \frac{m_t}{v} P_+ C_{T_2 t_0 \Phi_0},\end{aligned}\tag{5.43}$$

$$\begin{aligned}C_{T_2 t_0 \Phi_0} &= \frac{\sqrt{2}}{64\pi^2} \left[ g_3^2 \left( \frac{8}{3} L_1 + \frac{40}{3} - \pi^2 \right) + g_2^2 \left( \frac{15}{4} L_1 + 9 - \frac{3\pi^2}{8} \right) \right. \\ &\quad \left. + g_1^2 \left( -\frac{43}{36} L_1 + \frac{1}{9} + \frac{\pi^2}{24} \right) - 2h_t^2 L_1 + \lambda \frac{3}{2} (L_1 + 1) \right].\end{aligned}\tag{5.44}$$

**5.2.2.5  $\Phi_2$  decay couplings:** The level-2 KK excitation of the SM Higgs doublet can be decomposed into a neutral CP-even component  $h_2$ , a neutral CP-odd component  $\chi_2$ , and a charged pair  $\phi_2^\pm$ ,

$$\Phi_2 = \begin{pmatrix} \phi_2^+ \\ \frac{1}{\sqrt{2}}(h_2 + i\chi_2) \end{pmatrix}.\tag{5.45}$$

They have a rich variety of loop-induced couplings to pairs of zero-mode particles. In this work we do not attempt a comprehensive discussion of these channels, but only present a few interesting aspects.

The leading decay channel of  $h_2$  and  $\chi_2$  is into  $t\bar{t}$  pairs, which is dominantly induced through QCD loops. The result is given by

$$\bar{t}_0 t_0 h_2 : \quad - i \frac{m_t}{v} C_{t_0 t_0 h_2},\tag{5.46}$$

$$\bar{t}_0 t_0 \chi_2 : \quad i \gamma_5 \frac{m_t}{v} C_{t_0 t_0 h_2},\tag{5.47}$$

$$C_{t_0 t_0 h_2} = \frac{\sqrt{2} g_3^2}{64\pi^2} C_F \left[ -4L_1 - 4 + \frac{\pi^2}{2} \right].\tag{5.48}$$

The logarithmic part of this expression agrees with Ref. [95].

$h_2$  does not have any decays into gluon pairs since there is a cancellation between the  $\mathbb{Z}_2$ -even and  $\mathbb{Z}_2$ -odd KK-tops inside the vertex loop. However, it can couple to electroweak gauge boson pairs via loops involving level-1 KK-gauge and KK-Higgs bosons, although this effective interaction is suppressed by  $vR$ . Nevertheless, this subdominant decay channel is still interesting since it can lead to di-photon resonance signals. We find that it can be written as

$$\mathcal{L}_{h_2 V_0 V_0} \supset \sum_{j,k=0}^3 \frac{iC_{jk} v R^2}{64\sqrt{2}\pi^2} h_2 F_{0,\mu\nu}^j F_0^{k,\mu\nu}, \quad (5.49)$$

where the  $j, k = 0$  refers to the U(1) field  $B_0^\mu$  and  $j, k = 1, 2, 3$  to the SU(2) gauge boson  $W_0^{a,\mu}$ . The coefficient  $C_{jk}$  are given by

$$C_{00} = \frac{g_1^2}{128} [g_1^2(8\pi^2 - 58) + 24g_2^2(\pi^2 - 10) + 48\lambda(2\pi^2 - 27) + 3(41g_1^2 + 93g_2^2 - 120\lambda)L_1], \quad (5.50)$$

$$C_{jj} = -\frac{g_2^2}{128} [g_1^2(122 - 8\pi^2) + 24\lambda(54 - 4\pi^2) + 24g_2^2(10 + 3\pi^2) - 15(5g_1^2 + 41g_2^2 - 24\lambda)L_1], \quad [j = 1, 2, 3] \quad (5.51)$$

$$C_{03} = -\frac{g_1 g_2}{128} [2g_1^2(2\pi^2 - 65) - 8\lambda(17 - 2\pi^2) + 8g_2^2(35 + 3\pi^2) + 3(5g_1^2 + 81g_2^2)L_1], \quad (5.52)$$

$$C_{01} = C_{02} = C_{12} = C_{13} = C_{23} = 0. \quad (5.53)$$

In contrast to the CP-even component, the CP-odd  $\chi_2$  can have a loop-induced coupling to gluon pairs. The  $g_{0,\mu}^a(k_1)g_{0,\nu}^a(k_2)\chi_2$  has the form

$$\frac{-i}{v} C_{g_0 g_0 \chi_2} \epsilon^{\mu\nu k_1 k_2}, \quad C_{g_0 g_0 \chi_2} = \frac{\sqrt{2}g_3^2}{64} m_t R^2. \quad (5.54)$$

As for the  $h_2$  decay into vector bosons, it is suppressed by  $vR$ , but may still be relevant for the production of  $\chi_2$  at hadron colliders.

### 5.3 PHENOMENOLOGICAL IMPLICATIONS

In this section, we study the mass spectrum of KK particles with improved one-loop corrections, including finite (non-logarithmic) terms, and their decays and collider implications of KK-number violating interactions.

#### 5.3.1 Mass Hierarchy

We begin our discussion with the mass spectrum of KK particles at level-1, which is shown in Fig. 26 for  $R^{-1} = 1$  TeV and  $\Lambda R = 20$  without (left) and with (right) finite contributions, respectively. KK bosons (either spin-0 or spin-1) are shown in the left column, while KK fermions are in the middle (for first two generations) and right column (for third generation). In general is the mass spectrum slightly broadened by the finite corrections. For example, the mass splitting  $\delta = \frac{m_{Q_1} - m_{\gamma_1}}{m_{\gamma_1}}$  between KK quark ( $Q_1$ ) and KK photon ( $\gamma_1$ ) increases from  $\sim 20\%$  to  $\sim 25\%$  (for  $\Lambda R = 20$ ), making the decay products harder in the cascade decays. Since they become slightly heavier for a given value of  $R^{-1}$ , their production cross sections of KK quarks would decrease slightly. Therefore it is worth investigating the implications of finite terms to see which effect between the increased efficiency and the reduced production cross section would make a more pronounced difference. The dependence on  $\Lambda R$  is logarithmic and we observe similar patterns in the mass hierarchy for a wide range in  $(R^{-1}, \Lambda R)$  space, with the exception of the KK Higgs and KK leptons. The KK Higgs bosons masses (magenta in the left column) are highly degenerate with the  $SU(2)_L$ -singlet KK lepton masses ( $e_1$ , red in the middle column), as shown in the left panel of Fig. 26, but finite corrections increase the mass difference between the two, as shown in the right panel. In particular, this can affect the hierarchy of the lightest and next-to-lightest level-1 KK particles, abbreviated as LKP and NLKP, respectively. The (LKP, NLKP) structure has been studied in detail in Ref. [96], and we reproduce some of their findings as shown in the left panel of Fig. 27. For a given value of  $\Lambda R$ , the NLKP is the  $SU(2)_L$ -singlet KK lepton if  $R^{-1} < R_o^{-1}$ , while the NLKP is the charged KK Higgs for  $R^{-1} > R_o^{-1}$ , where  $R_o^{-1}$  is determined by  $m_{H_1^\pm}(R_o^{-1}, \Lambda R) = m_{e_1^R}(R_o^{-1}, \Lambda R)$ . The red curve in the left panel of Fig. 27

is the solution of this equation. To study this in detail, we plot the mass difference between them as a function of  $R^{-1}$  for  $\Lambda R = 20$ . The corresponding result (red, solid) is labeled as (a) in the right panel of Fig. 27. Fixing a typo in the Higgs mass correction of Ref. [80] ( $\frac{3}{2}$  should be  $\frac{9}{4}$ , as already mentioned in section 5.1.2), we obtain the (blue, dashed) curve, labeled as (b). With this correction, KK leptons are always the NLKP, in contrast to what is shown in the left panel. Including the finite terms in eq. (5.30), we find an even larger mass splitting, shown by the (green, dotted) curve (labeled as (c)). This could have some impact on the computation of the KK-photon relic abundance, since co-annihilation processes are important in this degenerate mass spectrum [95]. Finally, we revisit the mass eigenstates of the KK photon and KK  $Z$  boson. In the weak eigenstate basis, the mass matrix is found to be

$$\begin{pmatrix} \frac{n^2}{R^2} + \hat{\delta}m_{B_n}^2 + \frac{1}{4}g_1^2v^2 & \frac{1}{4}g_1g_2v^2 \\ \frac{1}{4}g_1g_2v^2 & \frac{n^2}{R^2} + \hat{\delta}m_{W_n}^2 + \frac{1}{4}g_2^2v^2 \end{pmatrix}, \quad (5.55)$$

where  $\hat{\delta}$  is the total one-loop correction, including both bulk and boundary contributions.

In Fig. 28, we show the dependence of the Weinberg mixing angle  $\theta_n$  on  $R^{-1}$  for the first five KK levels ( $n = 1, \dots, 5$ ) for  $\Lambda R = 20$ , without (left) and with (right) finite contributions respectively. As shown in the plots, the Weinberg angles are further suppressed by the finite terms,  $\frac{\sin^2 \theta_n^{\text{new}}}{\sin^2 \theta_n^{\text{old}}} \lesssim 0.55$  for large  $R^{-1}$ . Their dependence on  $\Lambda R$  is weak and similar to that in Ref. [80].

### 5.3.2 Branching Ratios of Level-2 KK Excitations

The decay channels of level-1 KK particles are the same as before. Although there are minor numerical changes due to the change in mass spectrum, including finite terms, the main branching fractions remain the same as those in Ref. [83]. In this section, we focus on the branching fractions of level-2 KK particles.

Unlike the decay of  $n = 1$  KK particles, which always give rise to an invisible stable KK particle in the decay,  $n = 2$  decays do not necessarily produce such missing-particle signatures. In fact, there are three decay channels of level-2 KK particles: (i) decay to two  $n = 0$  modes (denoted as 200), (ii) decay to two  $n = 1$  modes (211), and (iii) decay to one  $n = 2$  and one  $n = 0$  modes (220). Both the 220 and the 211 channels are phase space suppressed,

since KK particles are more or less degenerate around  $m_n \sim n/R$ , while 200 decays are suppressed by one loop. Therefore branching fractions of  $n = 2$  KK particles are sensitive to details of the coupling structure and mass spectrum, which illustrates the importance of computing the finite corrections. In the case of the 211 decay channel, each level-1 KK particle would then proceed through its own cascade decay and give one missing particle at the end. Therefore single production of a level-2 KK particle followed by a 211 decay gives two missing particles, while pair production of level-2 KK particles plus their subsequent 211 decay gives four missing particles at the end of their cascade decays. On the other hand, a KK particle that decays via a 200 channel will appear as a resonance, if both SM particles can be reconstructed.

**5.3.2.1  $\psi_2$  Decays** We first consider the branching fractions of level-2 KK fermions, which are shown in Figs. 29 and 30 for KK quarks and KK leptons, respectively. The branching fractions for  $SU(2)_L$ -doublet KK fermions are shown in the left panel, while those for  $SU(2)_L$ -singlet KK fermions are on the right. In Fig. 29 and the right panel of Fig. 30, results with finite corrections are shown in solid curves, whereas previous results from Ref. [97] are shown in dotted curves. While one observes no significant changes in existing decay channels, there are new ones based on our findings as explained in the previous section.  $SU(2)_L$  KK leptons have the new  $\nu W^-$ ,  $\ell Z$ , and  $\ell \gamma$  channels, which contribute with 0.1% to 2%, while the branching fraction of  $u_2$  to  $ug$  is as big as 2.5%. In the case of KK lepton decays, EWSB effects are important, *i.e.* a sizable mixing between KK photon and KK  $Z$  is expected for low values of  $R^{-1}$  (see eq. 5.55). It turns out that  $m_{\ell_2} - m_{\gamma_1} - m_{\ell_1}$  approaches 0 as  $R^{-1} \rightarrow v$ , which is why the  $\ell \gamma_2$  branching fraction becomes larger. This effect is more pronounced for the  $SU(2)_L$  singlet lepton. This pattern does not appear for KK quarks, since mass corrections to KK quarks are larger than those to KK gauge bosons (see Fig. 30).

Branching fractions of  $SU(2)_L$  doublet quarks are rather complicated as shown in the left panel of Fig. 30. New decay channels  $dW$ ,  $ug$  and  $uZ$ , show branching fractions of 2.5–4.5%, 1.5–2.5% and 1–2%, respectively.

Branching fractions for neutral KK leptons and the down-type KK quarks are similar. For example, looking at the  $d_2$  decay we find the  $d \gamma_2$  and  $d_1 \gamma_1$  channels to be dominant with BR

$\sim 45\%$ , but the branching fraction into  $dg$  is slightly higher at about 8%. This is due to the different hypercharge couplings between the up-type and the down-type quarks. Branching fractions into  $dZ$  and  $d\gamma$  are negligible as before.

Finally we show the branching fractions of level-2 KK top quarks in Fig. 31. In this case we find that the branching fractions of the  $SU(2)_L$  doublet KK top into  $th$  or  $tZ$  are 3–6% each. Other 200 decay modes into  $tg$  and  $bW^+$  show branching fractions of about 2–4% and 1–2%, respectively. The  $t\gamma$  branching fraction is below one percent, which implies that the KK top decays directly to two SM particles  $\sim 8$ –15% of the time. The  $SU(2)_L$  singlet KK top does not have decays to  $SU(2)_L$  gauge bosons, and branching fractions for  $th$  and  $tg$  are of order 1–5.5% and 2–12%, respectively, for  $250 \text{ GeV} < R^{-1} < 2 \text{ TeV}$ . Due to the Yukawa correction to the KK top mass, two-body decays of level-2 KK top into  $W_1^+ B_1$ ,  $t_1 Z_1$  and  $t\gamma_2$  are suppressed for low values of  $R^{-1}$ .

**5.3.2.2  $V_2$  Decays** Fig. 32 shows the branching fractions of  $n = 2$  KK gauge bosons as a function of  $R^{-1}$ . Overall, we find our results are similar to those in Ref. [97] with a few notable changes.

Firstly we considered the new decay channels  $g_2 \rightarrow gg$ ,  $Z_2 \rightarrow W^+W^-$ ,  $W_2^\pm \rightarrow ZW^\pm$  and  $W_2^\pm \rightarrow \gamma W^\pm$ . Their rather moderate branching fractions contribute with 1–2%, 0.3%, 2–3%, and 0.7%, respectively.

The leptonic branching fractions of  $Z_2$  and  $\gamma_2$  become smaller with finite corrections and are now about 0.7%.

Due to larger mass corrections for strongly interacting particles (KK-gluon and KK-quarks), only the  $n = 2$  KK gluon can decay to KK-quarks ( $qq_2$  or  $q_1q_1$ ), while two-body decays of KK  $Z$  and  $W$  gauge bosons into KK quarks are kinematically closed. With finite corrections and additional decay channels, the total decay widths of level-2 bosons increase by a factor of  $\sim 2$  for electroweak gauge bosons and  $\sim 5$  for KK gluon as shown in Fig. 33. However, their decay widths are still very small due to the phase space suppression of 220 and 211 decays and loop-suppression of 200 decays, as mentioned at the beginning. For electroweak gauge bosons,  $\Gamma_{V_2}/m_{V_2} \lesssim 10^{-3}$ , and  $\Gamma_{g_2}/m_{g_2} \sim 0.02$  for KK gluons.

**5.3.2.3 Cross Sections and Signatures** Single production of level-1 KK particles is forbidden due to KK-parity and therefore they must be produced in pairs from collisions of two SM particles or from the decay of level-2 KK particles. However, both single and pair productions are possible for level-2 KK particles. Single production cross sections are suppressed by a loop factor, while pair production cross sections are suppressed by phase space.

All cross sections are calculated at tree level considering five partonic quark flavors in the proton along with the gluon at the 14 TeV LHC. We sum over the final state quark flavors and include charge-conjugated contributions. We used CTEQ6L parton distributions [57] and chose the scale of the strong coupling constant to be equal to the parton-level center-of-mass energy. All results are obtained using CALCHEP [98] based on the implementation of the MUED model from Ref. [26]. Since the particle content and KK number conserving interactions remain the same, we only modified the KK mass spectrum and KK number violating interactions in the existing implementation which is based on Ref. [80]. We also implemented the new interactions which are described throughout this chapter.

We summarize single production cross sections of  $n = 2$  KK gauge bosons (left) and  $n = 2$  KK quarks (right) in Fig. 34. While overall one observes a slight increase in production cross sections for the KK-gauge bosons, the  $gg \rightarrow g_2$  production channel has been computed for the first time here and contributes at a sizable level. All KK-fermion single production cross sections presented here had also not been considered previously.

Fig. 35 shows the pair production of KK quarks (left) and associated production of KK quark and KK gluon (right), respectively.

Another interesting channel is associated production of KK top with SM top quark.  $pp \rightarrow T_2 \bar{t} + t \bar{T}_2$  is shown as a (black, solid) curve, labeled as ‘ $T_2 t_0$ ’ in the left panel of Fig. 35. Since  $T_2$  has a large branching fraction into  $th$  and a sizable branching fraction into  $t\gamma$ ,  $bW$  or  $tZ$ , this production could be constrained by cross section measurements of SM processes such as  $t\bar{t}\gamma$ ,  $t\bar{t}$ ,  $t\bar{t}h$  and  $t\bar{t}$ .

Finally, we plot the total integrated luminosity  $\mathcal{L}$  (in  $\text{fb}^{-1}$ ) required for a  $5\sigma$  excess of signal over background in the di-electron (red, dotted) or di-muon (blue, dashed) channel, as a function of  $R^{-1}$  (in GeV). We have used the same backgrounds, basic cuts and detector

resolutions as described in Ref. [97]. In each panel of Fig. 36, the upper set of lines labeled ‘DY’ only utilizes the single  $V_2$  productions from Fig. 34. The lower set of lines (labeled ‘All processes’) includes in addition indirect  $\gamma_2$  and  $Z_2$  production from the cascade decays of level-2 KK quarks to level-2 KK gauge bosons from Fig. 35. We do not include contributions from single production of level-2 KK quarks, so as to compare more directly against results in Ref. [97]. They would make a small contribution to the total luminosity as shown in the right panel of Fig. 34.

For both di-electron and di-muon channel, we observe no significant change in the required luminosity compared to results from Ref. [97], although we notice a slight reduction or increase in the luminosity, depending on the value of  $R^{-1}$ . This is due to the interplay between improved results on cross sections and branching fractions. Overall, production cross sections are increased as shown in Figs. 34 and 35, while branching fractions decrease as shown Fig. 32. The high-luminosity LHC with  $3 \text{ ab}^{-1}$  would be able to probe the level-2 KK photon up to  $R^{-1} \sim 1.2 \text{ TeV}$  in the  $\mu^+\mu^-$  and  $R^{-1} \sim 1.5 \text{ TeV}$  in the  $e^+e^-$  channel. The corresponding reach for the level-2 KK  $Z$  boson is lower due to the relevant branching fractions.

## 5.4 SUMMARY AND CONCLUSIONS

In this article we presented the one-loop corrected mass spectrum and KK-number violating decays of level-2 KK states into SM particles in models with universal extra dimensions. As a concrete framework we chose to add one additional universal extra dimension to the SM, which is compactified on a circle with a  $\mathbb{Z}_2$  orbifold. Due to its non-renormalizability the model is regarded as an effective low-energy theory with a hard cutoff scale  $\Lambda$  at which an unspecified UV-completion is expected to describe the physics. This enables us to write down sensible  $\overline{\text{MS}}$  counterterms with a logarithmic sensitivity to the cutoff. All calculations were performed in the 4D effective theory using publicly available software supplemented by in-house routines.

The self energy diagrams giving rise to the mass corrections contain an infinite tower of states

in the loop, whose summation requires additional regularization. To this end we employed the Poisson summation identity to identify the divergent pieces in winding number space and remove them. The results can be divided into logarithmically divergent boundary terms and finite bulk contributions.

The low cutoff scale ( $\Lambda R \lesssim 50$ , considering perturbativity and unitarity [18, 22]) implies that the leading (logarithmic) terms in the one-loop corrections to KK masses are not as large as those in supersymmetry, and finite contributions could play an important role phenomenologically.

When including the new finite (non-logarithmic) corrections, the mass spectrum broadens and each KK particle becomes heavier, which implies that the pair production cross sections of level-1 KK particles at colliders would be reduced but their acceptance rate would increase. We also examined the nature of the NLKP, and confirmed that it is always the right-handed KK lepton, which is different from what has been stated in the literature, where the NLKP was thought to be the KK-Higgs for a large KK scale. The KK Weinberg angles are further reduced such that weak eigenstates are basically mass eigenstates.

Using the same methodology, we have calculated finite corrections to the decays of level-2 KK states into SM particles, including previously unknown couplings. Since the interactions violate KK number, only a finite number of diagrams contribute to the vertices and no additional regularization is necessary. We then revisited the computation of branching fractions for level-2 KK particles. For KK fermions the basic features remain the same as before with the addition of new decay modes opening up at the few-percent level. The largest effects appear in the decay of level-2 KK top quarks, *i.e.*, the branching fraction of the left-handed KK top quark into  $th$  is about 20–30%. Branching fractions of level-2 gauge bosons are also updated. Overall, the decay widths of level-2 particles are observed to increase when these effects are included, but they are still narrower than the detector resolution.

Finally, we would like to make a few comments about other potentially interesting collider and dark matter phenomenology. In this chapter, we showed results for the production of level-2 KK gauge bosons at the LHC. It is desirable to study these with a more detailed simulation, including single and pair production of level-2 KK fermions, and set bounds on  $(R^{-1}, \Lambda R)$  from various resonance searches, such as  $V_2$  decays to  $\ell\bar{\ell}$ ,  $jj$ ,  $W^+W^-$ ,  $W^\pm Z$ ,  $ZZ$ ,

$t\bar{t}$ . Here one can make use of boosted  $W$ ,  $Z$  and  $t$  event topologies.

The collider phenomenology of singly produced level-2 KK fermions provides interesting signatures. For instance, searches for excited quarks in various final states would constrain level-2 decays such as  $pp \rightarrow Q_2/q_2 \rightarrow q'V$ , where  $V = \gamma, Z, W$  or  $g$ .  $Q_2$  or  $q_2$  could appear as a single three-jet resonance via  $q'V_2$  with  $V_2 \rightarrow f_0f'_0$ .

Other interesting topologies involve the top quark and the Higgs. They may not provide the best sensitivity in a search for this particular model since certain signal-to-background ratios may be small. However they could serve as a benchmark model for various searches and provide useful search grounds. We list a few examples below.

- $pp \rightarrow t_2\bar{t}_2$  with  $t_2 \rightarrow th, t_2 \rightarrow tg$  or  $t_2 \rightarrow t\gamma$
- $pp \rightarrow T_2\bar{T}_2$  with  $T_2 \rightarrow th, T_2 \rightarrow Zt, T \rightarrow tg, T \rightarrow t\gamma$  or  $T_2 \rightarrow t\gamma_2$  ( $\gamma_2 \rightarrow t\bar{t}$ )
- $pp \rightarrow B_2\bar{B}_2$  with  $B_2 \rightarrow Zb$  or  $B_2 \rightarrow Wt$  (and small branching fractions to  $B_2 \rightarrow gb, B_2 \rightarrow b\gamma$ )
- $pp \rightarrow b_2\bar{b}_2$  with  $b_2 \rightarrow gb$  (and small branching fractions to  $b_2 \rightarrow \gamma b$ , and  $b_2 \rightarrow Zb$ )
- $pp \rightarrow Q_2, q_2, Q_2\bar{Q}_2, q_2\bar{q}_2$  (both single and pair production) with  $Q_2 \rightarrow qg$  or  $Q_2 \rightarrow q\gamma$
- $T_2\bar{T}_2 \rightarrow t\bar{t}h + X$  (inclusive  $t\bar{t}h$  production)

As discussed earlier, level-1 KK particles are always produced in pairs due to KK parity and lead to signals with missing transverse momentum. Final states with jets + leptons + missing transverse momentum are known to provide stringent bounds on  $R^{-1}$  (see Ref. [23]). It is worth revisiting these analyses with our improved mass spectrum, since the broader mass pattern will lead to signal efficiency gains while at the same time the increased masses will reduce the production cross sections.

The computation of the relic abundance of KK dark matter has a rather long history [21, 82, 95]. Ref. [95] includes both coannihilation and resonance effects, which play a crucial role in increasing the preferred mass scale of the KK photon. Our results imply that a slightly broader mass spectrum would reduce effective cross sections in the coannihilation processes (which are suppressed by  $\frac{e^{-x'_f(m'_1 - m'_{\gamma_1})}}{e^{-x_f(m_1 - m_{\gamma_1})}} \approx e^{-x_f(m'_1 - m_1)}$  where  $x_f \approx x'_f$  is the freeze-out temperature and  $m_1$  is the mass of the coannihilating particle,  $m'_1$  is the improved mass, and  $m_{\gamma_1} \approx m'_{\gamma_1}$  is the mass of KK photon), pushing  $m_{\gamma_1}$  to a lower value. However,  $11 \rightarrow 20$

processes with the level-2 particle decaying to two zero modes would increase the effective annihilation cross section efficiently, increasing the preferred value for  $m_{\gamma_1}$ . This is a highly non-trivial and complicated exercise and we postpone it to a follow-up study.

We hope that our results will be useful for investigations of the phenomenology of universal extra dimensions and also provide interesting event topologies for various collider searches [86].

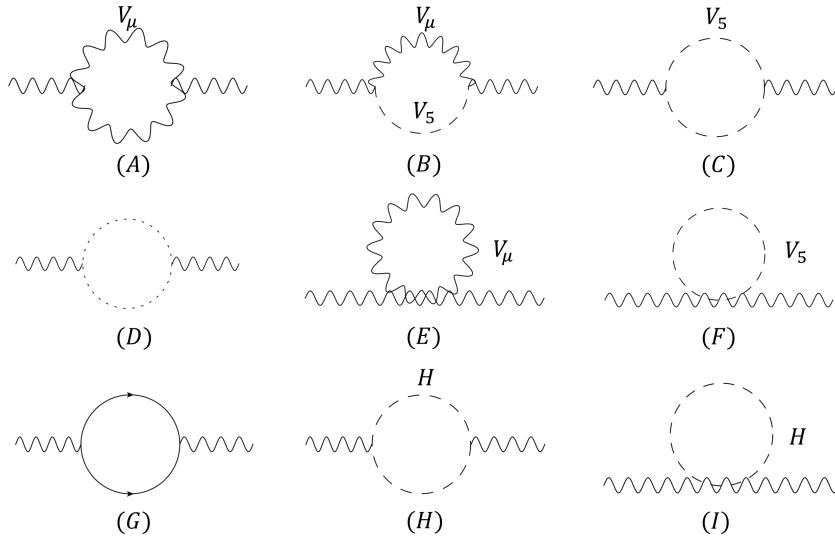


Figure 19: *Generic Feynman diagrams for the one-loop contributions to the self-energies of KK vector bosons. Here wavy, dashed, dotted and solid lines indicate the KK modes of vector bosons, scalars, ghosts and fermions, respectively.  $V_5$  denotes the scalar degree of freedom from the fifth component of a 5D gauge field, whereas  $H$  stands for the contribution from a genuine 5D scalar field.*

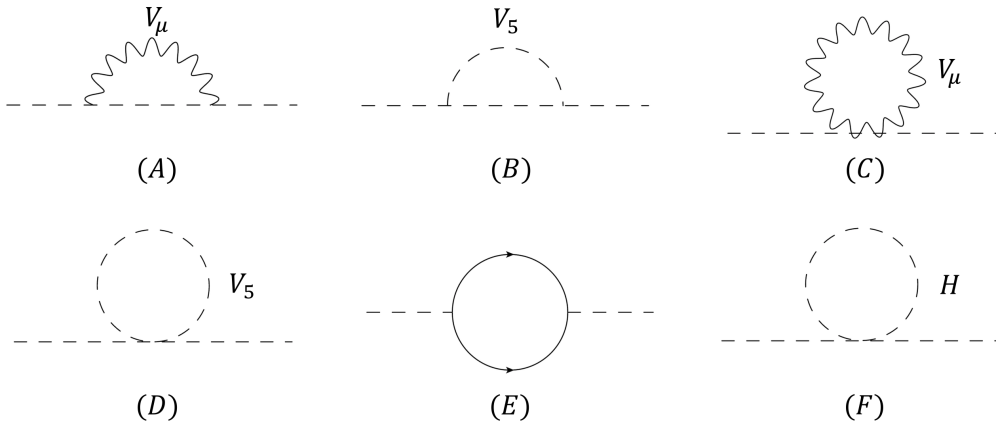


Figure 20: *Generic Feynman diagrams for the one-loop contributions to the self-energies of KK scalars. See caption of Fig. 19 for further explanations.*

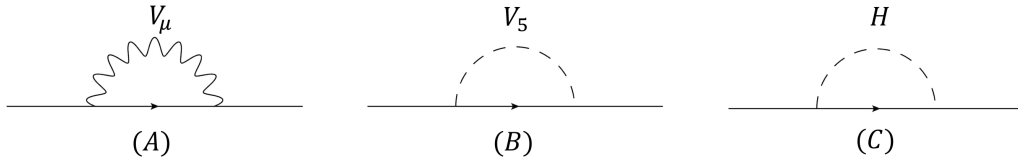


Figure 21: Generic Feynman diagrams for the one-loop contributions to the self-energy of KK fermions. See caption of Fig. 19 for further explanations.

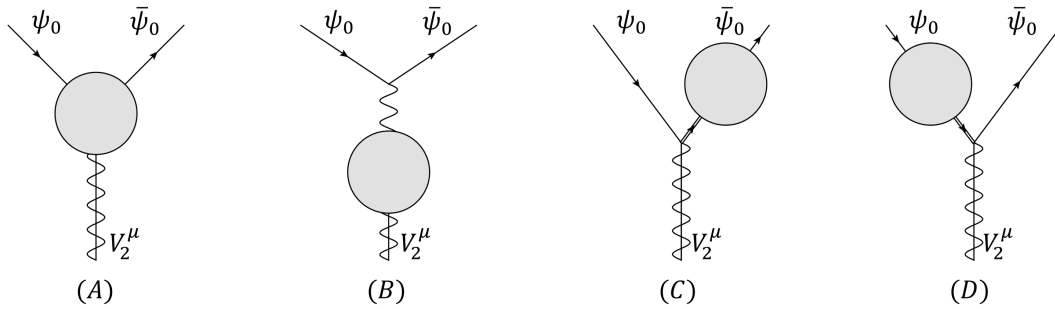


Figure 22: Contributions to the  $\bar{\psi}_0\text{-}\psi_0\text{-}V_2$  vertex, where the blobs indicate one-loop corrections. Zero-mode vector and fermion propagators are depicted through normal wavy and solid lines, respectively, whereas level-2 vector and fermion propagators are shown as wavy-solid and double-solid lines, respectively.

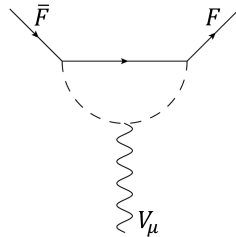


Figure 23: Vertex diagram contributing to KK-number violating vector-boson-fermion couplings involving a KK-Higgs in the loop.

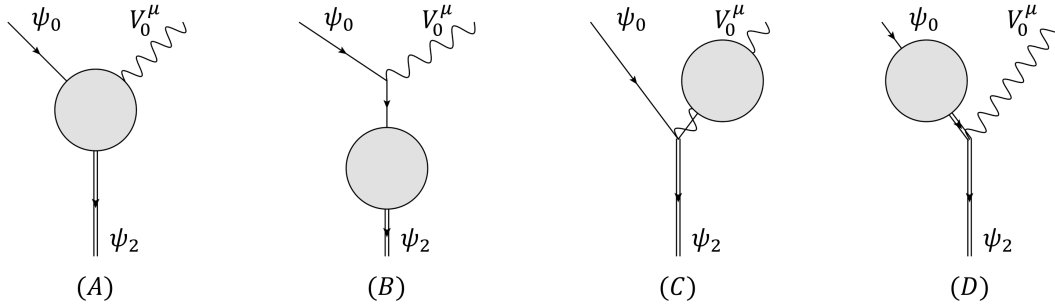


Figure 24: Contributions to the  $\bar{\psi}_2-\psi_0-V_0$  vertex. See caption of Fig. 23 for more explanations.

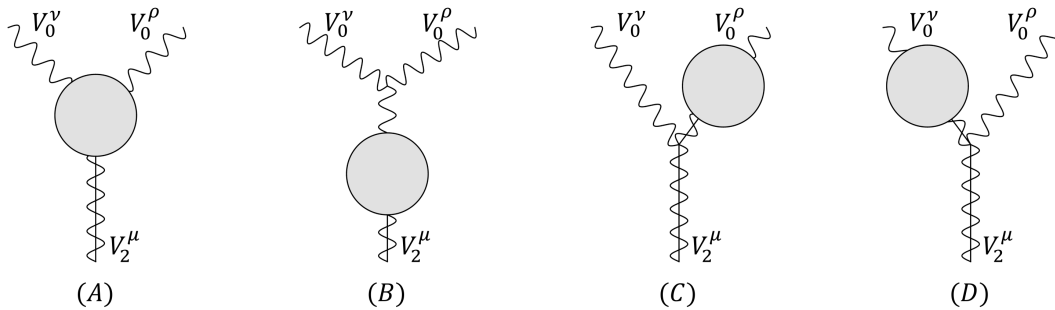


Figure 25: Contributions to the  $V_2-V_0-V_0$  vertex. See caption of Fig. 23 for more explanations.

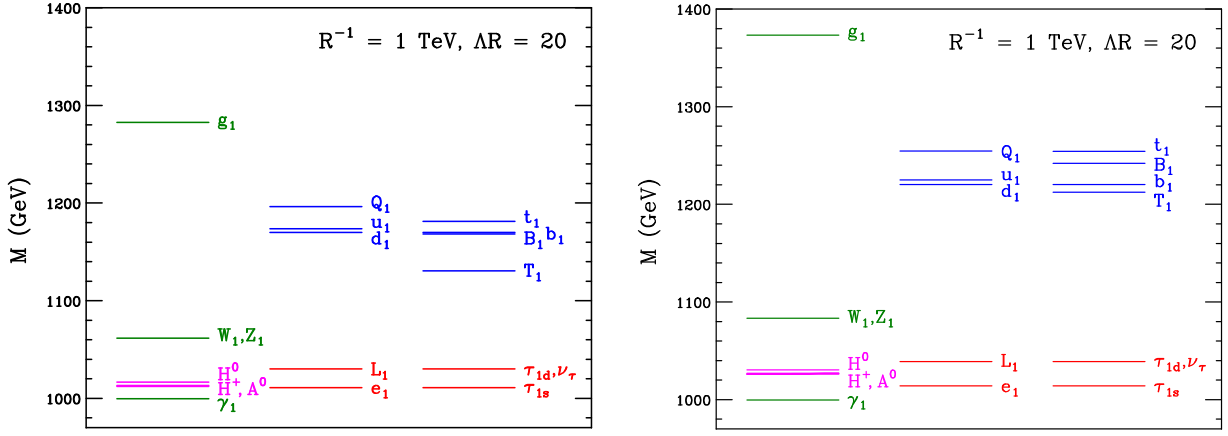


Figure 26: Mass spectrum of KK particles at level-1 for  $R^{-1} = 1$  TeV and  $\Lambda R = 20$  without (left) / with (right) finite contributions.

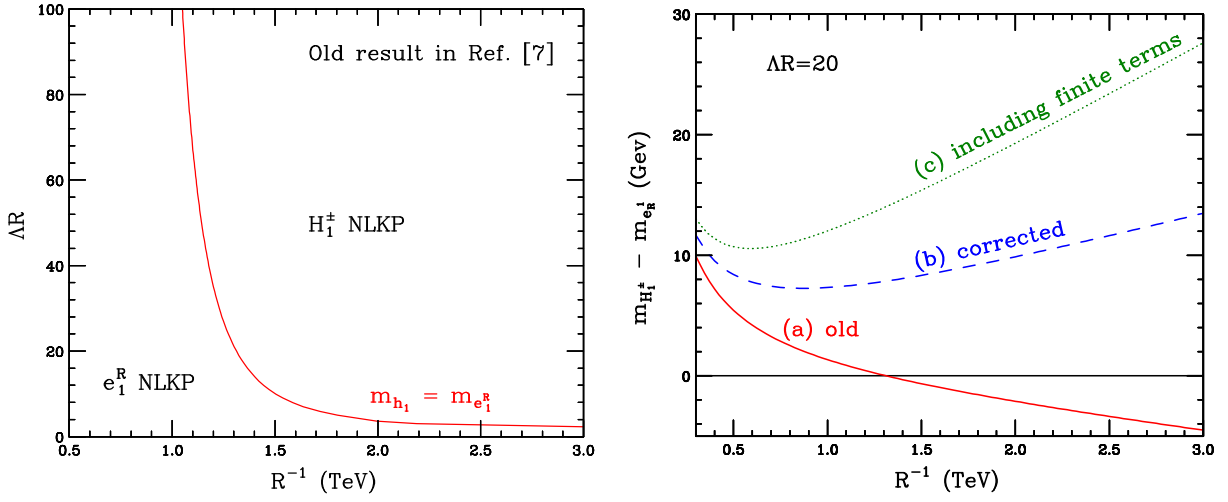


Figure 27: Left: The phase diagram in the  $(R^{-1}, \Lambda R)$  plane from Ref. [96] is reproduced using the incorrect numerical factor (see text), which shows that the KK Higgs could be the NLKP in MUED for a large value of  $R^{-1}$ . Right: Fixing  $\Lambda R = 20$ , the old (incorrect) result is shown in (red, solid) as a function of  $R^{-1}$ . The correct result is shown in (blue, dashed), while the curve in (green, dotted) includes finite terms. We find that KK leptons are always the NLKP.

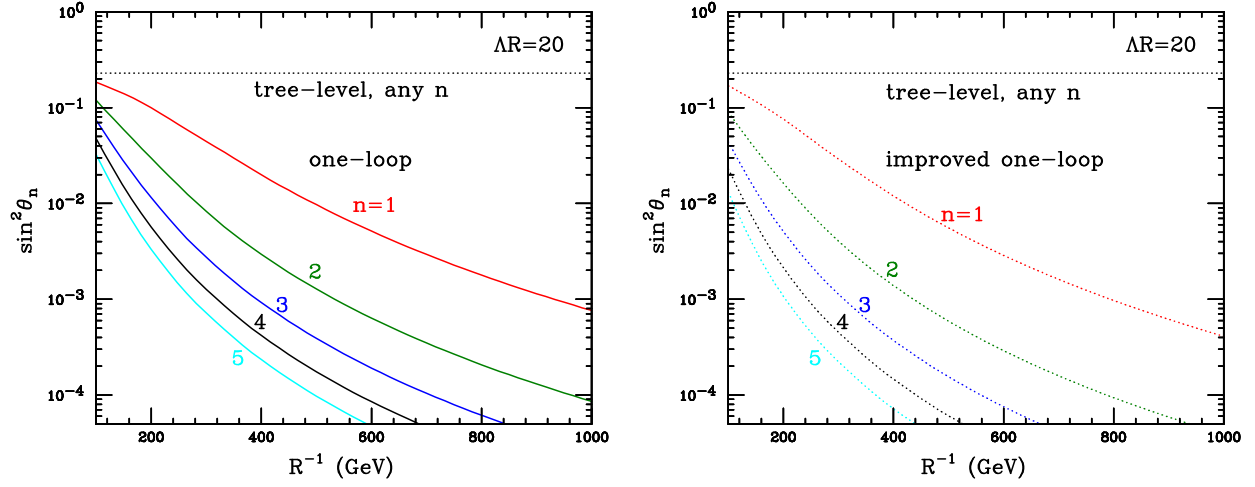


Figure 28: Dependence of the Weinberg angle  $\theta_n$  for KK levels ( $n = 1, \dots, 5$ ) on  $R^{-1}$  for  $\Lambda R = 20$  with (right) / without (left) finite contributions.

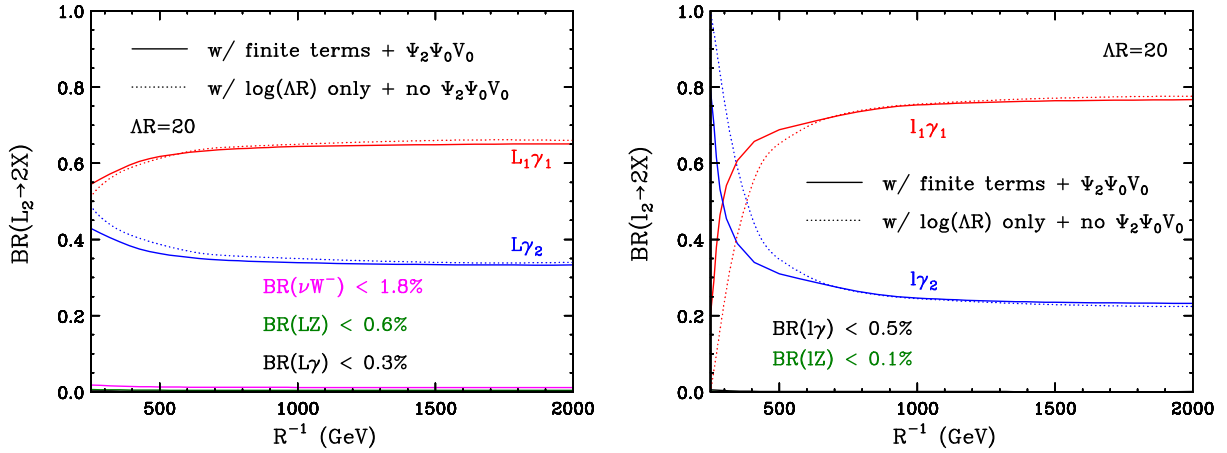


Figure 29: Branching fractions of  $SU(2)_L$ -doublet level-2 KK lepton (left) and charged  $SU(2)_L$ -singlet level-2 KK lepton (right). Solid curves include finite corrections and new decay channels, while dotted curves are old results.

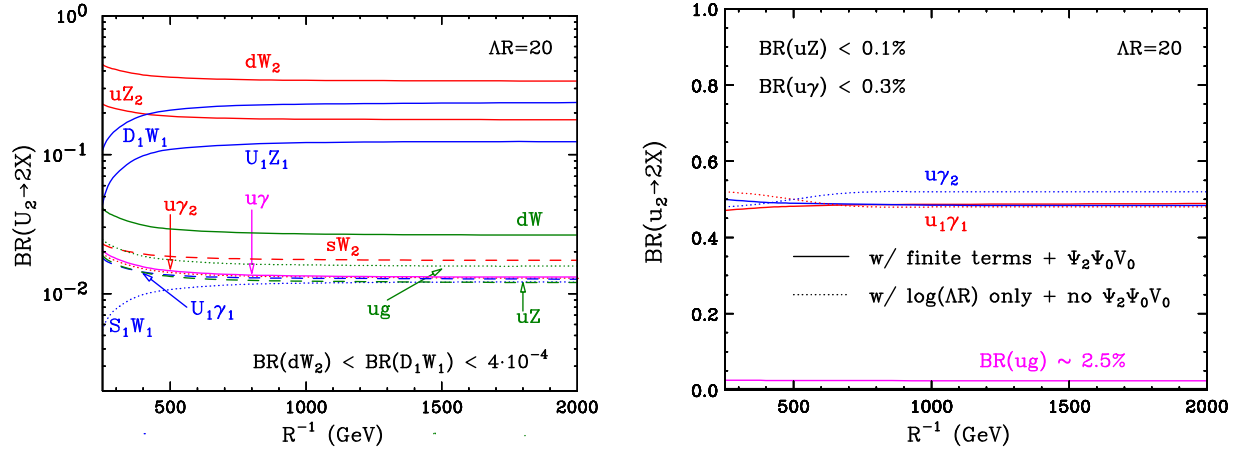


Figure 30: Branching fraction of  $SU(2)_L$ -doublet level-2 KK quark (left) and  $SU(2)_L$ -singlet level-2 KK quark (right) for the up-type.

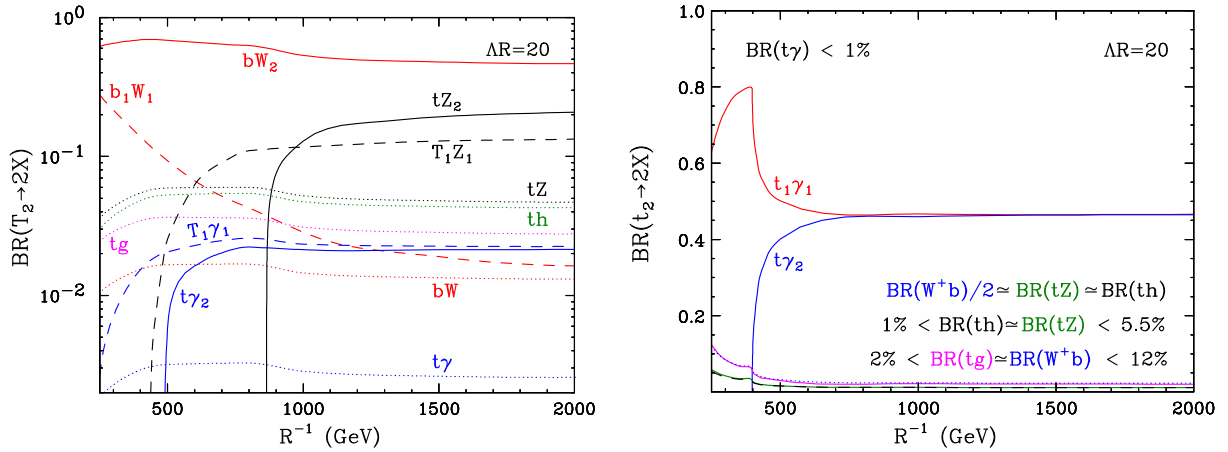


Figure 31: Branching fraction of  $SU(2)_L$ -doublet KK top quark (left) and  $SU(2)_L$ -singlet KK top quark (right).

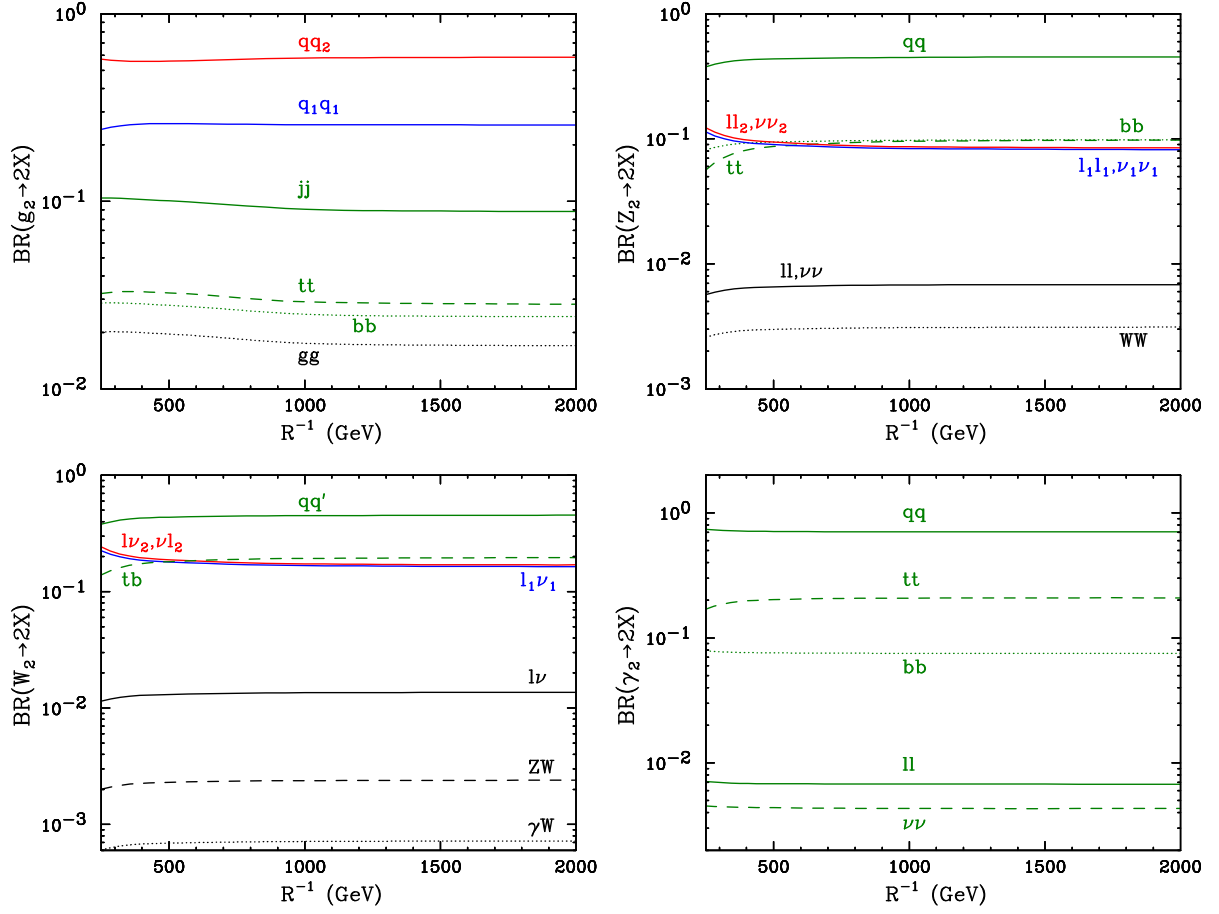


Figure 32: Branching fractions of  $\gamma_2$ ,  $Z_2$ ,  $W_2^\pm$  and  $g_2$  for  $\Lambda R = 20$ .

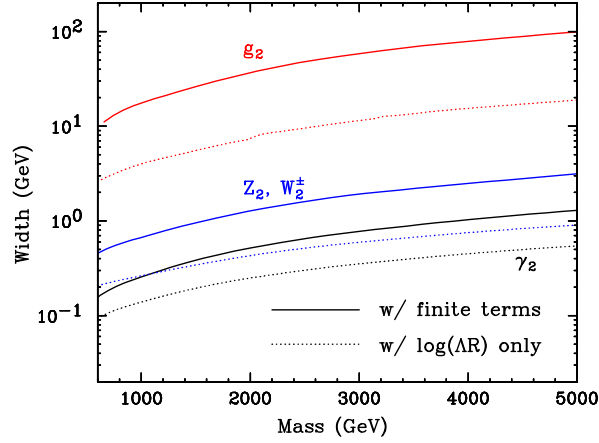


Figure 33: The decay width of level-2 gauge bosons as a function of  $R^{-1}$  for  $\Lambda R = 20$ . Solid curves include finite corrections, while dotted curves are old results.

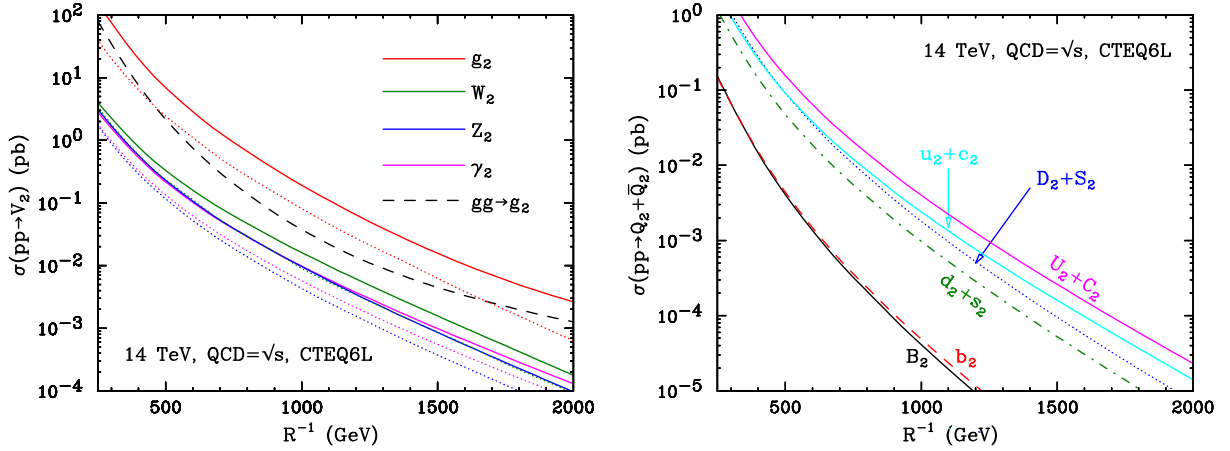


Figure 34: Single production cross section of level-2 KK gauge bosons (left) and level-2 KK fermions (right) as a function of  $R^{-1}$ . Dotted curves (left) are results from Ref. [97] and solid curves are new results including finite terms. Level-2 fermion cross sections and  $\sigma(gg \rightarrow g_2)$  have been computed first time. The cut-off scale has been set to  $\Lambda R = 20$ .

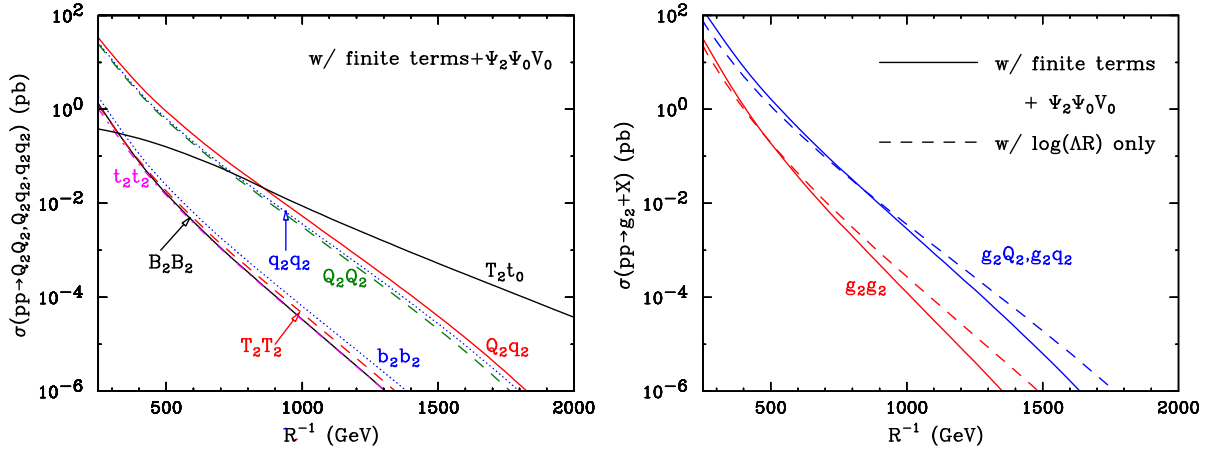


Figure 35: Strong production of  $n = 2$  KK particles at the 14 TeV LHC. The left panel shows KK-quark pair production, while the right panel shows KK-quark/KK-gluon associated production and KK gluon pair production. Updated results (solid curves) are similar to old results (in dashed curves from Ref. [97]). The cut-off scale has been set to  $\Lambda R = 20$ .

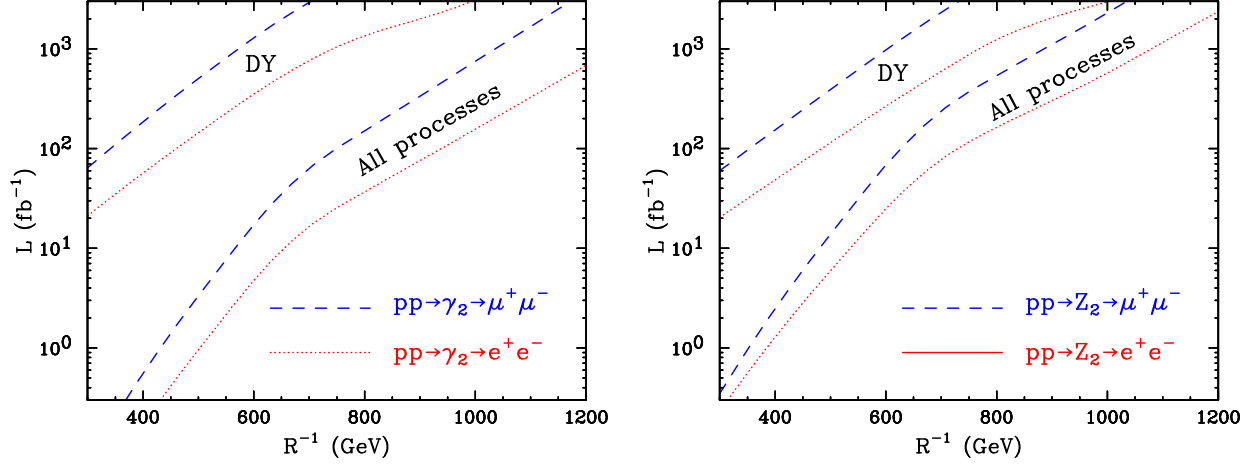


Figure 36:  $5\sigma$  discovery reach for  $\gamma_2$  (left) and  $Z_2$  (right). We show the total integrated luminosity  $\mathcal{L}$  (in  $\text{fb}^{-1}$ ) required for a  $5\sigma$  excess of signal over SM backgrounds in the di-electron (red, dotted) and di-muon (blue, dashed) channels. In each plot, the upper set of curves labeled as ‘DY’ make use of the single production of  $\gamma_2$  or  $Z_2$  (from Fig. 34), while the lower set of curves labeled as ‘All processes’ includes indirect  $\gamma_2$  and  $Z_2$  productions from  $n = 2$  KK quarks (see Fig. 35). We assumed the same signal and background efficiencies used in Ref. [97] and combined with our updated cross sections and branching fractions.

## 6.0 CONCLUSIONS AND OUTLOOK

In this dissertation I investigated the impact of radiative corrections and loop-induced processes on our understanding of the Standard Model formulated with a Universal Extra Dimension compactified on a  $S_1/Z_2$  orbifold. After giving a general introduction to the models and techniques at work I then presented our findings in a number of projects:

- In Chapter 3 I presented our calculation of the NLO corrections to the pair production of heavy vector color octets, as they appear in the two-site Coloron model. This served as a low-energy approximation for the production of level-1 KK-gluons, similar to a model where all higher modes were integrated out. The renormalization procedure involved several subtleties, which were discussed in detail. Furthermore I described the two-cutoff phase space slicing procedure, which was employed to remove the infrared divergencies from our calculation.

The impact of the corrections to the cross section was found to be modest, as it reduced the numerical value by 11 – 14%. The uncertainty introduced into the leading order result through unphysical renormalization and factorization scales is largely reduced in the NLO result.

- In Chapter 4 I discussed the uncertainty introduced into mUED predictions (like the ones in the previous chapter) through truncating the KK-towers at a UV-cutoff scale  $\Lambda$ . To that end I reviewed our calculation of the vertex corrections contributing to the SM QCD operators and the mUED operators containing two KK-1 modes as external legs. To account for the infrared behavior of the  $q_0 - Q_1 - G_1$  vertex function we calculated the full one-loop decay width  $\Gamma[G_1 \rightarrow q_0 Q_1]$  using two cutoff phase-space slicing. The contributions from higher modes were then treated through an analytic summation over

the modes up to the cutoff. Afterwards we extracted the asymptotic behavior of the sums with respect to  $\Lambda$ . As an additional independent method we also calculated the results again by applying the exact functional renormalization group to the uncompactified theory in 5D.

We found that the terms up to linear and logarithmic order of the direct summation describe the vertex functions astonishingly well. Furthermore do the SM vertex function exhibit the same leading order behavior as the KK vertex functions, causing them to converge in the limit of large  $\Lambda$ . The functional renormalization group analysis revealed that the same behavior is shown by the uncompactified theory. The numerical difference between the methods considered is of the order of a few percent.

- In Chapter 5 I revisit our study of the impact that radiatively induced boundary operators have on the phenomenology of mUED. The operators investigated were mass corrections to the entire mUED particle spectrum and KK-number violating three-point interactions. Results for a number of these have been scattered throughout the literature but were constrained to the terms proportional to the logarithm of the cutoff scale. We reported the finite pieces for each of these results and found them to be comparable in size. Additionally we found a number of new operators that are not logarithmically sensitive to  $\Lambda$ .

We found the mass spectrum to be considerably broadened by the new finite terms calculated, and also that the right-handed KK-lepton is always the next-to-lightest particle in the hierarchy. The KK-number violating couplings allow for level-2 KK modes to decay radiatively into a pair of SM particles. We discussed the changes of the branching fractions and discovery reaches in light of the new and updated results.

Even though chances are slim for a particular BSM model to "correctly" describe nature, a large number of models within a certain class share similar characteristic features. Therefore it is not sensible to analyze ones favorite model, in hope of defying the odds and predict a groundbreaking discovery. The best course modern phenomenology can take is to develop universal tools and search strategies, covering as many of those distinguishing features as possible. Once decisive discoveries pointing into the direction of new physics are made it is of utmost importance to have a robust analysis machine ready to understand the results

obtained and put them in context.

In this thesis I employed minimal Universal Extra Dimensions as a concrete framework but focused to understand some of the features that many extra dimensional models generally share, making our insights, results and developed tools applicable to many scenarios. I hope to have made a contribution in terms of this philosophy, since this truly is an exciting time for physics, where hints to what lies beyond the Standard Model may be lurking just around the corner.

## APPENDIX A

### LAGRANGIANS AND FEYNMAN RULES

#### A.1 MUED LAGRANGIAN

This appendix lists a complete set of Standard Model Lagrangian in a universal extra dimensions model in 5 dimensions with a  $S^1/\mathbb{Z}_2$  orbifold compactification. The conventions are chosen such that Greek indices take values 0, 1, 2, 3, assigned to the uncompactified dimensions, while capital Latin indices describe the full 5D theory, where the extra spatial dimension is denoted as  $x^5$  where necessary. The 5D coupling constants are labeled with a superscript (5) and are related to the 4D effective couplings through

$$g = \frac{g^{(5)}}{\sqrt{\pi R}}, \quad h_i = \frac{h_i^{(5)}}{\sqrt{\pi R}}, \quad \lambda = \frac{\lambda^{(5)}}{\pi R}, \quad (\text{A.1})$$

for the gauge, Yukawa and Higgs self coupling respectively.

Furthermore we have to define the conventions for the extension of the Clifford algebra,

$$\Gamma^M = (\gamma^\mu, i\gamma^5), \quad \text{such that} \quad \{\Gamma^M, \Gamma^N\} = 2\eta^{MN}, \quad (\text{A.2})$$

where  $\eta^{MN}$  is the flat 5D metric tensor

$$\eta_{MN} = \begin{pmatrix} \eta_{\mu\nu} & 0 \\ 0 & -1 \end{pmatrix}, \quad (\text{A.3})$$

and  $\eta^{\mu\nu} = \text{diag}\{+ - - -\}$  the usual 4D Minkowski metric. It is also helpful to define an extended set of  $\Delta$  symbols [26]

$$\begin{aligned}
\Delta_{mnl}^1 &= \delta_{l,m+n} + \delta_{n,l+m} + \delta_{m,l+n}, \\
\Delta_{mnlk}^2 &= \delta_{k,l+m+n} + \delta_{l,m+n+k} + \delta_{m,n+k+l} + \delta_{n,k+l+m} + \delta_{k+m,l+n} + \delta_{k+l,m+n} + \delta_{k+n,l+m}, \\
\Delta_{mnlk}^3 &= -\delta_{k,l+m+n} - \delta_{l,m+n+k} - \delta_{m,n+k+l} - \delta_{n,k+l+m} + \delta_{k+l,m+n} + \delta_{k+m,l+n} + \delta_{k+n,l+m}, \\
\Delta_{mnl}^4 &= -\delta_{l,m+n} + \delta_{n,l+m} + \delta_{m,l+n}, \\
\Delta_{mnlk}^5 &= -\delta_{k,l+m+n} - \delta_{l,m+n+k} + \delta_{m,n+k+l} + \delta_{n,k+l+m} - \delta_{k+l,m+n} + \delta_{k+m,l+n} + \delta_{k+n,l+m}.
\end{aligned} \tag{A.4}$$

### A.1.1 The Gauge Sector

As a generic example, we show the gauge sector Lagrangian for a single vector field in the adjoint representation of  $SU(N)$ , which contains a four-component vector  $V_\mu(x, x^5)$  and a fifth component  $V_5(x, x^5)$ , which takes the role of a Goldstone boson. Additionally we require the ghost field  $c(x, x^5)$ . After compactification the Lagrangians read

$$\begin{aligned}
\mathcal{L}_{\text{Gauge}} &= \frac{1}{2} \int_{-\pi R}^{\pi R} dx^5 \left\{ -\frac{1}{4} F_{MN}^a F^{a,MN} \right\} = \frac{1}{2} \int_{-\pi R}^{\pi R} dx^5 \left\{ -\frac{1}{4} F_{\mu\nu}^a F^{a,\mu\nu} - \frac{1}{2} F_{5\nu}^a F^{a,5\nu} \right\}, \\
\mathcal{L}_{\text{GF}} &= \frac{1}{2} \int_{-\pi R}^{\pi R} dx^5 \left\{ -\frac{1}{2\xi} (\partial^\mu V_\mu^a(x, x^5) - \xi \partial_5 V_5^a(x, x^5))^2 \right\}, \\
\mathcal{L}_{\text{Ghost}} &= \frac{1}{2} \int_{-\pi R}^{\pi R} dx^5 \left\{ \bar{c}^a(x, x^5) (-\partial^\mu \partial_\mu + \xi \partial_5^2) c^a(x, x^5) \right. \\
&\quad \left. + g^{(5)} f^{abc} (-\partial^\mu \bar{c}^a(x, x^5) V_\mu^c(x, x^5) c^b(x, x^5) + \xi \partial_5 \bar{c}^a(x, x^5) V_5^c c^b(x, x^5)) \right\}, \tag{A.5}
\end{aligned}$$

with  $\xi$  being the gauge parameter in the generalized  $R_\xi$  gauge. After decomposing the 5D fields into Fourier modes, according to

$$\begin{aligned}
V_\mu(x, x^5) &= \frac{1}{\sqrt{\pi R}} \left[ V_\mu^0(x) + \sqrt{2} \sum_{n=1}^{\infty} V_\mu^n(x) \cos \frac{nx^5}{R} \right], \\
V_5(x, x^5) &= \sqrt{\frac{2}{\pi R}} \sum_{n=1}^{\infty} V_5^n(x) \sin \frac{nx^5}{R}, \\
c^a(x, x^5) &= \frac{1}{\sqrt{\pi R}} \left[ c^{0,a}(x) + \sqrt{2} \sum_{n=1}^{\infty} c^{n,a}(x) \cos \frac{nx^5}{R} \right], \tag{A.6}
\end{aligned}$$

and performing the integral over the fifth dimension one obtains the effectively 4D pure Yang-Mills pieces, given by

$$\begin{aligned}
\frac{1}{2} \int_{-\pi R}^{\pi R} dx^5 (F_{5\nu}^a F^{a5\nu}) &= - \sum_{n=1}^{\infty} \left( \frac{n}{R} V_{\mu}^{n,a} + \partial_{\mu} V_5^n - g C^{abc} V_5^{n,b} V_{\mu}^{0,c} \right)^2 \\
&+ \sum_{m,n,l=1}^{\infty} \sqrt{2} g C^{ade} \left( \frac{m}{R} V_{\mu}^{m,a} + \partial_{\mu} V_5^{m,a} - g C^{abc} V_5^{m,b} V_{\mu}^{0,c} \right) V_5^{n,d} V^{l,e\mu} \Delta_{mnl}^4 \\
&- \frac{g^2}{2} C^{abc} C^{ade} \sum_{m,n,l,k=1}^{\infty} V_5^{m,b} V_{\mu}^{n,c} V_5^{l,d} V^{k,e\mu} \Delta_{mlnk}^5, \tag{A.7}
\end{aligned}$$

$$\begin{aligned}
\frac{1}{2} \int_{-\pi R}^{\pi R} dx^5 (F_{\mu\nu}^a F^{a\mu\nu}) &= F_{\mu\nu}^{0,a} F^{0,a\mu\nu} + 2g C^{abc} \sum_{n=1}^{\infty} F_{\mu\nu}^{0,a} V^{n,b\mu} V^{n,c\nu} + \sum_{n=1}^{\infty} (\partial_{\mu} V_{\nu}^{n,a} - \partial_{\nu} V_{\mu}^{n,a})^2 \\
&+ 2g C^{abc} \sum_{n=1}^{\infty} (\partial_{\mu} V_{\nu}^{n,a} - \partial_{\nu} V_{\mu}^{n,a}) (V^{0,b\mu} V^{n,c\nu} + V^{0,c\nu} V^{n,b\mu}) \\
&+ \sqrt{2} g C^{abc} \sum_{m,n,l=1}^{\infty} (\partial_{\mu} V_{\nu}^{m,a} - \partial_{\nu} V_{\mu}^{m,a}) V^{n,b\mu} V^{l,c\nu} \Delta_{mnl}^1 \\
&+ \sum_{n=1}^{\infty} g^2 (C^{abc} (V_{\mu}^{0,b} V_{\nu}^{n,c} + V_{\nu}^{0,c} V_{\mu}^{n,b}))^2 \\
&+ \sqrt{2} g^2 \sum_{m,n,l=1}^{\infty} C^{abc} C^{ade} (V_{\mu}^{0,b} V_{\nu}^{m,c} + V_{\nu}^{0,c} V_{\mu}^{m,b}) V^{n,d\mu} V^{l,e\nu} \Delta_{mnl}^1 \\
&+ \sum_{m,n,l,k=1}^{\infty} \frac{g^2}{2} C^{abc} C^{ade} V_{\mu}^{m,b} V_{\nu}^{n,c} V^{l,d\mu} V^{k,e\nu} \Delta_{mnlk}^2, \tag{A.8}
\end{aligned}$$

a gauge fixing part given by

$$\mathcal{L}_{\text{GF}} = -\frac{1}{2\xi} \left[ (\partial^{\mu} V_{\mu}^0)^2 + \sum_{n=1}^{\infty} \left( \partial^{\mu} V_{\mu}^n - \frac{\xi n}{R} V_5^n \right)^2 \right], \tag{A.9}$$

and finally the ghost piece

$$\begin{aligned}
\mathcal{L}_{\text{Ghost}} &= -\bar{c}^{0,a} \partial^{\mu} \partial_{\mu} c^{0,a} - g f^{abc} \partial^{\mu} \bar{c}^{0,a} V_{\mu}^{0,c} c^{0,b} - \sum_{n=1}^{\infty} \left[ \bar{c}^{n,a} \partial^{\mu} \partial_{\mu} c^{n,a} + \xi \frac{n^2}{R^2} \bar{c}^{n,a} c^{n,a} \right] \\
&- g f^{abc} \sum_{n=1}^{\infty} \left[ \partial^{\mu} \bar{c}^{0,a} V_{\mu}^{n,c} c^{n,b} + \partial^{\mu} \bar{c}^{n,a} V_{\mu}^{0,c} c^{n,b} + \partial^{\mu} \bar{c}^{n,a} V_{\mu}^{n,c} c^{0,b} + \xi \frac{n}{R} \bar{c}^{n,a} V_5^{n,b} c^{0,c} \right] \\
&- \frac{g}{\sqrt{2}} f^{abc} \sum_{m,n,l=1}^{\infty} \left[ \partial^{\mu} \bar{c}^{l,a} V_{\mu}^{m,c} c^{n,b} \Delta_{lmn}^1 + \xi \frac{l}{R} \bar{c}^{l,a} V_5^{m,c} c^{n,b} \Delta_{lmn}^4 \right]. \tag{A.10}
\end{aligned}$$

### A.1.2 The Fermion Sector

Analogously, we show the Lagrangian for a fermion in the fundamental representation coupled to a generic  $SU(N)$  gauge field. The structure of the SM makes it necessary to distinguish between Fermions  $\Psi$  that transform as doublets under  $SU(2)$  and those that are singlets  $\psi$ . Their respective decomposition is

$$\begin{aligned}\Psi(x, x^5) &= \frac{1}{\sqrt{\pi R}} \left\{ \Psi_L(x) + \sqrt{2} \sum_{n=1}^{\infty} \left[ P_- \Psi_L^n(x) \cos \frac{nx^5}{R} + P_+ \Psi_R^n(x) \sin \frac{nx^5}{R} \right] \right\}, \\ \psi(x, x^5) &= \frac{1}{\sqrt{\pi R}} \left\{ \psi_R(x) + \sqrt{2} \sum_{n=1}^{\infty} \left[ P_+ \psi_R^n(x) \cos \frac{nx^5}{R} + P_- \psi_L^n(x) \sin \frac{nx^5}{R} \right] \right\}.\end{aligned}\quad (\text{A.11})$$

The generic Lagrangian for either of the Fermions coupling to  $V_M(x, x^5)$  can be written as

$$\begin{aligned}\mathcal{L}_\Psi &= \frac{1}{2} \int_{-\pi R}^{\pi R} dx^5 \{ i \bar{\Psi}(x, x^5) \Gamma^M [\partial_M + ig^{(5)} V_M(x, x^5)] \Psi(x, x^5) \} \\ &= i \bar{\Psi}_L \gamma^\mu (\partial_\mu + ig V_\mu^0) \Psi_L - \sum_{n=1}^{\infty} \frac{n}{R} [\bar{\Psi}_R^n \Psi_L^n + \bar{\Psi}_L^n \Psi_R^n] \\ &+ \sum_{n=1}^{\infty} [i \bar{\Psi}_R^n \gamma^\mu (\partial_\mu + ig V_\mu^0) \Psi_R^n + i \bar{\Psi}_L^n \gamma^\mu (\partial_\mu + ig V_\mu^0) \Psi_L^n - g \bar{\Psi}_L \gamma^\mu V_\mu^n \Psi_L^n + g \bar{q}_L i \gamma^5 V_5^n \Psi_R^n] \\ &- \frac{g}{\sqrt{2}} \sum_{m,n,l=1}^{\infty} [\bar{\Psi}_L^m \gamma^\mu V_\mu^n \Psi_L^l \Delta_{mnl}^1 + \bar{\Psi}_R^m \gamma^\mu V_\mu^n \Psi_R^l \Delta_{mln}^4 + \bar{\Psi}_L^m i \gamma^5 V_5^n \Psi_R^l \Delta_{lnm}^4].\end{aligned}\quad (\text{A.12})$$

### A.1.3 The Higgs Sector

Due to the somewhat complicated structure of the four-point interactions between the Higgs and electroweak gauge bosons, we here show the Higgs Lagrangian not just for a generic gauge group, but write the explicit Lagrangian for a Higgs doublet coupling to the  $U(1)_Y$  field  $B_M(x, x^5)$  and the  $SU(2)_L$  field  $W_M(x, x^5)$ .

The Higgs doublet  $\Phi(x, x^5)$  is decomposed as

$$\Phi(x, x^5) = \frac{1}{\sqrt{\pi R}} \left\{ \Phi_0(x) + \sqrt{2} \sum_{n=1}^{\infty} \Phi_n(x) \cos \frac{nx^5}{R} \right\} \quad (\text{A.13})$$

and inserted into the Lagrangian

$$\mathcal{L}_{\text{Higgs}} = \frac{1}{2} \int_{-\pi R}^{\pi R} dx^5 \left[ (D_M \Phi(x, x^5))^\dagger (D^M \Phi(x, x^5)) + \mu^2 \Phi^\dagger(x, x^5) \Phi(x, x^5) - \lambda (\Phi^\dagger(x, x^5) \Phi(x, x^5))^2 \right]$$

$$\begin{aligned}
&= \left[ \left( \partial_\mu + ig_2 W_\mu^0 + \frac{ig_1}{2} B_\mu^0 \right) \Phi_0 \right]^\dagger \left[ \left( \partial^\mu + ig_2 W^{0\mu} + \frac{ig_1}{2} B^{0\mu} \right) \Phi_0 \right] \\
&+ \sum_{n=1}^{\infty} \left[ \left( \partial_\mu + ig_2 W_\mu^0 + \frac{ig_1}{2} B_\mu^0 \right) \Phi_n \right]^\dagger \left[ \left( \partial^\mu + ig_2 W^{0\mu} + \frac{ig_1}{2} B^{0\mu} \right) \Phi_n \right] \\
&+ ig_2 \sum_{n=1}^{\infty} \left[ (\partial^\mu \Phi_0)^\dagger W_\mu^n \Phi_n + (\partial^\mu \Phi_n)^\dagger W_\mu^n \Phi_0 - \Phi_n^\dagger W_\mu^{n\dagger} (\partial^\mu \Phi_0) - \Phi_0^\dagger W_\mu^{n\dagger} (\partial^\mu \Phi_n) \right] \\
&+ ig_2 \sum_{m,n,l=1}^{\infty} \left[ (\partial^\mu \Phi_m)^\dagger W_\mu^n \Phi_l - \Phi_l^\dagger W_\mu^{n\dagger} (\partial^\mu \Phi_m) \right] \Delta_{mnl}^1 \\
&+ \frac{ig_1}{2} \sum_{n=1}^{\infty} \left[ (\partial^\mu \Phi_0)^\dagger B_\mu^n \Phi_n + (\partial^\mu \Phi_n)^\dagger B_\mu^n \Phi_0 - \Phi_n^\dagger B_\mu^n (\partial^\mu \Phi_0) - \Phi_0^\dagger B_\mu^n (\partial^\mu \Phi_n) \right] \\
&+ \frac{ig_1}{2\sqrt{2}} \sum_{m,n,l=1}^{\infty} \left[ (\partial^\mu \Phi_m)^\dagger B_\mu^n \Phi_l - \Phi_l^\dagger B_\mu^n (\partial^\mu \Phi_m) \right] \Delta_{mnl}^1 \\
&+ g_2^2 \sum_{n=1}^{\infty} \left[ \Phi_0^\dagger W_\mu^{0\dagger} W^{n\mu} \Phi_n + \Phi_n^\dagger W_\mu^{0\dagger} W^{n\mu} \Phi_0 + \Phi_0^\dagger W^{n\mu\dagger} W_\mu^0 \Phi_n + \Phi_0^\dagger W^{n\mu\dagger} W_\mu^0 \Phi_n + \Phi_n^\dagger W^{n\mu\dagger} W_\mu^0 \Phi_0 \right] \\
&+ \frac{g_2^2}{\sqrt{2}} \sum_{m,n,l=1}^{\infty} \left[ \Phi_m^\dagger W_\mu^{0\dagger} W^{n\mu} \Phi_l + \Phi_0^\dagger W_\mu^{m\dagger} W^{l\mu} \Phi_n + \Phi_m^\dagger W_\mu^{n\dagger} W^{0\mu} \Phi_l + \Phi_m^\dagger W_\mu^{n\dagger} W^{l\mu} \Phi_0 \right] \Delta_{mnl}^1 \\
&+ \frac{g_2^2}{2} \sum_{m,n,l,k=1}^{\infty} \left[ \Phi_m^\dagger W_\mu^{n\dagger} W^{l\mu} \Phi_k \right] \Delta_{mnlk}^2 \\
&+ \frac{g_1 g_2}{2} \sum_{n=1}^{\infty} \left[ \Phi_0^\dagger W_\mu^{0\dagger} B^{n\mu} \Phi_n + \Phi_n^\dagger W_\mu^{0\dagger} B^{n\mu} \Phi_0 + \Phi_0^\dagger W_\mu^{n\dagger} B^{0\mu} \Phi_n + \Phi_0^\dagger W_\mu^{n\dagger} B^{n\mu} \Phi_0 + \Phi_n^\dagger W_\mu^{n\dagger} B^{0\mu} \Phi_0 \right. \\
&\quad \left. + \Phi_n^\dagger B^{n\mu} W_\mu^0 \Phi_0 + \Phi_0^\dagger B^{n\mu} W_\mu^0 \Phi_n + \Phi_n^\dagger B^{0\mu} W_\mu^n \Phi_0 + \Phi_0^\dagger B^{n\mu} W_\mu^n \Phi_0 + \Phi_0^\dagger B^{0\mu} W_\mu^n \Phi_n \right] \\
&+ \frac{g_1 g_2}{2\sqrt{2}} \sum_{m,n,l=1}^{\infty} \left[ \Phi_m^\dagger W_\mu^{0\dagger} B^{n\mu} \Phi_l + \Phi_0^\dagger W_\mu^{m\dagger} B^{l\mu} \Phi_n + \Phi_m^\dagger W_\mu^{n\dagger} B^{0\mu} \Phi_l + \Phi_m^\dagger W_\mu^{n\dagger} B^{l\mu} \Phi_0 \right. \\
&\quad \left. + \Phi_l^\dagger B^{n\mu} W_\mu^0 \Phi_m + \Phi_n^\dagger B^{l\mu} W_\mu^m \Phi_0 + \Phi_l^\dagger B^{0\mu} W_\mu^n \Phi_m + \Phi_0^\dagger B^{l\mu} W_\mu^n \Phi_m \right] \Delta_{mnl}^1 \\
&+ \frac{g_1 g_2}{4} \sum_{m,n,l,k=1}^{\infty} \left[ \Phi_m^\dagger W_\mu^{n\dagger} B^{l\mu} \Phi_k + \Phi_k^\dagger B^{l\mu} W_\mu^n \Phi_m \right] \Delta_{mnlk}^2 \\
&+ \frac{g_1^2}{4} \sum_{n=1}^{\infty} \left[ 2\Phi_0^\dagger B_\mu^0 B^{n\mu} \Phi_n + 2\Phi_n^\dagger B_\mu^0 B^{n\mu} \Phi_0 + \Phi_0^\dagger B_\mu^n B^{n\mu} \Phi_0 \right] \\
&+ \frac{g_1^2}{4\sqrt{2}} \sum_{m,n,l=1}^{\infty} \left[ 2\Phi_m^\dagger B_\mu^0 B^{n\mu} \Phi_l + \Phi_0^\dagger B_\mu^m B^{l\mu} \Phi_n + \Phi_m^\dagger B_\mu^n B^{l\mu} \Phi_0 \right] \Delta_{mnl}^1 \\
&+ \frac{g_1^2}{4} \sum_{m,n,l,k=1}^{\infty} \left[ \Phi_m^\dagger B_\mu^n B^{l\mu} \Phi_k \right] \Delta_{mnlk}^2
\end{aligned}$$

$$\begin{aligned}
& + \mu^2 \left[ \Phi_0^\dagger \Phi_0 + \sum_{n=1}^{\infty} \Phi_n^\dagger \Phi_n \right] - \sum_{n=1}^{\infty} \left( \frac{n}{R} \right)^2 \Phi_n^\dagger \Phi_n \\
& + \frac{1}{\sqrt{2}} \sum_{m,n,l=1}^{\infty} \frac{n}{R} \Phi_n^\dagger \left( \frac{ig_1}{2} B_5^m + ig_2 W_5^m \right) \Phi_l \Delta_{mnl}^4 \\
& - \frac{1}{\sqrt{2}} \sum_{m,n,l=1}^{\infty} \frac{m}{R} \Phi_l^\dagger \left( \frac{ig_1}{2} B_5^n + ig_2 W_5^n \right) \Phi_m \Delta_{mnl}^4 \\
& - \frac{1}{2} \sum_{m,n,l,k=1}^{\infty} \Phi_l^\dagger \left( \frac{ig_1}{2} B_5^m + ig_2 W_5^{m\dagger} \right) \left( \frac{ig_1}{2} B_5^n + ig_2 W_5^n \right) \Phi_k \Delta_{mnlk}^5 \\
& + \sum_{n=1}^{\infty} \left[ \Phi_0^\dagger \left( g_2 W_5^n + \frac{g_1}{2} B_5^n \right)^2 \Phi_0 - \frac{n}{R} \Phi_0^\dagger \left( g_2 W_5^n + \frac{g_1}{2} B_5^n \right) \Phi_n + \frac{n}{R} \Phi_n^\dagger \left( g_2 W_5^n + \frac{g_1}{2} B_5^n \right) \Phi_0 \right] \\
& - \frac{1}{\sqrt{2}} \sum_{m,n,l=1}^{\infty} \left[ \Phi_0^\dagger \left( g_2 W_5^k + \frac{g_1}{2} B_5^k \right) \left( g_2 W_5^l + \frac{g_1}{2} B_5^l \right) \Phi_m \right. \\
& \quad \left. + \Phi_m^\dagger \left( g_2 W_5^k + \frac{g_1}{2} B_5^k \right) \left( g_2 W_5^l + \frac{g_1}{2} B_5^l \right) \Phi_0 \right] \Delta_{klm}^4 \\
& - \lambda \left( \Phi_0^\dagger \Phi_0 \right)^2 - \lambda \sum_{n=1}^{\infty} \left[ \left( \Phi_0^\dagger \Phi_n + \Phi_n^\dagger \Phi_0 \right)^2 + 2 \Phi_0^\dagger \Phi_0 \Phi_n^\dagger \Phi_n \right] \\
& - \sqrt{2} \lambda \sum_{m,n,l=1}^{\infty} \Phi_m^\dagger \Phi_n \left( \Phi_l^\dagger \Phi_0 + \Phi_0^\dagger \Phi_l \right) \Delta_{mnl}^1 - \frac{\lambda}{2} \sum_{m,n,l,k=1}^{\infty} \Phi_m^\dagger \Phi_n \Phi_l^\dagger \Phi_k \Delta_{mnlk}^2. \tag{A.14}
\end{aligned}$$

### A.1.4 The Yukawa Sector

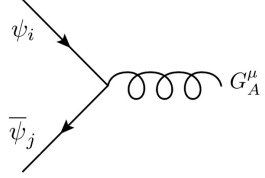
To ensure that the SM Fermions acquire a mass through EWSB one has to consider the Yukawa couplings to the Higgs field. For a down-type fermion they are described by

$$\begin{aligned}
\mathcal{L}_{\text{Yukawa}} &= \frac{1}{2} \int_{-\pi R}^{\pi R} dx^5 \left\{ h_i^{(5)} \bar{\Psi}(x, x^5) \psi(x, x^5) \Phi(x, x^5) \right\} \\
&= h_i \bar{\Psi}_L \psi_R \Phi_0 + h_i \sum_{n=1}^{\infty} \left[ \bar{\Psi}_L^n \psi_R^n \Phi_0 + \bar{\Psi}_R^n \psi_L^n \Phi_0 \right] + h_i \sum_{n=1}^{\infty} \left[ \bar{\Psi}_L \psi_R^n \Phi_n + \bar{\Psi}_L^n \psi_R \Phi_n \right] \\
&+ \frac{h_i}{\sqrt{2}} \sum_{m,n,l=1}^{\infty} \left[ \bar{\Psi}_L^n \psi_R^m \Phi_l \Delta_{mnl}^1 + \bar{\Psi}_R^n \psi_L^m \Phi_l \Delta_{mnl}^4 \right]. \tag{A.15}
\end{aligned}$$

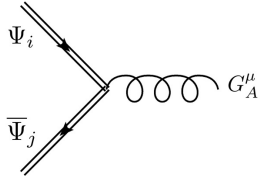
and for an up-type fermion they can be constructed in complete analogy.

## A.2 FEYNMAN RULES FOR THE TWO-SITE COLORON MODEL

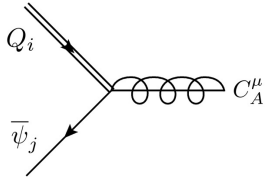
### A.2.1 Feynman Rules Involving Massless Quarks



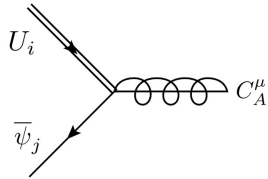
$$-ig_s \gamma^\mu T_{ij}^A \quad (\text{A.16})$$



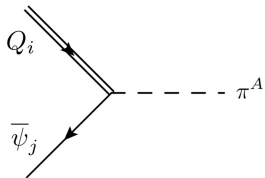
$$-ig_s \gamma^\mu T_{ij}^A \quad (\text{A.17})$$



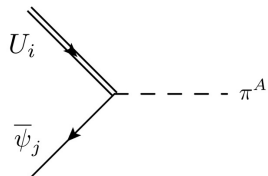
$$-ig_s \gamma^\mu P_L T_{ij}^A \quad (\text{A.18})$$



$$ig_s \gamma^\mu P_R T_{ij}^A \quad (\text{A.19})$$

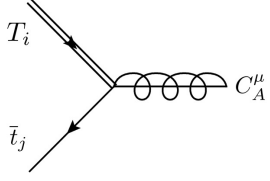


$$-g_s P_R T_{ij}^a \quad (\text{A.20})$$

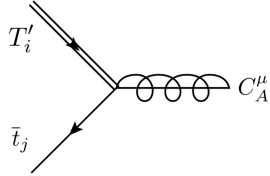


$$g_s P_L T_{ij}^a \quad (\text{A.21})$$

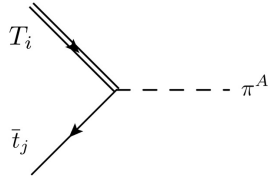
### A.2.2 Vertices Involving the Top Quark



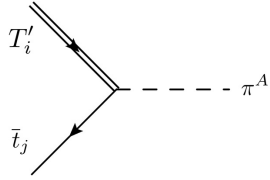
$$-ig_s \gamma^\mu [\sin \theta_T P_R + \cos \theta_T P_L] T_{ij}^a \quad (\text{A.22})$$



$$ig_s \gamma^\mu [\sin \theta_T P_L + \cos \theta_T P_R] T_{ij}^a \quad (\text{A.23})$$

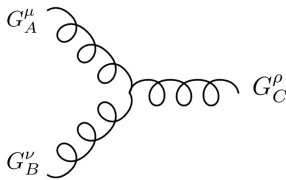


$$g_s [\sin \theta_T P_L - \cos \theta_T P_R] T_{ij}^a \quad (\text{A.24})$$

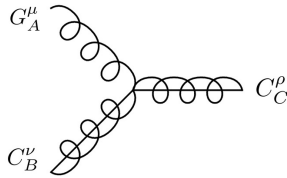


$$-g_s [\sin \theta_T P_R - \cos \theta_T P_L] T_{ij}^a \quad (\text{A.25})$$

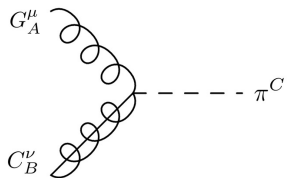
### A.2.3 Three-Point Boson Vertices



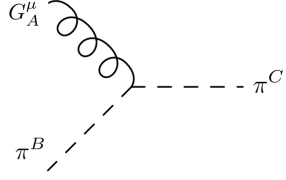
$$g_s [(p_B - p_A)^\rho \eta^{\mu\nu} + (p_A - p_C)^\nu \eta^{\mu\rho} + (p_C - p_B)^\mu \eta^{\nu\rho}] f^{ABC} \quad (\text{A.26})$$



$$g_s [(p_B - p_A)^\rho \eta^{\mu\nu} + (p_A - p_C)^\nu \eta^{\mu\rho} + (p_C - p_B)^\mu \eta^{\nu\rho}] f^{ABC} \quad (\text{A.27})$$

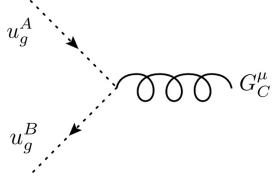


$$-ig_s M \eta^{\mu\nu} f^{ABC} \quad (\text{A.28})$$

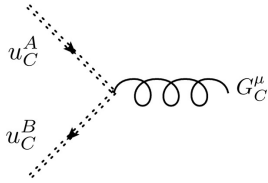


$$g_s (p_B - p_C)^\mu f^{ABC} \quad (\text{A.29})$$

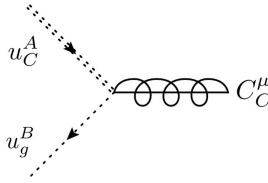
#### A.2.4 Feynman Rules Involving Ghosts



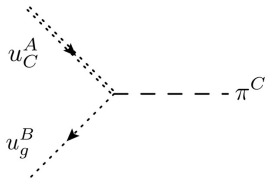
$$-g_s p_B^\mu f^{ABC} \quad (\text{A.30})$$



$$-g_s p_B^\mu f^{ABC} \quad (\text{A.31})$$

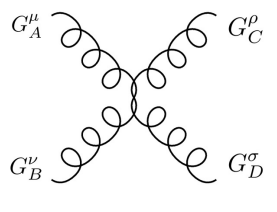


$$-g_s p_B^\mu f^{ABC} \quad (\text{A.32})$$

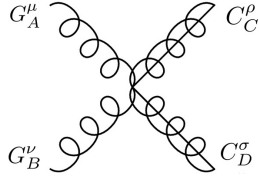


$$-i g_s M f^{ABC} \quad (\text{A.33})$$

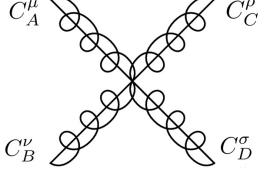
#### A.2.5 Four-Point Boson Vertices



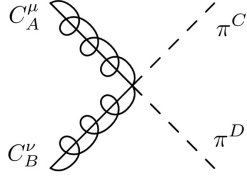
$$\begin{aligned}
 & -i g_s^2 [\eta^{\mu\nu} \eta^{\rho\sigma} (f^{ACE} f^{BDE} - f^{ADE} f^{CBE}) \\
 & \quad + \eta^{\mu\rho} \eta^{\nu\sigma} (f^{ADE} f^{CBE} - f^{ABE} f^{DCE}) \\
 & \quad + \eta^{\mu\sigma} \eta^{\nu\rho} (f^{ABE} f^{DCE} - f^{ACE} f^{BDE})] \quad (\text{A.34})
 \end{aligned}$$



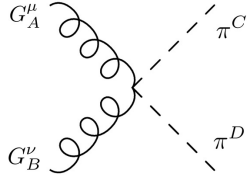
$$\begin{aligned}
& -ig_s^2 [\eta^{\mu\nu}\eta^{\rho\sigma} (f^{ACE} f^{BDE} - f^{ADE} f^{CBE}) \\
& \quad + \eta^{\mu\rho}\eta^{\nu\sigma} (f^{ADE} f^{CBE} - f^{ABE} f^{DCE}) \\
& \quad + \eta^{\mu\sigma}\eta^{\nu\rho} (f^{ABE} f^{DCE} - f^{ACE} f^{BDE})]
\end{aligned} \tag{A.35}$$



$$\begin{aligned}
& -ig_s^2 [\eta^{\mu\nu}\eta^{\rho\sigma} (f^{ACE} f^{BDE} - f^{ADE} f^{CBE}) \\
& \quad + \eta^{\mu\rho}\eta^{\nu\sigma} (f^{ADE} f^{CBE} - f^{ABE} f^{DCE}) \\
& \quad + \eta^{\mu\sigma}\eta^{\nu\rho} (f^{ABE} f^{DCE} - f^{ACE} f^{BDE})]
\end{aligned} \tag{A.36}$$



$$ig_s^2 \eta^{\mu\nu} (f^{ACE} f^{BDE} + f^{BCE} f^{ADE}) \tag{A.37}$$



$$ig_s^2 \eta^{\mu\nu} (f^{ACE} f^{BDE} + f^{BCE} f^{ADE}) \tag{A.38}$$

Note that the Feynman rules in this appendix agree with those for KK-level-1 gluons and quarks in mUED, with the exception of (A.36), which has an additional factor  $\frac{3}{2}$  in mUED.

## APPENDIX B

### SPECIAL INTEGRALS AND FUNCTIONS

#### B.1 ONE LOOP FUNCTIONS AND IDENTITIES

In this appendix we summarize all scalar one-loop functions which exhibit UV or IR/collinear divergencies. These integrals have been calculated in the literature in a variety of ways; we simply summarize the ones important for the calculations in this thesis. Our main points of reference have been [53, 100] as well as [99]. The finite loop functions that could not be reduced to  $A_0$  functions were numerically calculated using LOOPTOOLS.

Since our calculations only concern NLO contributions is it sufficient to consider the real parts of all loop functions up to order  $\epsilon^0$ , we therefore omit any imaginary parts in this appendix.

To list the functions in their most compact form it is useful to define two variables

$$x_1 = \frac{1 - \beta_1}{1 - \beta_1} \quad \text{and} \quad x_2 = \frac{1 - \beta_2}{1 - \beta_2}, \quad (\text{B.1})$$

that themselves depend on

$$\beta_1 = \sqrt{1 - \frac{4m_1^2}{s}} \quad \text{and} \quad \beta_2 = \sqrt{1 - \frac{4m_1 m_2}{s - (m_1 - m_2)^2}}. \quad (\text{B.2})$$

### B.1.1 Integrals with Ultraviolet Divergences

We begin with the scalar tadpole integral

$$A_0(m^2) = \mu^{2\epsilon} \int \frac{d^D q}{i\pi^2} \frac{1}{q^2 - m^2} = m^2 \left[ \frac{1}{\epsilon} + 1 - \log\left(\frac{m^2}{\mu^2}\right) \right] \quad (\text{B.3})$$

and its generalization

$$T_0^N(m^2) = \mu^{2\epsilon} \int \frac{d^D q}{i\pi^2} \frac{1}{[q^2 - m^2]^N} = \frac{1}{N!} \left(\frac{D}{2} - 1\right) \cdots \left(\frac{D}{2} - 1\right) \frac{A_0(m^2)}{m^{2N}}, \quad (\text{B.4})$$

which is useful as it allows us to calculate an arbitrary N-point integral in the special case, where all external momenta are zero.

Furthermore we expect UV divergencies from all scalar bubble integrals, which we define as

$$B_0(p^2; m_1^2, m_2^2) = \mu^{2\epsilon} \int \frac{d^D q}{i\pi^2} \frac{1}{[q^2 - m_1^2][(q+p)^2 - m_2^2]}. \quad (\text{B.5})$$

The most general form can be expressed analytically through

$$\begin{aligned} B_0(p^2; m_1^2, m_2^2) &= \frac{1}{\epsilon} + 2 + x_+ \log\left(1 - \frac{1}{x_+}\right) + x_- \log\left(1 - \frac{1}{x_-}\right) - \log\left(\frac{m_1^2}{\mu^2}\right) \\ x_{\pm} &= \frac{p^2 + m_2^2 - m_1^2}{2p^2} \pm \sqrt{\left(\frac{p^2 + m_2^2 - m_1^2}{2p^2}\right)^2 - \frac{m_2^2}{p^2}}. \end{aligned} \quad (\text{B.6})$$

Note that even though  $B_0(0, 0, 0)$  vanishes identically, we only set it to zero at the very end of the calculation. It is useful to write  $B_0(0, 0, 0) = \frac{1}{\epsilon_{\text{UV}}} - \frac{1}{\epsilon_{\text{IR}}}$  to distinguish between UV and IR poles in our calculation.

### B.1.2 Integrals with Soft Divergencies

We continue to quote all necessary three and four-point integrals that exhibit infrared divergencies.

**B.1.2.1 Triangle Functions** The general triangle integral is of the form

$$C_0(p_1^2, p_2^2, (p_1 + p_2)^2; m_1^2, m_2^2, m_3^2) = \mu^{2\epsilon} \int \frac{d^D q}{i\pi^2} \frac{1}{[q^2 - m_1^2][(q + p)^2 - m_2^2][(q + p_1 + p_2)^2 - m_3^2]}. \quad (\text{B.7})$$

All infrared divergent triangle diagrams can be expressed through a set of 6 linearly independent basis functions if one makes use of the symmetry identities, expressing the cyclicity of the triangle functions

$$C_0(p_1^2, p_2^2, p_3^2; m_1^2, m_2^2, m_3^2) = C_0(p_1^2, p_3^2, p_2^2; m_2^2, m_1^2, m_3^2), \quad (\text{B.8})$$

$$C_0(p_1^2, p_2^2, p_3^2; m_1^2, m_2^2, m_3^2) = C_0(p_2^2, p_3^2, p_1^2; m_2^2, m_3^2, m_1^2). \quad (\text{B.9})$$

The relevant functions in that base are then

$$C_0(0, 0, s; 0, 0, 0) = \frac{1}{s} \left[ \frac{1}{\epsilon^2} - \frac{1}{\epsilon} \log\left(\frac{s}{\mu^2}\right) + \frac{1}{2} \log^2\left(\frac{s}{\mu^2}\right) - \frac{7\pi^2}{12} \right], \quad (\text{B.10})$$

for the s-channel as well as

$$C_0(0, p_2^2, t; 0, 0, m^2) = \quad (\text{B.11})$$

$$= \frac{1}{p_2^2 - t} \left[ \frac{1}{\epsilon} \log\left(\frac{m^2 - t}{m^2 - p_2^2}\right) + \text{Li}_2\left(\frac{p_2^2}{m^2}\right) - \text{Li}_2\left(\frac{t}{m^2}\right) + \log^2\left(\frac{m^2 - p_2^2}{m^2}\right) - \log^2\left(\frac{m^2 - t}{m^2}\right) - \log\left(\frac{m^2 - t}{m^2 - p_2^2}\right) \log\left(\frac{m^2}{\mu^2}\right) \right], \quad (\text{B.12})$$

$$C_0(0, m^2, t; 0, 0, m^2) =$$

$$= \frac{1}{t - m^2} \left[ \frac{1}{2\epsilon^2} + \frac{1}{\epsilon} \log\left(\frac{m^2}{m^2 - t}\right) + \log^2\left(\frac{m^2}{m^2 - t}\right) + \text{Li}_2\left(\frac{t}{m^2}\right) + \frac{\pi^2}{24} \right], \quad (\text{B.13})$$

for which it is useful to quote the special case in which  $t \rightarrow m^2$ , which yields

$$C_0(0, m^2, m^2; 0, 0, m^2) = \frac{1}{m^2} \left[ -\frac{1}{2\epsilon} + 1 - \log\left(\frac{m^2}{\mu^2}\right) \right], \quad (\text{B.14})$$

and finally

$$C_0(m_2^2, s, m_3^2; 0, m_2^2, m_3^2) =$$

$$= \frac{x_2}{m_2 m_3 (1 - x_2^2)} \left\{ -\frac{1}{\epsilon} \log(x_2) + \text{Li}_2\left(1 - x_2 \frac{m_2}{m_3}\right) - \frac{\pi^2}{4} + \text{Li}_2\left(1 - x_2 \frac{m_3}{m_2}\right) + \text{Li}_2(x_2^2) + \frac{1}{2} \log^2\left(\frac{m_2}{m_3}\right) + \log(x_2) \left[ -\frac{1}{2} \log(x_2) + 2 \log(1 - x_2^2) + \log\left(\frac{m_2 m_3}{\mu^2}\right) \right] \right\}. \quad (\text{B.15})$$

**B.1.2.2 Box Functions** The general scalar box integral is of the form

$$D_0(p_1^2, p_2^2, p_3^2, (p_1 + p_2 + p_3)^2, (p_1 + p_2)^2, (p_2 + p_3)^2, m_1^2, m_2^2, m_3^2, m_4^2) = \quad (\text{B.16})$$

$$= \mu^{2\epsilon} \int \frac{d^D q}{i\pi^2} \frac{1}{[q^2 - m_1^2][(q + p)^2 - m_2^2][(q + p_1 + p_2)^2 - m_3^2][(q + p_1 + p_2 + p_3)^2 - m_4^2]}.$$

There exists a set of 16 linearly independent basis functions for infrared divergent box integrals. All other divergent box functions can be expressed through the base when exploiting the cyclic symmetry relations

$$D_0(p_1^2, p_2^2, p_3^2, p_4^2, s, t; m_1^2, m_2^2, m_3^2, m_4^2) = D_0(p_2^2, p_3^2, p_4^2, p_1^2, t, s; m_2^2, m_3^2, m_4^2, m_1^2), \quad (\text{B.17})$$

$$D_0(p_1^2, p_2^2, p_3^2, p_4^2, s, t; m_1^2, m_2^2, m_3^2, m_4^2) = D_0(p_4^2, p_3^2, p_2^2, p_1^2, s, t; m_1^2, m_4^2, m_3^2, m_2^2). \quad (\text{B.18})$$

The relevant functions for our calculations are

$$D_0(0, p_2^2, p_3^2, p_4^2, s, t; 0, 0, 0, 0) = \quad (\text{B.19})$$

$$= \frac{1}{p_2^2 p_4^2 - st} \left[ -\frac{2}{\epsilon^2} + \frac{1}{\epsilon} \left( \log\left(\frac{s}{\mu^2}\right) + \log\left(-\frac{t}{\mu^2}\right) + \log\left(\frac{p_4^2}{p_2^2}\right) \right) + \log^2\left(\frac{p_2^2}{\mu^2}\right) \right. \\ \left. + \log^2\left(\frac{p_3^2}{\mu^2}\right) - \frac{1}{2} \log^2\left(\frac{p_3^2 p_4^2}{s \mu^2}\right) - \log^2\left(\frac{s}{\mu^2}\right) - \frac{1}{2} \log\left(-\frac{p_2^2 p_3^2}{t \mu^2}\right) \right. \\ \left. - \log^2\left(-\frac{t}{\mu^2}\right) - 2\text{Li}_2\left(1 - \frac{p_2^2}{s}\right) - 2\text{Li}_2\left(1 - \frac{p_4^2}{s}\right) + 2\text{Li}_2\left(1 - \frac{p_2^2 p_4^2}{2t}\right) \right. \\ \left. - \log\left(-\frac{s}{t}\right) + \frac{2\pi^2}{3} \right],$$

$$D_0(0, 0, m^2, m^2, s, t; 0, 0, 0, m^2) = \quad (\text{B.20})$$

$$= \frac{1}{s(t - m^2)} \left[ \frac{2}{\epsilon^2} - \frac{1}{\epsilon} \left( 2 \log\left(\frac{m^2 - t}{\mu^2}\right) + \log\left(\frac{s}{m^2}\right) \right) + \log\left(\frac{s}{\mu^2}\right) \log\left(\frac{(m^2 - t)^2}{m^2 \mu^2}\right) \right. \\ \left. + \log\left(\frac{s}{\mu^2}\right) \log\left(\frac{(m^2 - t^2)^2}{m^2 \mu^2}\right) - \frac{2\pi^2}{3} \right],$$

$$D_0(0, 0, m^2, m^2, s, t; m^2, m^2, m^2, 0) = \quad (\text{B.21})$$

$$= \frac{1}{s(t - m^2) \beta_2} \left[ \frac{1}{\epsilon} \log(x_1) - 2 \log(x_2) \log(\beta_2) - 2 \log(x_2) \log\left(\frac{(m^2 - t)^2}{m^2 \mu^2}\right) \right. \\ \left. - 2\text{Li}_2(x_2) + 2\text{Li}_2(-x_2) - \frac{\pi^2}{2} \right],$$

$$\begin{aligned}
D_0(0, m^2, 0, m^2, t, u; m^2, m^2, 0, 0) &= \tag{B.22} \\
&= \frac{1}{(t - m^2)(u - m^2)} \left[ \frac{1}{\epsilon^2} - \frac{1}{\epsilon} \left( \log \left( \frac{m^2 - t}{\mu^2} \right) + \log \left( \frac{m^2 - t}{m^2} \right) \right) - \frac{7\pi^2}{12} \right. \\
&\quad \left. + \frac{1}{2} \log \left( \frac{(m^2 - t)^2}{m^2 \mu^2} \right) \log \left( \frac{(m^2 - u)^2}{m^2 \mu^2} \right) \right],
\end{aligned}$$

and finally

$$\begin{aligned}
D_0(0, 0, m_1^2, m_1^2, s, t; 0, 0, 0, m_2^2) &= \tag{B.23} \\
&= \frac{1}{s(t - m_2^2)} \left[ \frac{1}{\epsilon^2} - \frac{1}{\epsilon} \left( \log \left( \frac{s}{\mu^2} \right) + 2 \log \left( \frac{m_2^2 - t}{m_2^2 - m_1^2} \right) \right) - 4 \text{Li}_2 \left( 1 + \frac{m_2^2 - m_1^2}{t - m_2^2} \right) \right. \\
&\quad - \text{Li}_2 \left( 1 + \frac{(m_2^2 - m_1^2)^2}{s m_2^2} \right) + \frac{1}{2} \log^2 \left( \frac{s}{\mu^2} \right) - \frac{1}{2} \log^2 \left( \frac{s}{m_2^2} \right) \\
&\quad + 2 \log \left( \frac{s}{m_1^2} \right) \log \left( \frac{m_2^2 - t}{m_2^2} \right) + 2 \log \left( \frac{m_1^2}{\mu^2} \right) \log \left( \frac{m_2^2 - t}{m_2^2 - m_1^2} \right) \\
&\quad \left. - 2 \log \left( \frac{m_2^2 - m_1^2}{m_1^2} \right) \log \left( \frac{m_2^2 - m_1^2}{m_2^2} \right) - \frac{\pi^2}{4} \right].
\end{aligned}$$

### B.1.3 Derivatives of One-Loop Functions

It is furthermore important to summarize the first derivatives of the  $B_0$  functions, since the field renormalization constants in the on-shell scheme are obtained through the derivatives of the self-energy functions with respect to the momentum of the external leg they are stemming from.

For derivatives with zero external momentum it is useful to note, that

$$\left. \frac{\partial^2}{\partial p^\mu \partial p_\mu} B_0(p^2, m_1^2, m_2^2) \right|_{p^2=0} = \left( \frac{\partial^2 B_0}{\partial (p^2)^2} 4p^2 + 2D \frac{\partial B_0}{\partial (p^2)} \right) \Big|_{p^2=0} = 2D \frac{\partial B_0}{\partial (p^2)} \Big|_{p^2=0}, \tag{B.24}$$

since the calculation of the derivatives are considerably simplified if one utilizes partial integration with respect to the loop momentum.

The only two cases for zero momentum derivatives are given by  $B_0$  functions with different masses

$$\begin{aligned}
B_0'(0, m_1^2, m_2^2) &= \tag{B.25} \\
&= \frac{1}{(m_1^2 - m_2^2)^3} \left[ (m_2^2 A_0(m_1^2) - m_1^2 A_0(m_2^2)) + \frac{4 - D}{D} (m_1^2 A_0(m_1^2) - m_2^2 A_0(m_2^2)) \right]
\end{aligned}$$

and the degenerate case with equal masses in the loop

$$B'_0(0, m^2, m^2) = -\frac{1}{6} \left( \frac{D}{2} - 1 \right) \left( \frac{D}{2} - 2 \right) \frac{A_0(m^2)}{m^4}. \quad (\text{B.26})$$

Notice, that in the both cases the derivatives are UV finite.

For external momentum not equal to zero we similarly perform the derivative and arrive at the general formula

$$B'_0(p^2, m_1^2, m_2^2) = \quad (\text{B.27})$$

$$= \frac{1}{2p^2} \left[ B_0(0, m_2^2, m_2^2) - B_0(p_2, m_1^2, m_2^2) + (m_1^2 - m_2^2 - p^2) C_0(0, p^2, p^2, m_2^2, m_2^2, m_1^2) \right],$$

which can be further simplified by splitting and partially integrating the  $C_0$  function.

It is important to note that the special case

$$B'_0(m^2, 0, m^2) = -\frac{D-2}{D-3} \frac{A_0(m^2)}{4m^4} \quad (\text{B.28})$$

represents a soft divergence, even though  $A_0$  functions are UV-divergent, and therefore warrants to be kept and treated separately. This relates to the fact that the threshold  $p^2 \rightarrow m^2$  exhibits an IR divergency.

### B.1.4 Useful Identities and Special Cases

Additionally we would like to quote a handful of special cases and finite functions that appear in our calculations and have played a special role.

These are the  $B_0$  function that lies exactly on the energy threshold, as it appears in the self-energies of the level-1 KK particles

$$B_0(m^2, n^2 m^2, (n \pm 1)^2 m^2) = \frac{1}{\epsilon} + 2 - \log \left( \frac{m^2 n^2}{\mu^2} \right) \pm (n \pm 1) \log \left( \frac{n^2}{(n \pm 1)^2} \right), \quad (\text{B.29})$$

as well as the corresponding  $C_0$  functions describing the KK-contributions to SM operators

$$C_0(0, 0, s, m^2, m^2, m^2) = \frac{1}{2s} \left[ \log \left( \frac{1 - \beta_1}{1 + \beta_1} \right)^2 - \pi^2 \right], \quad (\text{B.30})$$

which holds in the case that  $s \geq 4m^2$ , and to operators with two level-1 KK modes as external legs

$$C_0(0, m^2, m^2, n^2 m^2, n^2 m^2, (n \pm 1)^2 m^2) = -\frac{1}{m^2} \left[ \pm \frac{1}{n} + \log \left( \frac{n}{n \pm 1} \right) \right]. \quad (\text{B.31})$$

## B.2 SOFT ANGULAR INTEGRALS

In this appendix we quote the soft angular integrals as they appear in our description of the real emission processes in Chapter 3 and Chapter 4. The integrals left in question are generally of the form

$$I_{kl} = \int_0^\pi d\theta_1 \sin^{1-2\epsilon} \theta_1 \int_0^\pi d\theta_2 \sin^{-2\epsilon} \theta_2 \frac{(a + b \cos \theta_1)^{-k}}{(A + B \cos \theta_1 + C \sin \theta_1 \cos \theta_2)^l}, \quad (\text{B.32})$$

after the integration over the gluons energy  $E_g$  has been performed.

These integrals have been reported in the literature and we restrict ourselves to listing the ones useful for our calculations. It should however be noted that some of these have only been reported up to  $\mathcal{O}(\epsilon^0)$ , which is insufficient since in a few cases the linear term gives a non-vanishing contribution. These cases have been calculated by us and are included. The remaining integrals follow [44, 45].

To report the most compact form of the integrals it is helpful to define

$$X_S = (aA - bB)^2 - (A^2 - B^2 - C^2)(a^2 - b^2). \quad (\text{B.33})$$

We furthermore separate the integrals into classes based on how their coefficients relate to each other.

$$I_{00} = 2\pi + 2\pi\epsilon \left( \psi_0 \left( \frac{3}{2} \right) - \psi_0 \left( \frac{1}{2} \right) \right), \quad (\text{B.34})$$

where  $\psi_0(z) = \frac{\Gamma'(z)}{\Gamma(z)}$  is the digamma function.

$$I_{01} = \frac{\pi}{\sqrt{B^2 + C^2}} \left\{ \log \left( \frac{A + \sqrt{B^2 + C^2}}{A - \sqrt{B^2 + C^2}} \right) + 2\epsilon \left[ \text{Li}_2 \left( \frac{2\sqrt{B^2 + C^2}}{A + \sqrt{B^2 + C^2}} \right) + \frac{1}{4} \log^2 \left( \frac{A + \sqrt{B^2 + C^2}}{A - \sqrt{B^2 + C^2}} \right) \right] \right\}, \quad (\text{B.35})$$

$$I_{02} = \frac{2\pi}{A^2 - B^2 - C^2} \left[ 1 + \epsilon \frac{A}{\sqrt{B^2 + C^2}} \log \left( \frac{A + \sqrt{B^2 + C^2}}{A - \sqrt{B^2 + C^2}} \right) \right], \quad (\text{B.36})$$

$$I_{11} = \frac{\pi}{\sqrt{X_S}} \log \left( \frac{aA - bB + \sqrt{X_S}}{aA - bB - \sqrt{X_S}} \right), \quad (\text{B.37})$$

$$I_{12} = \pi \left[ \frac{2a(B^2 + C^2 - 2bAB)}{(A^2 - B^2 - C^2)X_S} + \frac{b(bA - aB)}{X_S^{\frac{3}{2}}} \log \left( \frac{aA - bB + \sqrt{X_S}}{aA - bB - \sqrt{X_S}} \right) \right]. \quad (\text{B.38})$$

$$I_{10} = -\frac{\pi}{a\epsilon}, \quad (\text{B.39})$$

$$I_{20} = -\frac{\pi}{a^2} \frac{1}{1 + \epsilon}, \quad (\text{B.40})$$

$$I_{11} = \frac{\pi}{a(A+B)} \left\{ -\frac{1}{\epsilon} + \log \left( \frac{(A+B)^2}{A^2 - B^2 - C^2} \right) - \epsilon \left[ \log^2 \left( \frac{A - \sqrt{B^2 + C^2}}{A+B} \right) \right. \right. \quad (\text{B.41})$$

$$\left. -\frac{1}{2} \log^2 \left( \frac{A + \sqrt{B^2 + C^2}}{A - \sqrt{B^2 + C^2}} \right) + 2\text{Li}_2 \left( -\frac{B + \sqrt{B^2 + C^2}}{A - \sqrt{B^2 + C^2}} \right) \right. \\ \left. - 2\text{Li}_2 \left( \frac{B - \sqrt{B^2 + C^2}}{A+B} \right) \right] \right\}, \quad (\text{B.42})$$

$$I_{11} = -\frac{2\pi}{a(A+B)} \left[ \frac{1}{\epsilon} - \log \left( \frac{A+B}{2A} \right) + \epsilon \left( \text{Li}_2 \left( \frac{A-B}{2A} \right) + \frac{1}{2} \log^2 \left( \frac{A+B}{2A} \right) \right) \right], \quad (\text{B.43})$$

## APPENDIX C

### KK-NUMBER VIOLATING COUPLINGS IN MUED

In this appendix, the KK-number violating couplings discussed in section 5.2 are shown for the MUED extension of the SM. Here  $g_{1,2,3}$  are the couplings of the SM  $U(1)_Y$ ,  $SU(2)_L$  and  $SU(3)_C$  gauge groups, respectively, while  $h_t$  is the top Yukawa coupling and  $\lambda_H$  the Higgs self-coupling. The  $L_n$  is defined as  $L_n \equiv \ln(\Lambda^2/m_n^2)$ .

$$-iC_{\psi_0\psi_0V_2}\gamma^\mu T^a P_\pm$$

$$C_{Q_0Q_0G_2} = \frac{\sqrt{2}g_3}{64\pi^2} \left[ g_3^2 \left( 11L_1 + 35 - \frac{11\pi^2}{3} \right) + g_2^2 \left( -\frac{27}{4}L_1 - \frac{39}{4} + \frac{21\pi^2}{16} \right) + g_1^2 \left( -\frac{1}{4}L_1 - \frac{13}{36} + \frac{7\pi^2}{144} \right) \right] \quad (C.1)$$

$$C_{t_{L_0}t_{L_0}G_2} = C_{b_{L_0}b_{L_0}G_2} = \frac{\sqrt{2}g_3}{64\pi^2} \left[ g_3^2 \left( 11L_1 + 35 - \frac{11\pi^2}{3} \right) + g_2^2 \left( -\frac{27}{4}L_1 - \frac{39}{4} + \frac{21\pi^2}{16} \right) + g_1^2 \left( -\frac{1}{4}L_1 - \frac{13}{36} + \frac{7\pi^2}{144} \right) + h_t^2 \left( L_1 - 1 + \frac{\pi^2}{4} \right) \right] \quad (C.2)$$

$$C_{u_0u_0G_2} = \frac{\sqrt{2}g_3}{64\pi^2} \left[ g_3^2 \left( 11L_1 + 35 - \frac{11\pi^2}{3} \right) + g_1^2 \left( -4L_1 - \frac{52}{9} + \frac{7\pi^2}{9} \right) \right] \quad (C.3)$$

$$C_{t_{R_0}t_{R_0}G_2} = \frac{\sqrt{2}g_3}{64\pi^2} \left[ g_3^2 \left( 11L_1 + 35 - \frac{11\pi^2}{3} \right) + g_1^2 \left( -4L_1 - \frac{52}{9} + \frac{7\pi^2}{9} \right) + h_t^2 \left( 2L_1 - 2 + \frac{\pi^2}{2} \right) \right] \quad (C.4)$$

$$C_{d_0d_0G_2} = \frac{\sqrt{2}g_3}{64\pi^2} \left[ g_3^2 \left( 11L_1 + 35 - \frac{11\pi^2}{3} \right) + g_1^2 \left( -L_1 - \frac{13}{9} + \frac{7\pi^2}{36} \right) \right] \quad (C.5)$$

$$C_{Q_0 Q_0 Z_2} = \frac{\sqrt{2}g_2}{64\pi^2} \left[ g_3^2 \left( -12L_1 - \frac{52}{3} + \frac{7\pi^2}{3} \right) + g_2^2 \left( \frac{33}{4}L_1 + \frac{299}{12} - \frac{43\pi^2}{16} \right) + g_1^2 \left( -\frac{1}{4}L_1 - \frac{13}{36} + \frac{7\pi^2}{144} \right) \right] \quad (C.6)$$

$$C_{t_{L_0} t_{L_0} Z_2} = C_{b_{L_0} b_{L_0} Z_2} = \frac{\sqrt{2}g_2}{64\pi^2} \left[ g_3^2 \left( -12L_1 - \frac{52}{3} + \frac{7\pi^2}{3} \right) + g_2^2 \left( \frac{33}{4}L_1 + \frac{299}{12} - \frac{43\pi^2}{16} \right) + g_1^2 \left( -\frac{1}{4}L_1 - \frac{13}{36} + \frac{7\pi^2}{144} \right) + h_t^2 \left( L_1 - 3 + \frac{\pi^2}{4} \right) \right] \quad (C.7)$$

$$C_{L_0 L_0 Z_2} = \frac{\sqrt{2}g_2}{64\pi^2} \left[ g_2^2 \left( \frac{33}{4}L_1 + \frac{299}{12} - \frac{43\pi^2}{16} \right) + g_1^2 \left( -\frac{9}{4}L_1 - \frac{13}{4} + \frac{7\pi^2}{16} \right) \right] \quad (C.8)$$

$$C_{Q_0 Q_0 B_2} = \frac{\sqrt{2}g_1}{64\pi^2} \left[ g_3^2 \left( -12L_1 - \frac{52}{3} + \frac{7\pi^2}{3} \right) + g_2^2 \left( -\frac{27}{4}L_1 - \frac{39}{4} + \frac{21\pi^2}{16} \right) + g_1^2 \left( -\frac{7}{12}L_1 - \frac{7}{12} + \frac{7\pi^2}{144} \right) \right] \quad (C.9)$$

$$C_{t_{L_0} t_{L_0} B_2} = C_{b_{L_0} b_{L_0} B_2} = \frac{\sqrt{2}g_1}{64\pi^2} \left[ g_3^2 \left( -12L_1 - \frac{52}{3} + \frac{7\pi^2}{3} \right) + g_2^2 \left( -\frac{27}{4}L_1 - \frac{39}{4} + \frac{21\pi^2}{16} \right) + g_1^2 \left( -\frac{7}{12}L_1 - \frac{7}{12} + \frac{7\pi^2}{144} \right) + h_t^2 \left( L_1 + 5 + \frac{\pi^2}{4} \right) \right] \quad (C.10)$$

$$C_{u_0 u_0 B_2} = \frac{\sqrt{2}g_1}{64\pi^2} \left[ g_3^2 \left( -12L_1 - \frac{52}{3} + \frac{7\pi^2}{3} \right) + g_1^2 \left( -\frac{13}{3}L_1 - 6 + \frac{7\pi^2}{9} \right) \right] \quad (C.11)$$

$$C_{t_{R_0} t_{R_0} B_2} = \frac{\sqrt{2}g_1}{64\pi^2} \left[ g_3^2 \left( -12L_1 - \frac{52}{3} + \frac{7\pi^2}{3} \right) + g_1^2 \left( -\frac{13}{3}L_1 - 6 + \frac{7\pi^2}{9} \right) + h_t^2 \left( 2L_1 - 5 + \frac{\pi^2}{2} \right) \right] \quad (C.12)$$

$$C_{d_0 d_0 B_2} = \frac{\sqrt{2}g_1}{64\pi^2} \left[ g_3^2 \left( -12L_1 - \frac{52}{3} + \frac{7\pi^2}{3} \right) + g_1^2 \left( -\frac{4}{3}L_1 - \frac{5}{3} + \frac{7\pi^2}{36} \right) \right] \quad (C.13)$$

$$C_{L_0 L_0 B_2} = \frac{\sqrt{2}g_1}{64\pi^2} \left[ g_2^2 \left( -\frac{27}{4}L_1 - \frac{39}{4} + \frac{21\pi^2}{16} \right) + g_1^2 \left( -\frac{31}{12}L_1 - \frac{125}{36} + \frac{7\pi^2}{16} \right) \right] \quad (C.14)$$

$$C_{e_0 e_0 B_2} = \frac{\sqrt{2}g_1^3}{64\pi^2} \left( -\frac{28}{3}L_1 - \frac{119}{9} + \frac{7\pi^2}{4} \right) \quad (C.15)$$

$$-i\tilde{C}_{\psi_2 \psi_0 V_0} \gamma^\mu P_\pm \quad [V_0 \text{ transverse}]$$

Note that  $\tilde{C}$  is defined without  $T^a$ , in contrast to eq. (5.33). In the expressions below,  $A$  is

an SU(3) color index.

$$\tilde{C}_{Q_2 Q_0 G_0} = \frac{\sqrt{2}g_3}{64\pi^2} T^A \left[ g_3^2 \left( -\frac{2}{3} + \frac{3\pi^2}{4} \right) + 3g_2^2 + \frac{g_1^2}{9} \right] \quad [\text{including } Q = T, B] \quad (\text{C.16})$$

$$\tilde{C}_{u_2 u_0 G_0} = \frac{\sqrt{2}g_3}{64\pi^2} T^A \left[ g_3^2 \left( -\frac{2}{3} + \frac{3\pi^2}{4} \right) + \frac{16}{9}g_1^2 \right] \quad [\text{including } u = t] \quad (\text{C.17})$$

$$\tilde{C}_{d_2 d_0 G_0} = \frac{\sqrt{2}g_3}{64\pi^2} T^A \left[ g_3^2 \left( -\frac{2}{3} + \frac{3\pi^2}{4} \right) + \frac{4}{9}g_1^2 \right] \quad (\text{C.18})$$

$$\tilde{C}_{Q_2 Q_0 Z_0} = \frac{\sqrt{2}(\pm \frac{1}{2}g_2 c_W - \frac{1}{6}g_1 s_W)}{64\pi^2} \left[ \frac{16}{3}g_3^2 + 3g_2^2 + \frac{g_1^2}{9} \right] \pm \frac{\sqrt{2}g_2^3 c_W}{128\pi^2} \left( \frac{\pi^2}{2} - 4 \right) \quad (\text{C.19})$$

[including  $Q = T, B$ ]

$$\tilde{C}_{Q_2 Q_0 \gamma_0} = \frac{\sqrt{2}(\pm \frac{1}{2}g_2 s_W + \frac{1}{6}g_1 c_W)}{64\pi^2} \left[ \frac{16}{3}g_3^2 + 3g_2^2 + \frac{g_1^2}{9} \right] \pm \frac{\sqrt{2}g_2^3 s_W}{128\pi^2} \left( \frac{\pi^2}{2} - 4 \right) \quad (\text{C.20})$$

[including  $Q = T, B$ ]

$$-\frac{1}{s_W} \tilde{C}_{u_2 u_0 Z_0} = \frac{1}{c_W} \tilde{C}_{u_2 u_0 \gamma_0} = \frac{\sqrt{2}g_1}{96\pi^2} \left[ \frac{16}{3}g_3^2 + \frac{16}{9}g_1^2 \right] \quad [\text{including } u = t] \quad (\text{C.21})$$

$$-\frac{1}{s_W} \tilde{C}_{d_2 d_0 Z_0} = \frac{1}{c_W} \tilde{C}_{d_2 d_0 \gamma_0} = -\frac{\sqrt{2}g_1}{192\pi^2} \left[ \frac{16}{3}g_3^2 + \frac{4}{9}g_1^2 \right] \quad (\text{C.22})$$

$$\tilde{C}_{L_2 L_0 Z_0} = \frac{\sqrt{2}(\pm \frac{1}{2}g_2 c_W + \frac{1}{2}g_1 s_W)}{64\pi^2} [3g_2^2 + g_1^2] \pm \frac{\sqrt{2}g_2^3 c_W}{128\pi^2} \left( \frac{\pi^2}{2} - 4 \right) \quad (\text{C.23})$$

$$\tilde{C}_{L_2 L_0 \gamma_0} = \frac{\sqrt{2}(\pm \frac{1}{2}g_2 s_W - \frac{1}{2}g_1 c_W)}{64\pi^2} [3g_2^2 + g_1^2] \pm \frac{\sqrt{2}g_2^3 s_W}{128\pi^2} \left( \frac{\pi^2}{2} - 4 \right) \quad (\text{C.24})$$

$$-\frac{1}{s_W} \tilde{C}_{e_2 e_0 Z_0} = \frac{1}{c_W} \tilde{C}_{e_2 e_0 \gamma_0} = -\frac{\sqrt{2}g_1^3}{16\pi^2} \quad (\text{C.25})$$

In eqs. (C.19) ff., the  $\pm$  signs indicate the upper/lower entry of a fermion doublet.

$$-\tilde{D}_{\psi_2 \psi_0 V_0} \frac{\sigma^{\mu\nu} q_\nu}{2m_{KK}} P_\pm$$

Note that  $\tilde{D}$  is defined without  $T^a$ , in contrast to eq. (5.34). In the expressions below,  $A$  is

an SU(3) color index.

$$\tilde{D}_{Q_2 Q_0 G_0} = \frac{\sqrt{2}g_3}{64\pi^2} T^A \left[ g_3^2(-17 + 2\pi^2) + g_2^2 \left( \frac{9}{4} - \frac{9\pi^2}{16} \right) + g_1^2 \left( \frac{1}{12} - \frac{\pi^2}{48} \right) \right] \quad (\text{C.26})$$

$$\begin{aligned} \tilde{D}_{T_2 t_{L_0} G_0} = \tilde{D}_{B_2 b_{L_0} G_0} &= \frac{\sqrt{2}g_3}{64\pi^2} T^A \left[ g_3^2(-17 + 2\pi^2) + g_2^2 \left( \frac{9}{4} - \frac{9\pi^2}{16} \right) \right. \\ &\quad \left. + g_1^2 \left( \frac{1}{12} - \frac{\pi^2}{48} \right) + h_t^2 \left( \frac{\pi^2}{4} - 1 \right) \right] \end{aligned} \quad (\text{C.27})$$

$$\tilde{D}_{u_2 u_0 G_0} = \frac{\sqrt{2}g_3}{64\pi^2} T^A \left[ g_3^2(-17 + 2\pi^2) + g_1^2 \left( \frac{4}{3} - \frac{\pi^2}{3} \right) \right] \quad (\text{C.28})$$

$$\tilde{D}_{t_2 t_{R_0} G_0} = \frac{\sqrt{2}g_3}{64\pi^2} T^A \left[ g_3^2(-17 + 2\pi^2) + g_1^2 \left( \frac{4}{3} - \frac{\pi^2}{3} \right) + h_t^2 \left( \frac{\pi^2}{2} - 2 \right) \right] \quad (\text{C.29})$$

$$\tilde{D}_{d_2 d_0 G_0} = \frac{\sqrt{2}g_3}{64\pi^2} T^A \left[ g_3^2(-17 + 2\pi^2) + g_1^2 \left( \frac{1}{3} - \frac{\pi^2}{12} \right) \right] \quad (\text{C.30})$$

$$\begin{aligned} \tilde{D}_{Q_2 Q_0 Z_0} &= \frac{\sqrt{2}(\pm \frac{1}{2}g_2 c_W - \frac{1}{6}g_1 s_W)}{64\pi^2} \left[ g_3^2(4 - \pi^2) + g_2^2 \left( \frac{9}{4} - \frac{9\pi^2}{16} \right) + g_1^2 \left( \frac{1}{12} - \frac{\pi^2}{48} \right) \right] \\ &\quad \pm \frac{\sqrt{2}g_2^3 c_W}{128\pi^2} (-14 + 2\pi^2) \end{aligned} \quad (\text{C.31})$$

$$\begin{aligned} \tilde{D}_{T_2 t_{L_0} Z_0} / \tilde{D}_{B_2 b_{L_0} Z_0} &= \frac{\sqrt{2}(\pm \frac{1}{2}g_2 c_W - \frac{1}{6}g_1 s_W)}{64\pi^2} \left[ g_3^2(4 - \pi^2) + g_2^2 \left( \frac{9}{4} - \frac{9\pi^2}{16} \right) + g_1^2 \left( \frac{1}{12} - \frac{\pi^2}{48} \right) \right] \\ &\quad \pm \frac{\sqrt{2}g_2^3 c_W}{128\pi^2} (-14 + 2\pi^2) \\ &\quad + \frac{\sqrt{2}h_t^2}{64\pi^2} \left[ \pm \frac{g_2 c_W}{2} \left( 3 - \frac{\pi^2}{4} \right) - \frac{g_1 s_W}{6} \left( -13 + \frac{7\pi^2}{4} \right) \right] \end{aligned} \quad (\text{C.32})$$

$$\begin{aligned} \tilde{D}_{Q_2 Q_0 \gamma_0} &= \frac{\sqrt{2}(\pm \frac{1}{2}g_2 s_W + \frac{1}{6}g_1 c_W)}{64\pi^2} \left[ g_3^2(4 - \pi^2) + g_2^2 \left( \frac{9}{4} - \frac{9\pi^2}{16} \right) + g_1^2 \left( \frac{1}{12} - \frac{\pi^2}{48} \right) \right] \\ &\quad \pm \frac{\sqrt{2}g_2^3 s_W}{128\pi^2} (-14 + 2\pi^2) \end{aligned} \quad (\text{C.33})$$

$$\begin{aligned} \tilde{D}_{T_2 t_{L_0} \gamma_0} / \tilde{D}_{B_2 b_{L_0} \gamma_0} &= \frac{\sqrt{2}(\pm \frac{1}{2}g_2 s_W + \frac{1}{6}g_1 c_W)}{64\pi^2} \left[ g_3^2(4 - \pi^2) + g_2^2 \left( \frac{9}{4} - \frac{9\pi^2}{16} \right) + g_1^2 \left( \frac{1}{12} - \frac{\pi^2}{48} \right) \right] \\ &\quad \pm \frac{\sqrt{2}g_2^3 s_W}{128\pi^2} (-14 + 2\pi^2) \\ &\quad + \frac{\sqrt{2}h_t^2}{64\pi^2} \left[ \pm \frac{g_2 s_W}{2} \left( 3 - \frac{\pi^2}{4} \right) + \frac{g_1 c_W}{6} \left( -13 + \frac{7\pi^2}{4} \right) \right] \end{aligned} \quad (\text{C.34})$$

$$-\frac{1}{s_W} \tilde{D}_{u_2 u_0 Z_0} = \frac{1}{c_W} \tilde{D}_{u_2 u_0 \gamma_0} = \frac{\sqrt{2} g_1}{96 \pi^2} \left[ g_3^2 (4 - \pi^2) + g_1^2 \left( \frac{4}{3} - \frac{\pi^2}{3} \right) \right] \quad (\text{C.35})$$

$$-\frac{1}{s_W} \tilde{D}_{t_2 t_{R0} Z_0} = \frac{1}{c_W} \tilde{D}_{t_2 t_{R0} \gamma_0} = \frac{\sqrt{2} g_1}{96 \pi^2} \left[ g_3^2 (4 - \pi^2) + g_1^2 \left( \frac{4}{3} - \frac{\pi^2}{3} \right) + h_t^2 \left( -\frac{\pi^2}{4} \right) \right] \quad (\text{C.36})$$

$$-\frac{1}{s_W} \tilde{D}_{d_2 d_0 Z_0} = \frac{1}{c_W} \tilde{D}_{d_2 d_0 \gamma_0} = -\frac{\sqrt{2} g_1}{192 \pi^2} \left[ g_3^2 (4 - \pi^2) + g_1^2 \left( \frac{1}{3} - \frac{\pi^2}{12} \right) \right] \quad (\text{C.37})$$

$$\begin{aligned} \tilde{D}_{L_2 L_0 Z_0} &= \frac{\sqrt{2} (\pm \frac{1}{2} g_2 c_W + \frac{1}{2} g_1 s_W)}{64 \pi^2} \left[ g_2^2 \left( \frac{9}{4} - \frac{9 \pi^2}{16} \right) + g_1^2 \left( \frac{3}{4} - \frac{3 \pi^2}{16} \right) \right] \\ &\quad \pm \frac{\sqrt{2} g_2^3 c_W}{128 \pi^2} (-14 + 2 \pi^2) \end{aligned} \quad (\text{C.38})$$

$$\begin{aligned} \tilde{D}_{L_2 L_0 \gamma_0} &= \frac{\sqrt{2} (\pm \frac{1}{2} g_2 s_W - \frac{1}{2} g_1 c_W)}{64 \pi^2} \left[ g_2^2 \left( \frac{9}{4} - \frac{9 \pi^2}{16} \right) + g_1^2 \left( \frac{3}{4} - \frac{3 \pi^2}{16} \right) \right] \\ &\quad \pm \frac{\sqrt{2} g_2^3 s_W}{128 \pi^2} (-14 + 2 \pi^2) \end{aligned} \quad (\text{C.39})$$

$$-\frac{1}{s_W} \tilde{D}_{e_2 e_0 Z_0} = \frac{1}{c_W} \tilde{D}_{e_2 e_0 \gamma_0} = -\frac{\sqrt{2} g_1^3}{64 \pi^2} \left( 3 - \frac{3 \pi^2}{4} \right) \quad (\text{C.40})$$

In eqs. (C.31) ff., the  $\pm$  signs indicate the upper/lower entry of a fermion doublet.

$$\begin{aligned} f_{abc} \left\{ \left[ \eta_{\mu\nu} (p - k_1)_\rho + \eta_{\nu\rho} (k_1 - k_2)_\mu + \eta_{\rho\mu} (k_2 - p)_\nu \right] C_{V_2 V_0 V_0} \right. \\ \left. + \left[ -\eta_{\mu\nu} k_{1,\rho} + \eta_{\rho\mu} k_{2,\nu} \right] D_{V_2 V_0 V_0} + \eta_{\nu\rho} (k_1 - k_2)_\mu E_{V_2 V_0 V_0} \right\} \quad [\text{all momenta incoming}] \end{aligned}$$

$$C_{G_2 G_0 G_0} = \frac{3\sqrt{2} g_3^3}{64 \pi^2} \left( -\frac{157}{9} + \frac{7 \pi^2}{6} \right) \quad (\text{C.41})$$

$$D_{G_2 G_0 G_0} = \frac{3\sqrt{2} g_3^3}{64 \pi^2} \left( \frac{91}{6} - \pi^2 \right) \quad (\text{C.42})$$

$$E_{G_2 G_0 G_0} = \frac{3\sqrt{2} g_3^3}{64 \pi^2} \left( \frac{38}{3} - \frac{3 \pi^2}{4} \right) \quad (\text{C.43})$$

$$C_{Z_2 W_0^+ W_0^-} = \frac{1}{c_W} C_{W_2^- W_0^+ Z_0} = -\frac{1}{s_W} C_{W_2^- W_0^+ \gamma_0} = \frac{i\sqrt{2} g_2^3}{64 \pi^2} \left( -\frac{316}{9} + \frac{85 \pi^2}{36} \right) \quad (\text{C.44})$$

$$D_{Z_2 W_0^+ W_0^-} = \frac{1}{c_W} D_{W_2^- W_0^+ Z_0} = -\frac{1}{s_W} D_{W_2^- W_0^+ \gamma_0} = \frac{i\sqrt{2} g_2^3}{64 \pi^2} \left( \frac{92}{3} - \frac{49 \pi^2}{24} \right) \quad (\text{C.45})$$

$$E_{Z_2 W_0^+ W_0^-} = \frac{1}{c_W} E_{W_2^- W_0^+ Z_0} = -\frac{1}{s_W} E_{W_2^- W_0^+ \gamma_0} = \frac{i\sqrt{2} g_2^3}{64 \pi^2} \left( \frac{38}{3} - \frac{3 \pi^2}{4} \right) \quad (\text{C.46})$$

## BIBLIOGRAPHY

- [1] D. J. E. Callaway, Phys. Rept. **167**, 241 (1988); R. Fernandez, J. Frohlich and A. D. Sokal, “Random walks, critical phenomena, and triviality in quantum field theory,” Berlin, Germany: Springer (1992) (Texts and monographs in physics).
- [2] D. J. E. Callaway, Nucl. Phys. B **233**, 189 (1984); M. Lindner, Z. Phys. C **31**, 295 (1986).
- [3] L. D. Landau, A. A. Abrikosov and I. M. Khalatnikov, Doklady Akademii Nauk SSSR. 95: 497 (1954); L. D. Landau; A. A. Abrikosov and I. M. Khalatnikov, Doklady Akademii Nauk SSSR. 95: 1177 (1954).
- [4] V. C. Rubin and W. K. Ford, Jr., Astrophys. J. **159**, 379 (1970).
- [5] A. N. Taylor, S. Dye, T. J. Broadhurst, N. Benitez and E. van Kampen, Astrophys. J. **501**, 539 (1998), [astro-ph/9801158].
- [6] P. A. R. Ade *et al.* [Planck Collaboration], Astron. Astrophys. **594**, A13 (2016) [arXiv:1502.01589 [astro-ph.CO]].
- [7] T. Appelquist and J. Carazzone, Phys. Rev. D **11**, 2856 (1975).
- [8] D. Hooper and S. Profumo, Phys. Rept. **453**, 29 (2007) [hep-ph/0701197].
- [9] T. Kaluza, Sitzungsber. Preuss. Akad. Wiss. Berlin (Math. Phys.) **1921** (1921) 966.
- [10] O. Klein, Z. Phys. **37**, 895 (1926) [Surveys High Energ. Phys. **5**, 241 (1986)].
- [11] E. Witten, Conf. Proc. C **8306011**, 227 (1983).
- [12] L. Randall and R. Sundrum, Phys. Rev. Lett. **83**, 3370 (1999) [hep-ph/9905221].
- [13] L. Randall and R. Sundrum, Phys. Rev. Lett. **83**, 4690 (1999) [hep-th/9906064].
- [14] A. Karch, E. Katz, D. T. Son and M. A. Stephanov, Phys. Rev. D **74**, 015005 (2006) [hep-ph/0602229].
- [15] A. Falkowski and M. Perez-Victoria, JHEP **0812**, 107 (2008) [arXiv:0806.1737 [hep-ph]].

- [16] N. Arkani-Hamed, S. Dimopoulos and G. R. Dvali, Phys. Lett. B **429**, 263 (1998) [hep-ph/9803315].
- [17] I. Antoniadis, N. Arkani-Hamed, S. Dimopoulos and G. R. Dvali, Phys. Lett. B **436**, 257 (1998) [hep-ph/9804398].
- [18] T. Appelquist, H. C. Cheng and B. A. Dobrescu, Phys. Rev. D **64**, 035002 (2001) [hep-ph/0012100].
- [19] E. Ponton, arXiv:1207.3827 [hep-ph]; C. Csaki, J. Hubisz and P. Meade, hep-ph/0510275; G. D. Kribs, hep-ph/0605325.
- [20] D. Binosi, J. Collins, C. Kaufhold and L. Theussl, Comput. Phys. Commun. **180**, 1709 (2009) [arXiv:0811.4113 [hep-ph]].
- [21] H. C. Cheng, J. L. Feng and K. T. Matchev, Phys. Rev. Lett. **89**, 211301 (2002) [hep-ph/0207125]; G. Servant and T. M. P. Tait, Nucl. Phys. B **650**, 391 (2003) [hep-ph/0206071]; F. Burnell and G. D. Kribs, Phys. Rev. D **73**, 015001 (2006) [hep-ph/0509118]; K. Kong and K. T. Matchev, JHEP **0601**, 038 (2006) [hep-ph/0509119]. S. Arrenberg, L. Baudis, K. Kong, K. T. Matchev and J. Yoo, Phys. Rev. D **78**, 056002 (2008) [arXiv:0805.4210 [hep-ph]].
- [22] Z. Chacko, M. A. Luty and E. Ponton, JHEP **0007**, 036 (2000) [hep-ph/9909248]. G. Bhattacharyya, A. Datta, S. K. Majee and A. Raychaudhuri, Nucl. Phys. B **760** (2007) 117 [hep-ph/0608208]. R. S. Chivukula, D. A. Dicus and H. J. He, Phys. Lett. B **525** (2002) 175 [hep-ph/0111016].
- [23] G. Aad *et al.* [ATLAS Collaboration], JHEP **1504**, 116 (2015) [arXiv:1501.03555 [hep-ex]]; N. Deutschmann, T. Flacke and J. S. Kim, Phys. Lett. B **771**, 515 (2017) [arXiv:1702.00410 [hep-ph]]; J. Beuria, A. Datta, D. Debnath and K. T. Matchev, arXiv:1702.00413 [hep-ph].
- [24] A. Belyaev, M. Brown, J. Moreno and C. Papineau, JHEP **1306**, 080 (2013) [arXiv:1212.4858 [hep-ph]].
- [25] A. Datta, K. Kong and K. T. Matchev, New J. Phys. **12**, 075017 (2010) [arXiv:1002.4624 [hep-ph]].
- [26] A. Datta, K. Kong and K. Matchev, “Minimal Universal Extra Dimensions in CalcHEP/CompHEP,” <http://home.fnal.gov/~kckong/mued/mued.pdf>.
- [27] C. Macesanu, Int. J. Mod. Phys. A **21**, 2259 (2006) [hep-ph/0510418].
- [28] R. S. Chivukula, A. Farzinnia, E. H. Simmons and R. Foadi, Phys. Rev. D **85**, 054005 (2012) [arXiv:1111.7261 [hep-ph]].
- [29] S. R. Coleman, J. Wess and B. Zumino, Phys. Rev. **177**, 2239 (1969); C. G. Callan, S. R. Coleman, J. Wess and B. Zumino, Phys. Rev. **177**, 2247 (1969).

- [30] A. Mück, A. Pilaftsis and R. Rückl, *Phys. Rev. D* **65**, 085037 (2002) [hep-ph/0110391].
- [31] A. Freitas and D. Wiegand, *JHEP* **1709**, 058 (2017) [arXiv:1706.09442 [hep-ph]].
- [32] W. Beenakker, R. Höpker, M. Spira and P. M. Zerwas, *Nucl. Phys. B* **492**, 51 (1997) [hep-ph/9610490].
- [33] W. Beenakker, M. Krämer, T. Plehn, M. Spira and P. M. Zerwas, *Nucl. Phys. B* **515**, 3 (1998) [hep-ph/9710451].
- [34] W. Beenakker, C. Borschensky, M. Krämer, A. Kulesza, E. Laenen, V. Theeuwes and S. Thewes, *JHEP* **1412**, 023 (2014) [arXiv:1404.3134 [hep-ph]]; W. Beenakker, C. Borschensky, R. Heger, M. Krämer, A. Kulesza and E. Laenen, *JHEP* **1605**, 153 (2016) [arXiv:1601.02954 [hep-ph]].
- [35] M. Krämer, T. Plehn, M. Spira and P. M. Zerwas, *Phys. Rev. Lett.* **79**, 341 (1997) [hep-ph/9704322].
- [36] M. Cacciari, M. Czakon, M. Mangano, A. Mitov and P. Nason, *Phys. Lett. B* **710**, 612 (2012) [arXiv:1111.5869 [hep-ph]].
- [37] D. Gonçalves-Netto, D. López-Val, K. Mawatari, T. Plehn and I. Wigmore, *Phys. Rev. D* **85**, 114024 (2012) [arXiv:1203.6358 [hep-ph]].
- [38] H. X. Zhu, C. S. Li, D. Y. Shao, J. Wang and C. P. Yuan, *Eur. Phys. J. C* **72**, 2232 (2012) [arXiv:1201.0672 [hep-ph]]; R. S. Chivukula, A. Farzinia, J. Ren and E. H. Simmons, *Phys. Rev. D* **87**, no. 9, 094011 (2013) [arXiv:1303.1120 [hep-ph]].
- [39] H. Georgi, A. K. Grant and G. Hailu, *Phys. Lett. B* **506**, 207 (2001) [hep-ph/0012379].
- [40] W. E. Caswell, *Phys. Rev. Lett.* **33**, 244 (1974).
- [41] V. Ilisie, “Concepts in Quantum Field Theory: A Practitioner’s Toolkit,” Springer, Switzerland (2016), chapter 9.3.
- [42] T. Kinoshita, *J. Math. Phys.* **3**, 650 (1962); T. D. Lee and M. Nauenberg, *Phys. Rev.* **133**, B1549 (1964); F. Bloch and A. Nordsieck, *Phys. Rev.* **52**, 54 (1937).
- [43] L. J. Bergmann, “Next-to-leading Log Qcd Calculation Of Symmetric Dihadron Production,” PhD Thesis, UMI-89-15738 (1989).
- [44] B. W. Harris and J. F. Owens, *Phys. Rev. D* **65**, 094032 (2002) [hep-ph/0102128].
- [45] W. Beenakker, H. Kuijf, W. L. van Neerven and J. Smith, *Phys. Rev. D* **40**, 54 (1989).
- [46] G. Altarelli and G. Parisi, *Nucl. Phys. B* **126**, 298 (1977).
- [47] P. Breitenlohner and D. Maison, *Commun. Math. Phys.* **52**, 11 (1977).

- [48] S. A. Larin, In \*Zvenigorod 1992, Quarks '92\* 201-211.
- [49] T. Hahn, Comput. Phys. Commun. **140**, 418 (2001) [hep-ph/0012260].
- [50] V. Shtabovenko, R. Mertig and F. Orellana, Comput. Phys. Commun. **207**, 432 (2016) [arXiv:1601.01167 [hep-ph]].
- [51] G. Passarino and M. J. G. Veltman, Nucl. Phys. B **160**, 151 (1979).
- [52] T. Hahn, PoS ACAT **2010**, 078 (2010) [arXiv:1006.2231 [hep-ph]].
- [53] R. Höpker, “Hadroproduction and decay of squarks and gluinos,” (in german), PhD Thesis, DESY-T-96-02, INT.REP.T-96-02 (1996).
- [54] A. Buckley, J. Ferrando, S. Lloyd, K. Nordström, B. Page, M. Rufenacht, M. Schönherr and G. Watt, Eur. Phys. J. C **75**, 132 (2015) [arXiv:1412.7420 [hep-ph]].
- [55] D. Stump, J. Huston, J. Pumplin, W. K. Tung, H. L. Lai, S. Kuhlmann and J. F. Owens, JHEP **0310**, 046 (2003) [hep-ph/0303013].
- [56] M. R. Whalley, D. Bourilkov and R. C. Group, hep-ph/0508110; <http://lhapdf.hepforge.org>.
- [57] J. Pumplin, D. R. Stump, J. Huston, H. L. Lai, P. M. Nadolsky and W. K. Tung, JHEP **0207**, 012 (2002) [hep-ph/0201195].
- [58] T. R. Taylor and G. Veneziano, Phys. Lett. B **212**, 147 (1988).
- [59] K. R. Dienes, E. Dudas and T. Gherghetta, Nucl. Phys. B **537**, 47 (1999) [hep-ph/9806292].
- [60] K. R. Dienes, E. Dudas and T. Gherghetta, Phys. Lett. B **436**, 55 (1998) [hep-ph/9803466].
- [61] H. Gies, Phys. Rev. D **68**, 085015 (2003) [hep-th/0305208].
- [62] I. Z. Rothstein, hep-ph/0308266.
- [63] J. Kubo, H. Terao and G. Zoupanos, Nucl. Phys. B **574**, 495 (2000) [hep-ph/9910277].
- [64] A. Freitas and D. Wiegand, [arXiv:180xx.xxxx [hep-ph]] (in preparation).
- [65] A. Sfondrini, PoS ModaveVIII , 005 (2012) [arXiv:1210.2262 [hep-th]].
- [66] K. G. Wilson and J. B. Kogut, Phys. Rept. **12**, 75 (1974). K. G. Wilson, Rev. Mod. Phys. **47**, 773 (1975).
- [67] C. Wetterich, Nucl. Phys. B **352**, 529 (1991). C. Wetterich, Phys. Lett. B **301**, 90 (1993) [arXiv:1710.05815 [hep-th]].

- [68] D. F. Litim, Nucl. Phys. B **631**, 128 (2002) [hep-th/0203006].
- [69] D. F. Litim, Phys. Lett. B **486**, 92 (2000) [hep-th/0005245]; D. F. Litim, Phys. Rev. D **64**, 105007 (2001) [hep-th/0103195]. D. F. Litim, Int. J. Mod. Phys. A **16**, 2081 (2001) [hep-th/0104221].
- [70] A. O. Barvinsky and G. A. Vilkovisky, Nucl. Phys. B **282**, 163 (1987).
- [71] A. O. Barvinsky and G. A. Vilkovisky, Nucl. Phys. B **333**, 471 (1990).
- [72] I. G. Avramidi, Phys. Lett. B **236**, 443 (1990).
- [73] I. G. Avramidi, hep-th/9509077.
- [74] A. Codello and O. Zanusso, J. Math. Phys. **54**, 013513 (2013) [arXiv:1203.2034 [math-ph]].
- [75] A. Codello, R. Percacci, L. Rachwał and A. Tonero, Eur. Phys. J. C **76**, no. 4, 226 (2016) [arXiv:1505.03119 [hep-th]].
- [76] V. P. Gusynin and I. A. Shovkovy, J. Math. Phys. **40**, 5406 (1999) [hep-th/9804143].
- [77] M. Reuter and C. Wetterich, Nucl. Phys. B **417**, 181 (1994). H. Gies, Phys. Rev. D **66**, 025006 (2002) [hep-th/0202207].
- [78] M. Srednicki, “Quantum field theory,” Cambridge University Press (2007), chapter 78.
- [79] A. Freitas, K. Kong and D. Wiegand, JHEP **1803**, 093 (2018) [arXiv:1711.07526 [hep-ph]].
- [80] H. C. Cheng, K. T. Matchev and M. Schmaltz, Phys. Rev. D **66**, 036005 (2002) [hep-ph/0204342].
- [81] R. Z. Roskies, M. J. Levine and E. Remiddi, Adv. Ser. Direct. High Energy Phys. **7**, 162 (1990).
- [82] M. Kakizaki, S. Matsumoto, Y. Sato and M. Senami, Phys. Rev. D **71**, 123522 (2005) [hep-ph/0502059]; M. Kakizaki, S. Matsumoto, Y. Sato and M. Senami, Nucl. Phys. B **735**, 84 (2006) [hep-ph/0508283].
- [83] H. C. Cheng, K. T. Matchev and M. Schmaltz, Phys. Rev. D **66**, 056006 (2002) [hep-ph/0205314].
- [84] T. G. Rizzo, Phys. Rev. D **64**, 095010 (2001) [hep-ph/0106336]; C. Macesanu, C. D. McMullen and S. Nandi, Phys. Rev. D **66**, 015009 (2002) [hep-ph/0201300]; J. M. Smillie and B. R. Webber, JHEP **0510**, 069 (2005) [hep-ph/0507170].

- [85] T. Flacke, A. Menon and D. J. Phalen, Phys. Rev. D **79**, 056009 (2009) [arXiv:0811.1598 [hep-ph]]; T. Flacke, K. Kong and S. C. Park, Mod. Phys. Lett. A **30**, 1530003 (2015) [arXiv:1408.4024 [hep-ph]]. T. Flacke, K. Kong and S. C. Park, JHEP **1305**, 111 (2013) [arXiv:1303.0872 [hep-ph]].
- [86] N. Craig, P. Draper, K. Kong, Y. Ng and D. Whiteson, arXiv:1610.09392 [hep-ph].
- [87] A. Codello and A. Tonerio, Phys. Rev. D **94**, no. 2, 025015 (2016) [arXiv:1504.00225 [hep-th]].
- [88] C. T. Hill, Phys. Lett. B **266**, 419 (1991).
- [89] C. T. Hill and S. J. Parke, Phys. Rev. D **49**, 4454 (1994) [hep-ph/9312324]; R. S. Chivukula, A. G. Cohen and E. H. Simmons, Phys. Lett. B **380**, 92 (1996) [hep-ph/9603311].
- [90] L. Randall, Nucl. Phys. B **403**, 122 (1993) [hep-ph/9210231]; G. Burdman and N. J. Evans, Phys. Rev. D **59**, 115005 (1999) [hep-ph/9811357].
- [91] E. H. Simmons, Phys. Rev. D **55**, 1678 (1997) [hep-ph/9608269]; A. Atre, R. S. Chivukula, P. Ittisamai, E. H. Simmons and J. H. Yu, Phys. Rev. D **86**, 054003 (2012) [arXiv:1206.1661 [hep-ph]]; R. Sekhar Chivukula, P. Ittisamai and E. H. Simmons, Phys. Rev. D **91**, no. 5, 055021 (2015) [arXiv:1406.2003 [hep-ph]].
- [92] G. Aad *et al.* [ATLAS Collaboration], JHEP **1508**, 148 (2015) [arXiv:1505.07018 [hep-ex]]; G. Aad *et al.* [ATLAS Collaboration], Phys. Lett. B **754**, 302 (2016) [arXiv:1512.01530 [hep-ex]]; M. Aaboud *et al.* [ATLAS Collaboration], Phys. Lett. B **759**, 229 (2016) [arXiv:1603.08791 [hep-ex]].
- [93] V. Khachatryan *et al.* [CMS Collaboration], Phys. Rev. D **93**, no. 1, 012001 (2016) [arXiv:1506.03062 [hep-ex]]; A. M. Sirunyan *et al.* [CMS Collaboration], arXiv:1611.03568 [hep-ex].
- [94] T. G. Rizzo, Phys. Rev. D **64**, 095010 (2001) [hep-ph/0106336]; C. Macesanu, C. D. McMullen and S. Nandi, Phys. Rev. D **66**, 015009 (2002) [hep-ph/0201300]; H. C. Cheng, K. T. Matchev and M. Schmaltz, Phys. Rev. D **66**, 056006 (2002) [hep-ph/0205314]; A. Datta, K. Kong and K. T. Matchev, Phys. Rev. D **72**, 096006 (2005), Erratum: Phys. Rev. D **72**, 119901 (2005) [hep-ph/0509246]; J. M. Smillie and B. R. Webber, JHEP **0510**, 069 (2005) [hep-ph/0507170]; J. A. R. Cembranos, J. L. Feng and L. E. Strigari, Phys. Rev. D **75**, 036004 (2007) [hep-ph/0612157].
- [95] M. Kakizaki, S. Matsumoto and M. Senami, Phys. Rev. D **74**, 023504 (2006) [hep-ph/0605280]; G. Belanger, M. Kakizaki and A. Pukhov, JCAP **1102**, 009 (2011) [arXiv:1012.2577 [hep-ph]].
- [96] J. A. R. Cembranos, J. L. Feng and L. E. Strigari, Phys. Rev. D **75**, 036004 (2007) [hep-ph/0612157].

- [97] A. Datta, K. Kong and K. T. Matchev, Phys. Rev. D **72**, 096006 (2005) [Erratum: Phys. Rev. D **72**, 119901 (2005)] [hep-ph/0509246].
- [98] A. Belyaev, N. D. Christensen and A. Pukhov, Comput. Phys. Commun. **184**, 1729 (2013) [arXiv:1207.6082 [hep-ph]].
- [99] A. Freitas, “Fermionische Zwei-Schleifen-Beiträge zum Myon-Zerfall,” (in german), Diploma Thesis, Universität Karlsruhe (1999).
- [100] R. K. Ellis and G. Zanderighi, JHEP **0802**, 002 (2008) [arXiv:0712.1851 [hep-ph]].